

Sun, Baoqing (2015) *Three dimensional computational imaging with single-pixel detectors*. PhD thesis.

<http://theses.gla.ac.uk/6127/>

Copyright and moral rights for this thesis are retained by the author

A copy can be downloaded for personal non-commercial research or study, without prior permission or charge

This thesis cannot be reproduced or quoted extensively from without first obtaining permission in writing from the Author

The content must not be changed in any way or sold commercially in any format or medium without the formal permission of the Author

When referring to this work, full bibliographic details including the author, title, awarding institution and date of the thesis must be given

UNIVERSITY OF GLASGOW

Three Dimensional Computational Imaging With Single-pixel Detectors

by

Baoqing Sun

A thesis submitted in partial fulfillment for the
degree of Doctor of Philosophy

in the
Optics Group
School of Physics and Astronomy

February 17, 2015

Declaration of Authorship

I, BAOQING SUN, declare that this thesis titled, ‘Three Dimensional Computational Imaging With Single-pixel Detectors’ and the work presented in it are my own. I confirm that:

- This work was done wholly or mainly while in candidature for a research degree at this University.
- Where any part of this thesis has previously been submitted for a degree or any other qualification at this University or any other institution, this has been clearly stated.
- Where I have consulted the published work of others, this is always clearly attributed.
- Where I have quoted from the work of others, the source is always given. With the exception of such quotations, this thesis is entirely my own work.
- I have acknowledged all main sources of help.
- Where the thesis is based on work done by myself jointly with others, I have made clear exactly what was done by others and what I have contributed myself.

Signed:

Date:

There was one day when I came to the university. At the entrance I was stopped by a doorman and asked three profound philosophical questions:

“Who are you? Where are you from? Where are you going to?”

Abstract

Computational imaging with single-pixel detectors utilises spatial correlation of light to obtain images. A series of structured illumination is generated using a spatial light modulator to encode the spatial information of an object. The encoded object images are recorded as total intensities with no spatial information by a single-pixel detector. These intensities are then sent to correlate with their corresponding illumination structures to derive an image. This correlation imaging method was first recognised as a quantum imaging technique called “ghost imaging” (GI) in 1995. Quantum GI uses the spatial correlation of entangled photon pairs to form images and was later demonstrated also by using classical correlated light beams. In 2008, an adaptive classical GI system called computational GI which employed a spatial light modulator and a single-pixel detector was proposed. Since its proposal, this computational imaging technique received intensive interest for this potential application. The aim of the work in this thesis was to improve this new imaging technique into a more applicable stage.

Our contribution mainly includes three aspects. First an advanced reconstruction algorithm called normalised ghost imaging was developed to improve the correlation efficiency. By normalising the object intensity with a reference beam, the reconstruction single-to-noise ratio can be increased, especially for a more transmissive object. In the second work, a computational imaging scheme adapted from computational GI was designed by using a digital light projector for structured illumination. Compared to a conventional computational GI system, the adaptive system improved the reconstruction efficiency significantly. And for the first time, correlation imaging using structured illumination and single-pixel detection was able to image a 3 dimensional reflective object with reasonable details. By using several single-pixel detectors, the system was able to retrieve the 3 dimensional profile of the object. In the last work, effort was devoted to increase the reconstruction speed of the single-pixel imaging technique, and a fast computational imaging system was built up to generate real-time single-pixel videos.

Acknowledgements

Four years ago, I came to Glasgow to start my PhD study. This journey of physics research turned out to be fruitful, from where my knowledge about research has grown. At this time to submit this thesis, there are many to whom I would like to show my thanks.

First of all, I would like to thank my supervisor, Prof. Miles Padgett, who guides me all the way through my PhD study. His illuminating direction had led me to the world of real research! His consistent devotion has shown me how to develop a simple idea into a successful experiment. From him I learned how to think as a physicist. To choose to study in the optics group led by Miles is my best choice. I would like to thank Dr. Matthew Edgar, for his patient and consistent support during my PhD. Since my second year Matt has come to help me with my experiment, from where I picked up many useful experimental skills. He also spent a lot of time on my academic writing in English.

I would like to thank Dr. Sonia Franke-Arnold, for her supervision of my PhD process. For Dr. Graham Gibson, thanks for his help and support in the lab. For Dr. Richard Bowman, thanks for his programming support in the single-pixel imaging experiment. Thanks for all the co-authors in my papers and all other people who has given their useful suggestion on my work. Thanks for QiQi, Yiwei, Dr. Daniel Tasca, Dr. David Phillips, Dr. Jacq Romero, Dr. Johannes Courtial, Dr. Neal Radwell, Dr Mike Lee, Reuben Aspden, Steve Welsh, Dr. Lixiang Chen and other friends and officemates for all the useful discussion. Thanks for their help and accompany to my life in Glasgow. Apologise if there are names I missed. Thanks for everyone I know during my study and your help.

At last but maybe the most important as to everyone, I would like to thank my family, especially my parents, for their devoted support to my study. All these years I was far away from home and spent little time together with them. As their only child I owe too much to mum and dad. I wish all my best to them.

Contents

Declaration of Authorship	i
Abstract	iii
Acknowledgements	iv
List of Figures	viii
List of Publications	xiii
1 Introduction	1
2 Ghost Imaging	5
2.1 Light interference	6
2.1.1 First-order coherence	6
2.1.2 Second-order interference and Hanbury-Brown-Twiss interferometer	8
2.2 Quantum ghost imaging	10
2.3 Classical ghost imaging	15
2.3.1 Ghost imaging using classical momentum correlations	15
2.3.2 Theoretical background for pseudo-thermal GI	16
2.3.3 Speckle statistics	19
2.3.4 Experimental demonstrations	21
2.4 Computational ghost imaging	22
2.4.1 Theoretical background	23
2.4.2 Experimental demonstrations	23
2.4.3 Computational GI and single-pixel camera: comparison between structured illumination and coded apertures	24
2.5 Ghost diffraction	26
2.6 Conclusion	27
3 Normalised Ghost Imaging	28
3.1 Introduction to existing iterative algorithms	29
3.1.1 Traditional ghost imaging algorithm	30
3.1.2 Differential ghost imaging algorithm	32

3.2	Normalized ghost imaging	33
3.3	Signal-to-noise ratio analysis	34
3.4	Experimental setup	37
3.4.1	General description	38
3.4.2	Spatial light modulator and modulated speckles	38
3.5	Experiment results	40
3.5.1	Experimental comparison between different algorithms	40
3.5.2	Experimental SNR Analysis	42
3.6	Normalization in matrix inverse algorithms	43
3.6.1	Matrix inverse algorithms and compressive sensing	43
3.6.2	Normalized compressive ghost imaging	45
3.7	Conclusion	46
4	3D Computational Imaging with Single-Pixel Detectors	48
4.1	Limitations of the existing GI experiment methodology	49
4.2	Computational imaging with structured illumination	52
4.2.1	Experiment setup	52
4.2.2	Digital light projectors and digital micromirror devices	53
4.2.3	Depth of field of the projection system	55
4.3	Differential computational imaging	57
4.3.1	Acquisition of differential signals	58
4.3.2	Experimental results	59
4.4	3D computational imaging utilising structured illumination	62
4.4.1	Computational imaging setup with multiple single-pixel detectors	64
4.4.2	Shading property of computational images	64
4.4.3	Computational imaging with multiple illumination directions	68
4.5	3D GI reconstruction using photometric stereo	68
4.5.1	3D imaging methodology	69
4.5.2	Shape from shading to photometric stereo	70
4.5.3	System calibration	73
4.5.4	3D reconstruction algorithm	74
4.5.5	Quantitive analysis of the 3D profile	75
4.6	Computational imaging with single detectors detecting object light re- flected by a wall	76
4.7	Conclusion	77
5	Single-Pixel Real-Time Video	86
5.1	Coded masking based on Hadamard patterns	88
5.1.1	Hadamard matrix	88
5.1.2	Hadamard patterns in iterative correlation imaging	89
5.2	Computational imaging using a commercial light projector	93
5.2.1	Sequential processing	95
5.2.2	A 110 Hz system by exploiting bit-plane display	95
5.2.3	A 660 Hz GI system	96
5.3	Real-time video from a computational imaging system with single-pixel detectors	98
5.3.1	Experimental setup	98

5.3.2	Single-pixel computational video	99
5.4	Real-time video from a single-pixel camera	100
5.5	Noise reduction using an optimiser	103
5.6	Conclusion	106
6	Conclusion and Future Work	108
 Bibliography		 113

List of Figures

2.1	Sketch of the Young's double-slit experiment.	7
2.2	Schematic diagram of the Hanbury Brown-Twiss stellar intensity interferometer. Light that has travelled along different paths \mathbf{r}_1 and \mathbf{r}_2 is detected by two photomultiplier P_1 and P_2 . Signals are then sent to a coincidence counter for coherence measurement. During the measurement, one detector (P_2) is kept stable while the other is moved in the transverse direction (P_1) relative to the incident light.	9
2.3	Illustration of Quantum ghost imaging setup. Entangled photon pairs generated from a nonlinear crystal is split by a polarised beamsplitter(PBS) into two beams. The reference beam is detected by a scanning pinhole detector to record its spatial information. And the object beam interacts with the object and then collected by a single-pixel (bucket) detector. The two beams are correlated through a computer algorithm.	12
2.4	Illustration of momentum conservation for (a) collimated and (b) non-collimated SPDC.	13
2.5	Klyshko's advanced wave illustration of quantum GI for (a) a far-field correlation and (b) the experiment in [1].	14
2.6	Classical ghost imaging setup using classical correlating momentum.	16
2.7	(a) Illustration of two-beam correlation imaging system. The input E and a is for quantum and thermal cases separately. (b) Illustration of the input and output of a non-polarising beamsplitter.	17
2.8	Illustration pseudo-thermal GI using speckles. Speckles are split by a non-polarised beamsplitter into two identical beams. The reference beam is captured by a CCD camera (D_2), and the object beam interacts with the object (O) and then collected by a bucket detector (D_1). D_2 and the object are placed in the same distance away from the speckle source.	21
2.9	Comparison of (a) a conventional pseudo-thermal GI and (b) a computational GI setup. In computational GI, speckles are generated by a spatial light modulator and predicted by the controlling hologram. The reference beam together with the beamsplitter is removed from a conventional GI setup.	24
3.1	Illustration of thermal GI. Speckles pass through a beamsplitter (BS) and are separated into two identical beams. The object (signal) beam (I_S) illuminates the object and is collected by a bucket detector (D_1). The reference beam (I_R) is recorded by a CCD (D_2).	30
3.2	Simulation TGI reconstruction of a 2D binary transmissive <i>Packman</i> and its ($1s, 0s$) inverse. Both results are obtained after a number of iterations equal to their pixel number. The packman on the right has more 0s in its area so it is more blocked, while its inverse on the right is more transmissive.	32

3.3	Computational ghost imaging setup used in the experiment. A spatial light modulator (SLM) is used to generate a random speckle field. A beam splitter (BS) is used to measure a reference signal R on a bucket detector before the object. The signal, S , is measured on a bucket detector which collects the light transmitted after the object.	39
3.4	Illustration of a intensity spatial light modulator setup. Linear polarised laser passes through a half-wave plate and is modulated by the SLM, gets through the half-wave plate again. The transmissive light from the polarised beamsplitter (PBS) contains spatial information determined by the hologram.	40
3.5	(a) A typical speckle pattern hologram. (b) The measured intensity distribution of the speckle pattern (blue) and an exponential curve (red). . .	41
3.6	Experimental results (middle column) for TGI, DGI and NGI reconstruction algorithms as they evolve (10, 100, 1000 and 10000 iterations from left to right, respectively) with the corresponding simulated results (right column). The transmissive object is shown in the lower right. The bottom row shows the evolution for reconstructing the object with the NGI algorithm using a single detector and predicting the reference signal R , termed here the SNGI algorithm.	42
3.7	Experimental results of a <i>Packman</i> (top row) and anti- <i>Packman</i> (bottom row) from different GI algorithms.	43
3.8	Signal-to-noise ratio's for DGI, NGI, SNGI and TGI versus transmitting area. Transmitting ratio is defined as the ratio between the transmitting area of the object and the area of the speckle field.	44
3.9	(a) Experimental result of Normalized known vector reconstruction method (S/R) having $SNR = 9.95$. (b) Standard CGI reconstruction from S having $SNR = 7.39$	46
4.1	Reconstructed image of a 3D reflective object using computational GI setup discussed in Chapter. 3. The object contains two 3D-printed letters "G" and "U".	51
4.2	GI reconstruction of a transmissive object by measuring the transmissive (a) an reflective (b)photons.	52
4.3	Illustration of the single-pixel computational imaging experimental setup. The light projector illuminates the object (head) with computer generated random binary speckle patterns. The light reflected from the object is collected by a single pixel photodetector. The signals from the photodetector are measured by the computer via the analogue-digital converter, and used to reconstruct a correlation image.	54
4.4	Illustration of light projector. RGB light are emitted from three photodiodes and passed onto the DMD chip. The modulated light field reflected by the DMD mirrors are projected by a lens onto the image plane of the DMD.	55
4.5	An illustration of the "on" and "off" states of a DMD pixel (a) and a modulated light pattern.	56

4.6	Measurement of depth of focus of the DLP system. (a) Image of black and white stripes obtained in the focal plane of the projection lens. (b) The image of the same pattern obtained with the contrast reduced to 50%. (c) shows the cross view of the magnitude of the pattern in the focal plane (black line), front out-of-focal plane (red line) and back out-of-focal plane (green line).	57
4.7	Illustration of speckles and their inverse. l_1 and l_2 are two speckles, and l'_1 and l'_2 are the inverse. The differential signals are obtained by subtracting S' from S	58
4.8	Differential signals. (a) Acquisition of 2000 samples. It contains signals for one light pattern and its inverse and two pair of triggers. (b) Signals of one frame of illumination from the DLP. (c) Filter for signals in one frame. (d) The differential signals.	60
4.9	Source ghost image reconstructed using the TGI iterative algorithm iteratively from 1000 to 1,000,000.	61
4.10	2D computational images of a sample skull and a toy camel.	62
4.11	(a) Signals of one frame illumination obtained with room light on. (b) The rendered differential signals. (c) A reconstruction of a toy skull without room light compared with the same reconstruction with room light on (d).	63
4.12	Illustration of the experimental setup used for 3D surface reconstructions. The light projector illuminates the object (head) with computer generated random binary speckle patterns. The light reflected from the object is collected on 4 spatially separated single pixel photodetectors. The signals from the photodetectors are measured by the computer via the analogue-digital converter, and used to reconstruct a ghost image for each photodetector.	65
4.13	Source ghost images from each photodetector employed in the system, reconstructed using the TGI iterative algorithm iteratively from 1000 to 1,000,000. The spatial information in each image is identical, however the apparent illumination source is determined by the location of the relevant photodetector, indicated underneath.	66
4.14	Validation of imaging system reciprocity. Simplified schematic of a conventional imaging system (b) and the computational imaging system (e) with the illustration of light propagation (a) and (c) respectively. In a conventional imaging system the light travels from the source to the object and the reflected light is measured on a spatially resolving detector. In our computational imaging system, a spatially resolved light pattern is projected on the object and the total reflected intensity is measured on a single-pixel detector. The images acquired from both approaches ((c) and (f)) are equivalent as shown indicated below, whereby the apparent lighting of the object is determined by the location of the non-imaging element.	79
4.15	Computational images obtained with different illumination directions: (a) from the left side of the head and (b) from the right side of the head. . . .	80
4.16	Measurement of Lambertian surface properties. Measured reflected power from a flat polystyrene surface (circles) and the theoretical curve representing a cosine function (solid line).	80
4.17	2D reconstruction of a polystyrene ball	81
4.18	3D reconstruction of a polystyrene ball	81

4.19	Process of the 3D Reconstruction.	81
4.20	Surface Normals and Reflection. (a)-(c) are surface normals in the x , y and z direction and Reflection.	81
4.21	Rendered views of the reconstructed facial surface derived by integration of the surface normal data and overlaid with the reflectance data (movie included in supplementary material).	82
4.22	Rendered views of the reconstructed facial surface derived by integration of the surface normal data and overlaid with the reflectance data (movie included in supplementary material).	82
4.23	The matched ghost imaging (green) and stereo-photogrammetric (blue) reconstructions of the mannequin head, from frontal (a) and profile (b) viewpoints, and with anatomical landmarks (colour coded green and blue respectively) added.	83
4.24	(a) Illustration of an imaging process of a computational imaging system with a single-pixel detector, where the single-pixel detector measures object light reflected by a wall. (b) Imaging process of a camera where the object is illuminated by light reflected by a wall.	84
4.25	Images obtained from a computational imaging system with four single-pixel detectors. All four detectors are arranged in a way that light scattered from the object can not illuminate the detectors directly, but can only be reflected into the detection windows from pieces of polystyrene planes.	84
4.26	Side view of a 3D reconstruction using the four images shown in Fig. 4.25.	85
5.1	(a) A 64×64 Hadamard matrix and (b) the derived 2D pattern from the 14th row.	90
5.2	Reconstruction of a toy skull from a full set of Hadamard derived patterns. The Hadamard derived patterns are in 64×64 derived from a 4096×4096 Hadamard matrix. From top-left to bottom-right are results after 300, 600, 900, 1200, 1500, 1800, 2100, 2400, 2700, 3000, 3300, 3600, 3800, 4000 and 4096 iterations.	91
5.3	TGI reconstruction of a toy skull using 4096 random binary patterns.	92
5.4	(a) Signal distribution of the 4096 Hadamard derived patterns from the reconstruction shown in Fig. 5.2, and (b) signals of the randomised Hadamard derived patterns from the reconstruction shown in Fig. 5.6.	93
5.5	A Hadamard derived pattern derived from a row of a 4096×4096 Hadamard matrix (left) and its randomised format (right).	94
5.6	Reconstructions from a whole set of randomised Hadamard derived patterns. The randomised Hadamard derived patterns are in 64×64 pixels derived from a 4096×4096 Hadamard matrix. From top-left to bottom-right are results from after 300 up to 4096 iterations, with an increasing step of 300 iterations between any two neighbouring ones.	94
5.7	Sequential experiment procedure of GI using a <i>Light Commander</i>	95
5.8	Signals in a frame which are associated to 11 different light patterns ($p_1 - p_{11}$). The two bit planes on the left end are used as triggers.	96

5.9	Illustration of a fast single-pixel computational imaging system. Uniform light is directed to the DMD, modulated into binary patterns and then displayed onto the object by a projection lens. Reflected signals are collected by three single-pixel detectors for red, green and blue light and then sent to a computer.	100
5.10	Video frames from a 10 Hz single-pixel computational imaging system in 4s. Each image is obtained from the correlation of 1024 Hadamard derived patterns in 32×32 pixels, which is finished in 0.1 Hz. The scene is about a Rubik's cube rotated by hands.	101
5.11	Illustration of a fast single pixel camera. Object under the ambient light illumination is imaged onto the DMD. Light is then split by a composite dichroic beamsplitter (X-Cube) into three channels for red green and blue light, each being detected by a unfiltered single-pixel detector and sent to a computer.	102
5.12	Video frames from a 10 Hz single pixel camera in 4s. Each image is obtained from the correlation of 1024 Hadamard derived patterns in 32×32 pixels, which is finished in 0.1 Hz. The scene is about a Rubik's cube rotated by hands.	103
5.13	Video frames of a moving toy robot from TGI algorithm (a) without optimisation and (b) with optimisation. Each image is obtained using correlation of 1024 32×32 Hadamard derived patterns.	105
5.14	Video frames of a moving toy robot from TGI algorithm (a) without optimisation and (b) with optimisation. Each image is obtained using correlation of 1024 32×32 random binary patterns.	105
5.15	Video frames of a moving toy robot from TGI algorithm and after optimisation. Each image is obtained using correlation of 4096 64×64 Hadamard derived patterns.	106

List of Publications

- [1] B. Sun, S. S. Welsh, M. P. Edgar, J. H. Shapiro, and M. J. Padgett. Normalized ghost imaging. *Opt. Express*, 20(15):16892–16901, Jul 2012. doi: 10.1364/OE.20.016892.
- [2] B. Sun, M. P. Edgar, R. Bowman, L. E. Vittert, S. Welsh, A. Bowman, and M. J. Padgett. 3d computational imaging with single-pixel detectors. *Science*, 340(6134): 844–847, 2013. doi: 10.1126/science.1234454.
- [3] S. S. Welsh, M. P. Edgar, R. B., P. J., B. Sun, and M. J. Padgett. Fast full-color computational imaging with single-pixel detectors. *Opt. Express*, 21(20):23068–23074, Oct 2013.
- [4] Baoqing Sun, Matthew Edgar, Richard Bowman, Liberty Vittert, Stephen Welsh, Adrian Bowman, and Miles J Padgett. 3d computational ghost imaging. In *Quantum Information and Measurement*, pages W1–1. Optical Society of America, 2013.
- [5] Baoqing Sun, Matthew Edgar, Richard Bowman, Liberty Vittert, Stephen Welsh, Adrian Bowman, and Miles Padgett. 3-dimensional computational ghost imaging. In *Frontiers in Optics*, pages FW5D–2. Optical Society of America, 2013.
- [6] Baoqing Sun, Matt Edgar, Richard Bowman, Liberty Vittert, Stephen Welsh, Adrian Bowman, and Miles Padgett. Differential computational ghost imaging. In *Computational Optical Sensing and Imaging*, pages CTu1C–4. Optical Society of America, 2013.
- [7] Stephen Welsh, Matthew Edgar, Richard Bowman, Baoqing Sun, and Miles Padgett. Near video-rate linear stokes imaging with single-pixel detectors. *Journal of Optics*, 2014.

To my parents.

Chapter 1

Introduction

Imaging is the process of representing an object in an image. In a typical imaging system, light from the object is collected by an imaging lens and an image is formed at a particular focal plane, whereupon a sensor (or a screen) is normally placed. Since the image contains information in two dimensions (2D), the sensor has to be sensitive in 2D. That is to say, the detector employed to record an image has to contain many pixels. An alternative approach for imaging, which is the subject this thesis, allows single-pixel detectors to be used, i.e. those without spatial resolution. This so-called single-pixel imaging technique can trace its history back to the technique of raster scanning, a technique in which an image can be recorded or displayed, pixel by pixel. However, the single-pixel imaging systems discussed in this thesis originated from the field of quantum “ghost” imaging.

In 1995, a novel imaging technique called “ghost imaging” (GI) was demonstrated by using quantum entangled photon pairs generated from spontaneous parametric down conversion (SPDC) [1]. This approach relied on the use of strong spatial correlations between the positions of pairs of entangled photons. In the imaging process, these entangled photons were separated at a beam splitter and propagated along two separate optical paths. One photon was permitted to interact with an object and subsequently recorded by a single-pixel detector, however the other photon, which does not interact with the object is measured such that its spatial information is recorded. Neither of the two measurements is sufficient to provide an image alone, but their correlation does

indeed enable the spatial information of the object to be retrieved. As this technique seemingly allows a image to be produced using the spatial information recorded by photons which did not interact with the object it was termed “ghost” imaging. Since GI was first conducted using quantum entanglement, it was believed to be intrinsically a quantum phenomenon, and is referred to herein as quantum GI.

Subsequent demonstrations and theoretical analysis proved that GI could also be achieved using a classical light source, indicating that quantum entanglement and non-locality provides only a means for utilising strong spatial correlations but is not necessary. Indeed, any two beams containing spatial correlation are able to produce a “ghost” image using the same technique. In 2004, a classical GI system based on correlation measurement of pseudo-thermal speckles was proposed and subsequently demonstrated [2–4]. In such systems the pseudo-thermal speckle beams are generated by passing a laser beam through a changing phase diffuser, and split by a beam splitter along two separate paths. Similar to quantum GI, one light beam, the object beam, interacts with the object and is subsequently measured by a single-pixel detector, whereas the other beam, the reference beam, does not interact with the object and is instead measured by a device with spatial resolution, capable of resolving the speckle statistics.

In 2008, a simplified version of classical GI, called computational GI, was proposed [5]. By using a spatial light modulator (SLM), the speckle characteristics can be computationally controlled and their propagation behaviour theoretically predicted, rendering the use of the beam splitter and spatially resolving detector unnecessary, and resulting in a true single-pixel imaging system.

The work presented herein begins with an experiment in computational GI, whereupon the computer algorithm and experimental apparatus used is shown to have a significant impact on the quality of the images obtained. Most experimental demonstrations in the field of computational GI at the time of this research could arguably be considered as proof of principle, and hence relatively simple binary transmissive objects were employed. A rigorous quantitative analysis is made on the our results when compared to existing approaches.

The goal to improve the performance and quality of reconstructions via computational GI led the research to instead utilise a digital light projector rather than an SLM and laser source. With this approach we showed that high-quality 2D images of large 3 dimensional (3D) objects could be obtained. A distinguishing property of a single-pixel computational imaging system is that the shading properties of an image are determined by the detecting direction, while the shape of the image is determined by the illumination direction. This is reciprocal to a camera system, where detecting direction determines the shape and the illumination direction determines the shading. Hence, in a computational imaging system with several single-pixel detectors, each detector will produce a computational image, all of which are in the same shape but different shadings. By taking advantage of a technique called “photometric stereo” we demonstrated a new approach to high-quality 3D image reconstruction by implementing several single-pixel detectors in conjunction with a device capable of producing structured illumination.

The display rates afforded by microelectromechanical systems (MEMS) based devices, demanded a considerable effort in the signal processing and analysis pipeline in order to perform image reconstruction efficiently, which subsequently moved the goal of the research to providing “real-time” colour video. This research therefore provides an important contribution towards the application of single-pixel detectors for imaging at wavelengths where detector arrays are expensive or non-existent.

The rest of this thesis is arranged as follows: in chapter 2 the background of GI is introduced. The development of GI from quantum to pseudo-thermal to computational setups is discussed. In chapter 3 the normalised correlation algorithm called “normalised ghost imaging” (NGI) is developed in a computational GI system. Comparison between NGI and other algorithms is done with both simulation and experimental results. the normalisation method is also employed utilising compressive sensing techniques. In chapter 4, a 3D computational imaging system utilising single-pixel detectors is detailed. In chapter 5, a system capable of producing “real-time” video is outlined. With this experimental hardware there are two distinct imaging approaches which are closely related: a computational imaging system using single-pixel detectors employing structured illumination or a computational imaging system using single-pixel detectors employing coded

masking, also known as a single-pixel camera. I summarise my findings and conclude in chapter 6.

Chapter 2

Ghost Imaging

Ghost imaging (GI) is a technique that utilises correlation measurements of light to produce images. There are different categories of GI, which depend on the type of light source and the experimental apparatus employed, called quantum, classical and computational. In both quantum and classical GI, the object is reconstructed by using two correlated beams: the reference beam which is captured by a spatially resolving detector, i.e. a CCD camera; and the object beam which, after interacting with the object, is collected by a single-pixel detector (bucket detector). By correlating the light distribution captured from the reference beam along with the bucket signal, an image of the object can be reconstructed using a computer algorithm.

The principle of GI was exploited by Klyshko from his advanced wave picture of quantum entanglement [6]. In 1995, the first GI experiment was realised utilising entangled photon pairs generated from spontaneous parametric down-conversion (SPDC) and thus was interpreted to be a quantum effect [1]. Subsequently however, it was demonstrated that GI could also be achieved by using a classical light source [7], indicating that fundamentally this phenomenon was a consequence of spatial correlation not entanglement. In 2008, a modified GI system called computational GI was proposed, whereby a device capable of producing programmable light fields is employed [5]. In this arrangement, knowledge of the incident light field is stored in computer memory, negating the requirement for a detector array to measure the reference beam, resulting in a simpler experimental setup. Since this type of configuration enables images to be formed using

a single-pixel detector, there is similarity with other imaging approaches, namely the single-pixel camera.

In this chapter I provide a concise theoretical background for the underlying principles of ghost imaging, starting with an introduction to the interference of light, followed by an overview of the experimental developments from quantum to classical to computational systems. In particular, I highlight some limitations of the existing work in the field and detail how some of these are overcome by the contents of this thesis.

2.1 Light interference

As will be discussed, GI depends upon correlation measurements between two beams, which can be regarded as a phenomenon of second-order correlation of light. Here the first and second order coherence functions of light interference are reviewed from a classical and quantum perspective. Most of the theory discussed here can be found in references [8–10].

2.1.1 First-order coherence

We start by reviewing Young’s double-slit interference as sketched in Fig. 2.1. Classically, as light propagates a distance of \mathbf{r} from a source it can be described by its complex amplitude

$$E(\mathbf{r}, t) = E_i \cdot e^{-i\omega t + i\phi}, \quad (2.1)$$

where E indicates the amplitude, ω is the angular frequency, ϕ is the phase, and $t = |\mathbf{r}|/c$ where c is the speed of light. In Fig. 2.1, light diffracted from the two slits S_1 , S_2 propagating after \mathbf{r}_1 and \mathbf{r}_2 arrives at a detection position P . The amplitude at any point on the detection plane can be written as the linear superposition of two waves,

$$E(\mathbf{r}, t) = K_1 E(\mathbf{r}_1, t_1) + K_2 E(\mathbf{r}_2, t_2), \quad (2.2)$$

where K_1 and K_2 represent the complex geometric factors that depend on the propagation of \mathbf{r}_1 and \mathbf{r}_2 respectively. The intensity $I(\mathbf{r})$, is then measured using a light-sensitive

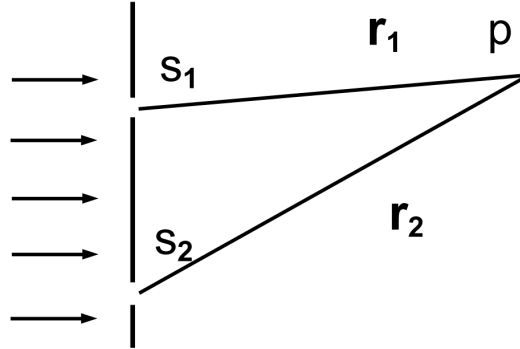


FIGURE 2.1: Sketch of the Young's double-slit experiment.

detector, which is assumed to have a long response time and therefore is only able to measure the average light intensity,

$$I(\mathbf{r}) = \langle |E(\mathbf{r}, t)|^2 \rangle, \quad (2.3)$$

where $\langle \dots \rangle$ denotes the time average. The intensity of Eq. 2.2 can be expressed as

$$I(\mathbf{r}) = |K_1|^2 \langle |E(\mathbf{r}_1, t_1)|^2 \rangle + |K_2|^2 \langle |E(\mathbf{r}_2, t_2)|^2 \rangle + 2\text{Re}[K_1^* K_2 \langle E^*(\mathbf{r}_1, t_1) E(\mathbf{r}_2, t_2) \rangle]. \quad (2.4)$$

where $*$ denotes the complex conjugate. On the right hand side of Eq. 2.4, the first two terms describe the intensities from the two waves, while the third term describes their interference. The first-order coherence function is defined as

$$G^{(1)}(\mathbf{r}_1, t_1; \mathbf{r}_2, t_2) = \langle E^*(\mathbf{r}_1, t_1) E(\mathbf{r}_2, t_2) \rangle. \quad (2.5)$$

Equation 2.5 can be normalised as

$$g^{(1)}(\mathbf{r}_1, t_1; \mathbf{r}_2, t_2) = \frac{\langle E^*(\mathbf{r}_1, t_1) E(\mathbf{r}_2, t_2) \rangle}{\sqrt{\langle |E(\mathbf{r}_1, t_1)|^2 \rangle \langle |E(\mathbf{r}_2, t_2)|^2 \rangle}}, \quad (2.6)$$

which is called normalised first-order coherence function, or degree of first order coherence function. It has a value of 1 and 0 for complete coherent light and complete

incoherent light respectively, and for partially coherent light, $0 < g^{(1)} < 1$.

From a quantum perspective, the light field is quantised and represented by $\mathbf{E}(\mathbf{r}, t)$, which can be separated into the sum of its positive and negative frequency parts

$$\mathbf{E}(\mathbf{r}, t) = \mathbf{E}^{(+)}(\mathbf{r}, t) + \mathbf{E}^{(-)}(\mathbf{r}, t), \quad (2.7)$$

where $\mathbf{E}^{(+)}(\mathbf{r}, t)$ and $\mathbf{E}^{(-)}(\mathbf{r}, t)$ contains the annihilation and creation operators respectively. The corresponding first-order correlation function is expressed as

$$G^{(1)}(\mathbf{r}_1, t_1; \mathbf{r}_2, t_2) = \langle \mathbf{E}^{(-)}(\mathbf{r}_1, t_1) \mathbf{E}^{(+)}(\mathbf{r}_2, t_2) \rangle. \quad (2.8)$$

2.1.2 Second-order interference and Hanbury-Brown-Twiss interferometer

While the first-order coherence function describes the field-field interference of light, a second-order coherence function describes the intensity-intensity, or photon-photon interference. Similar to Eq. 2.5, the classical second-order coherence function can be written as

$$G^{(2)}(\mathbf{r}_1, t_1; \mathbf{r}_2, t_2) = \langle E^*(\mathbf{r}_1, t_1) E(\mathbf{r}_2, t_2) E^*(\mathbf{r}_2, t_2) E(\mathbf{r}_1, t_1) \rangle, \quad (2.9)$$

and the normalised version of Eq. 2.9 is

$$g^{(2)}(\mathbf{r}_1, t_1; \mathbf{r}_2, t_2) = \frac{\langle E^*(\mathbf{r}_1, t_1) E^*(\mathbf{r}_2, t_2) E(\mathbf{r}_2, t_2) E(\mathbf{r}_1, t_1) \rangle}{\langle |E(\mathbf{r}_1, t_1)|^2 \rangle \langle |E(\mathbf{r}_2, t_2)|^2 \rangle}. \quad (2.10)$$

Equation 2.10 can be understood as the degree of intensity correlation of two light waves at \mathbf{r}_1 and \mathbf{r}_2 respectively. In quantum theory, Eq. 2.9 is expressed as

$$G^{(2)}(\mathbf{r}_1, t_1; \mathbf{r}_2, t_2; \mathbf{r}_3, t_3; \mathbf{r}_4, t_4) = \langle \mathbf{E}^{(-)}(\mathbf{r}_1, t_1) \mathbf{E}^{(-)}(\mathbf{r}_2, t_2) \mathbf{E}^{(+)}(\mathbf{r}_3, t_3) \mathbf{E}^{(+)}(\mathbf{r}_4, t_4) \rangle. \quad (2.11)$$

In 1956, a second-order interference experiment at optical wavelengths, called Hanbury-Brown-Twiss (HBT) interference [11–13] was demonstrated. The original experiment

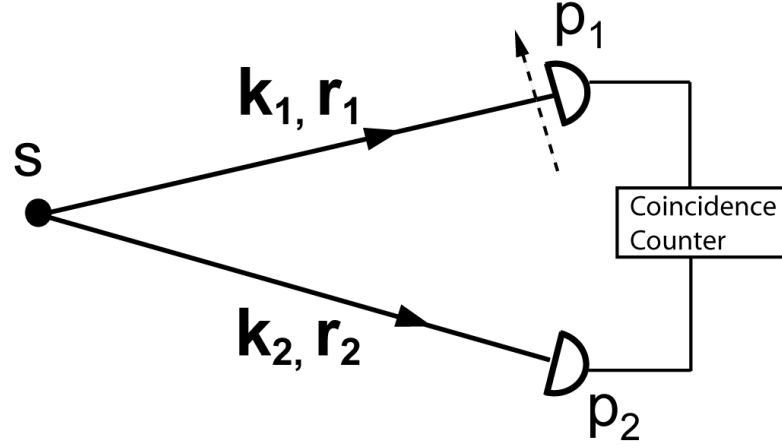


FIGURE 2.2: Schematic diagram of the Hanbury Brown-Twiss stellar intensity interferometer. Light that has travelled along different paths \mathbf{r}_1 and \mathbf{r}_2 is detected by two photomultiplier P_1 and P_2 . Signals are then sent to a coincidence counter for coherence measurement. During the measurement, one detector (P_2) is kept stable while the other is moved in the transverse direction (P_1) relative to the incident light.

was designed to observe light from the star Sirius in order to measure its diameter. More specifically, the HBT interferometer measured the angular separation between two different wave vectors \mathbf{k}_1 and \mathbf{k}_2 emitting from the star. Light from the star is filtered and measured by two separated photomultipliers P_1 and P_2 . An interference was observed between the two intensities by changing the relative transverse distance between the two detectors. The HBT effect was quite confusing when it was first announced. Simply speaking, it is difficult to understand how the phase information is conserved in this intensity to intensity correlation measurement.

The HBT interference patterns can be explained from both classical and quantum theory, and the results derived from the two theories are the same. Here only the classical results are shown. Classically, the interference of the intensities from the two detectors can be

derived as

$$\begin{aligned}
\langle I(\mathbf{r}_1, t) I(\mathbf{r}_2, t) \rangle &= \langle \{ |\mathbf{E}_{\mathbf{k}_1}|^2 + |\mathbf{E}_{\mathbf{k}_2}|^2 + [E_{\mathbf{k}_1} E_{\mathbf{k}_2}^* e^{i(\mathbf{k}_1 - \mathbf{k}_2) \cdot \mathbf{r}_1} + c.c.] \} \\
&\quad \times \{ |\mathbf{E}_{\mathbf{k}_1}|^2 + |\mathbf{E}_{\mathbf{k}_2}|^2 + [E_{\mathbf{k}_1} E_{\mathbf{k}_2}^* e^{i(\mathbf{k}_1 - \mathbf{k}_2) \cdot \mathbf{r}_2} + c.c.] \} \rangle \\
&= \langle (|\mathbf{E}_{\mathbf{k}_1}|^2 + |\mathbf{E}_{\mathbf{k}_2}|^2)^2 \rangle + \langle |\mathbf{E}_{\mathbf{k}_1}|^2 \rangle \langle |\mathbf{E}_{\mathbf{k}_2}|^2 \rangle [e^{i(\mathbf{k}_1 - \mathbf{k}_2) \cdot (\mathbf{r}_1 - \mathbf{r}_2)} + c.c.],
\end{aligned} \tag{2.12}$$

where *c.c.* stands for the complex conjugate. Notice that the two waves are filtered, therefore \mathbf{k}_1 and \mathbf{k}_2 have the same modules but different directions. The interference patterns is contained in the term $e^{i(\mathbf{k}_1 - \mathbf{k}_2) \cdot (\mathbf{r}_1 - \mathbf{r}_2)} + c.c..$

2.2 Quantum ghost imaging

Quantum GI utilises entangled photon pairs generated from spontaneous parameter down conversion (SPDC) to obtain an image. Entangled photon pairs generated from SPDC are separated into two beams: the object beam and the reference beam, which propagate along two separate paths. In the object beam, photons interact with an object and are subsequently measured on a detector with no spatial resolution (bucket detector). Meanwhile, the reference beam, which does not interact with the object is measured by a detector capable of resolving spatial information. Measurements from the two beams are then correlated, and after many photon pairs are used, an image is iteratively reconstructed. This “ghost” imaging technique can also be called correlation imaging, because it works by taking advantage of the spatial correlations of entangled photon pairs.

The first GI experiment was demonstrated by Pittman *et al.* in 1995 [1]. In this experiment, entangled photon pairs are generated from a beta barium borate (BBO) crystal that is cut at a degenerate type-II phase-matching angle to produce pairs of orthogonally polarised photons (as shown in Fig. 2.3). A 351.1-nm laser beam is used to pump the BBO crystal. Photon pairs that emerge from the crystal are separated by a polarised beam splitter (PBS) and propagated along different paths. A binary transmissive object is placed in the path of one photon, termed the object path, and a

lens is placed between the PBS and object. If the photon is transmitted through the object it is subsequently measured by a single-pixel detector sensitive to single photons, for example a single-photon avalanche detector (SPAD). A lens may also be used in conjunction with the detector, in order to ensure that the photon can be collected from the entire object. Meanwhile the orthogonally polarised photon that propagated along the other path, often termed the reference path, does not interact with the object and is detected by a scanning detector package, consisting of a multimode fibre whose output is mated with another SPAD. The aperture of the fibre is scanned in the transverse plane to photon propagation. A lens is also used in the reference path between the PBS and transverse plane of detection such that they are at the image plane. The output signals of the two detections are sent to a coincidence counting circuit with a narrow bandwidth acceptance window. By recording the coincidence counts as a function of the fibre's transverse plane coordinates in the reference beam, an image of the object can be seen in the reference arm. It is worth mentioning that a scanning procedure introduces a low optical efficiency at high resolutions. Thus to improve the sampling efficiency, a modified experimental setup of quantum GI utilising a camera with high quantum efficiency can be performed [14].

The ability to generate entangled photon pairs is an important tool for quantum GI as well as many other experiments in quantum optics. In SPDC, a nonlinear crystal is used to degenerate an incident high-energy photon into a pair of lower-energy photons [15–19]. SPDC is a parametric process, which means that light interacts with matter in such a way as to leave the quantum state of the material unchanged. Therefore both the energy and momentum is conserved in the process. The combined energy and momentum of the pair of photons is equal to the energy and momentum of the original photon. The conservation can be interpreted as phase-matching condition in the frequency domain. The energy conservation can be described as

$$\omega_s + \omega_i = \omega_p, \quad (2.13)$$

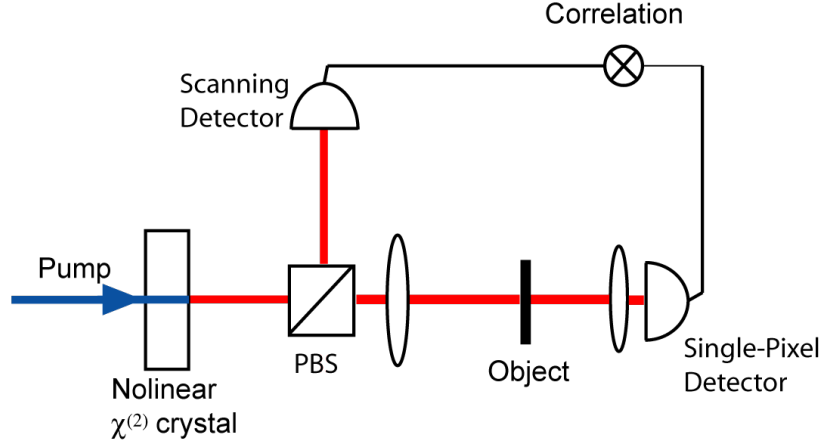


FIGURE 2.3: Illustration of Quantum ghost imaging setup. Entangled photon pairs generated from a nonlinear crystal is split by a polarised beamsplitter(PBS) into two beams. The reference beam is detected by a scanning pinhole detector to record its spatial information. And the object beam interacts with the object and then collected by a single-pixel (bucket) detector. The two beams are correlated through a computer algorithm.

where ω is the angular frequency for the pump (ω_p), signal (ω_s) and idle (ω_i) photons. And the momentum conservation can be described as

$$\mathbf{k}_s + \mathbf{k}_i = \mathbf{k}_p, \quad (2.14)$$

where \mathbf{k} stands for their wave vector. According to Eq. 2.13 and Eq. 2.14, the two entangled photons generated from SPDC always have the opposite (anti-correlated) transverse momentum in the near-field (Fig. 2.4), and will transferred into position anti-correlation in the far-field. On the other hand, as photon-pairs are generated from the same position in space, their positions are highly correlated in the near-field, and coincident at the image plane. Both the near-field correlation and far-field anti-correlation can be employed for imaging [20]. In the near-field quantum GI, the object and reference detector are both located in the image plane of the nonlinear crystal. Therefore the transverse spatial information of the object photons in the object plane can be represented by that of the entangled photons captured by the reference detector. During the imaging process, the two entangled photons work in such a way that the reference photon provide (transverse) spatial information, while the object photon indicates the transmission information on

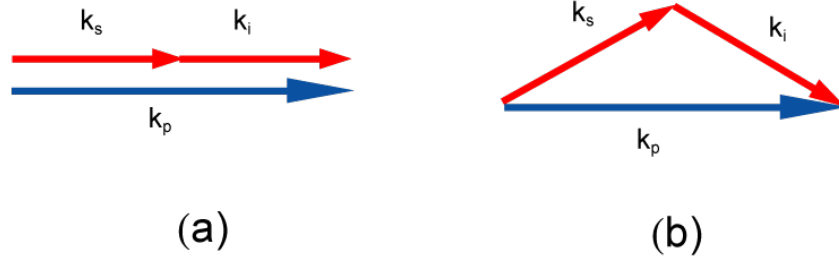


FIGURE 2.4: Illustration of momentum conservation for (a) collimated and (b) non-collimated SPDC.

corresponding position of the object. Signals from the bucket detector (bucket signals) work as triggers for the reference signals. If a photon transmits the object in the object beam and gets received by the bucket detector, the reference photon is recorded with related spatial information. The corresponding pixel in the reconstructed image will have a value of 1 for one photon. Otherwise, if a photon is blocked by the object, the corresponding pixel indicated by the entangled reference photon will appear as 0 in the image. After many photon pairs are used, the correlation of these two photons can be used to reconstruct an image of the object. In the far-field, the anti-correlation of momentum is transferred into anti-correlation of position. Thus measurements of the transverse position ρ of the reference photon corresponds to its entangled partner photon in position $-\rho$. The opposite sign renders an inverted image but with the spatial information of the object maintained.

Quantum GI can also be understood through Klyshko's advanced wave interpretation. In Klyshko's advanced wave interpretation, the time-space relation between the entangled photons from SPDC is explained in a geometrical method [6, 21, 22]. As two entangled photons emit from the crystal with opposite angles, the crystal plane can be regarded as a mirror upon where the two-beam system can be unfolded. The GI imaging system then can be treated like a conventional imaging system by replacing the single-pixel detector by a light source. Fig. 2.5(a) shows an example for the far-field GI setup. Light emits from the light source goes through the $4F$ system and images the object in the

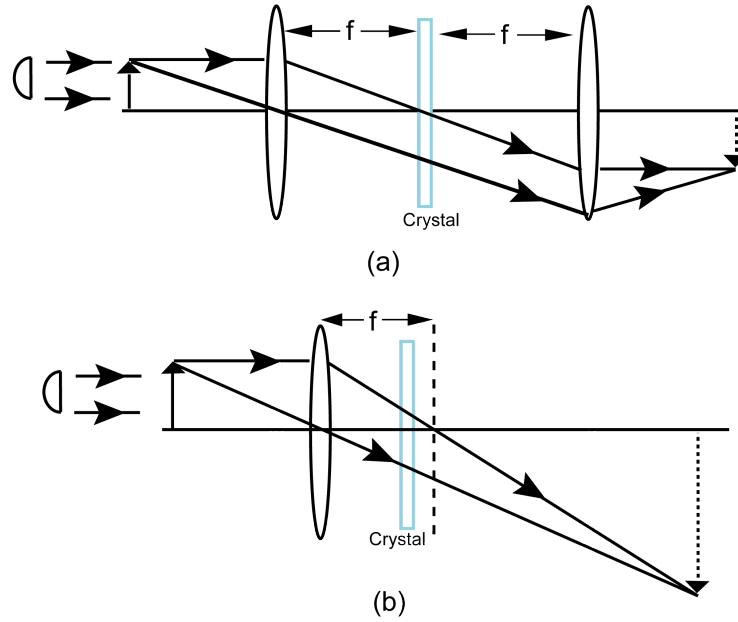


FIGURE 2.5: Klyshko's advanced wave illustration of quantum GI for (a) a far-field correlation and (b) the experiment in [1].

plane of the scanning detector. This illustration helps understand the magnification of the image reported in [1]. In their system a lens is placed in the object beam before the object. Unfolding the experiment setup upon the crystal plane we get Fig.2.5(b). The illustration reveals an imaging system of a thin focussing lens, and therefore the magnification of the image can be understood from the Gaussian thin lens equation.

In addition to GI experiments that make use of the amplitude component of the electric field, quantum entanglement can also be utilised for generating a non-local image of a phase object. In 2004, a quantum GI experiment was demonstrated on some pure phase objects [23]. It is worth mentioning here that in this experiment a pinhole is placed in front of each of the two detectors located in the object and reference paths. Prior to this it was predicted that any type of coincidence imaging technique using a bucket detector could not be used for a phase object [7]. However, when using a pinhole in front of the single-pixel detector, the system is rendered partially coherent in space, and therefore the intensity correlation in the two beams is related to their relative phase difference. In 2009 an experimental demonstration of a phase GI method using entangled photon pairs carrying orbital angular momentum (OAM) was performed [24]. In this work a phase

image is obtained by correlation measurements of OAM modes in the light propagating along the object and reference paths (also referred to by signal and idler beams). In addition, edge enhancement of the phase image can be achieved by inserting a phase filter in the reference beam.

2.3 Classical ghost imaging

Although the first GI experiment had been performed using entangled photons, and at the time was considered intrinsically a quantum phenomenon, it was soon suggested by others that this type of behaviour could also be achieved with some classical light sources, a claim contested by Abouraddy *et al.* [25]. However in 2002, Bennink *et al.* achieved the first classical GI demonstration using two classical-angular-correlated pulses [7]. This, as well as many subsequent experiments, led to the common understanding that the only requirement necessary for GI is spatial correlations between two light fields, be that quantum or classical. The discussion about whether or not entanglement is necessary, however, lasted for a long time [2, 26–34]. During this debate, it was realised that thermal speckles could also yield images in the same types of systems, first proposed in 2004 by Gatti *et al.* [2, 28] and thereafter demonstrated by experiments [3, 4].

2.3.1 Ghost imaging using classical momentum correlations

Figure 2.6 shows the first GI experiment using classical light. The light source employed here is a pair of laser beams with classical correlated angles, which is generated by chopping a laser beam and then deflecting it by a phase diffuser by a random variable amount. The beam is then separated by a 50 : 50 (non-polarised) beamsplitter (BS) so that the photons in the two beams contain correlated momentum distributions. In one beam, the object is located before a bucket detector. The bucket signal works as a trigger to the CCD camera in the other beam, in a way that the CCD signal is only recorded when the object beam is not blocked by the object. This is a classical analog to the quantum GI experiments, the difference is that the momentum correlation here is

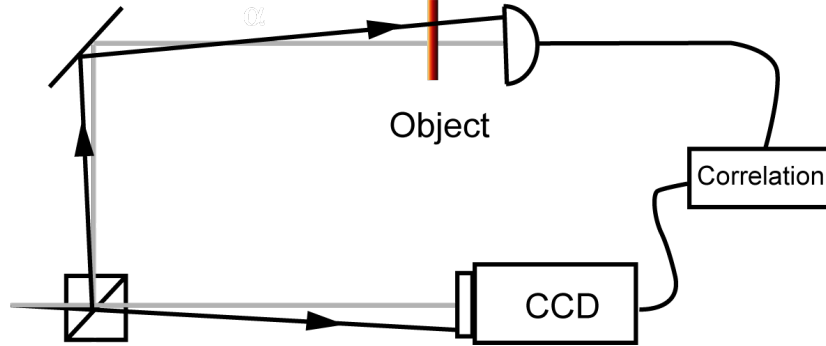


FIGURE 2.6: Classical ghost imaging setup using classical correlating momentum.

classical rather than quantum. It mimics the angular conservation without the quantum property of non-locality.

2.3.2 Theoretical background for pseudo-thermal GI

In 2004, Gatti *et. al.* proposed a classical ghost imaging setup using incoherent thermal speckle that can mimic all the features of entangled imaging [2, 28]. They considered a thermal light source that is split by a beamsplitter into two beams. They performed a comparison between this light source and an entangled photon pairs emitter in ghost imaging. Their analysis showed that such a classical light source can perform ghost imaging in both near-field and far-field, which is a full mimic of that from an quantum ghost imaging.

In a pseudo thermal GI setup, a speckle light field is passed through a BS, and the outputs of the BS can be regarded as a classical analogue to entangled photon pairs from the non-linear crystal used in SPDC. The input-output relation for a BS can be described as

$$E_1 = tE_3 + rE_4, E_2 = rE_3 + tE_4. \quad (2.15)$$

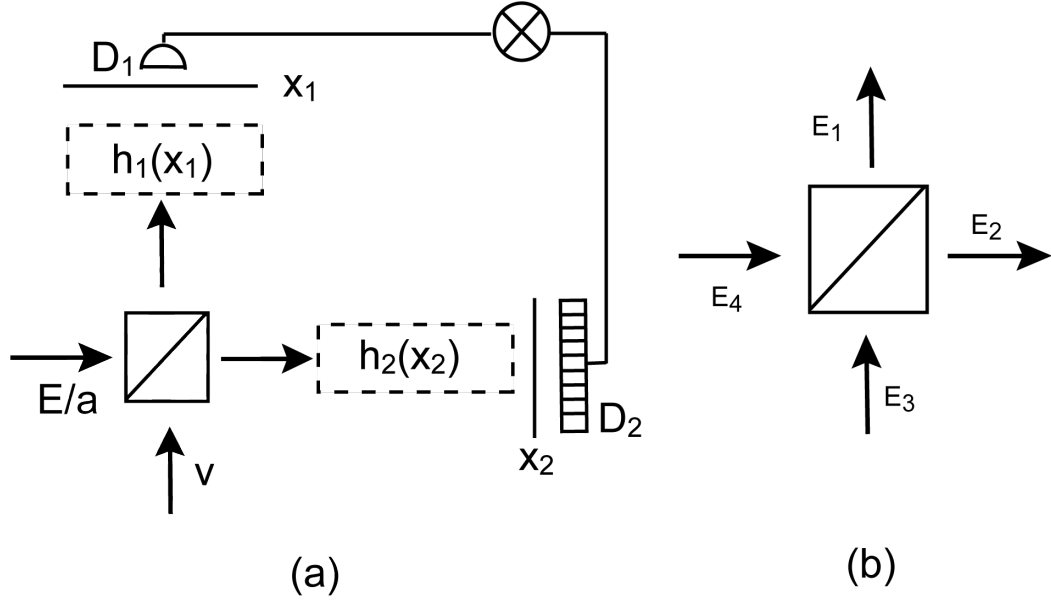


FIGURE 2.7: (a) Illustration of two-beam correlation imaging system. The input E and a is for quantum and thermal cases separately. (b) Illustration of the input and output of a non-polarising beamsplitter.

When using a 50 : 50 BS the reflection and transmission coefficients, r and t respectively, have equal magnitudes. Considering the case of pseudothermal GI, a thermal light field $E(\mathbf{x})$ passes through the BS, and the two output beams are

$$e_1(\mathbf{x}) = rE(\mathbf{x}) + tv(\mathbf{x}), \quad e_2(\mathbf{x}) = tE(\mathbf{x}) + rv(\mathbf{x}), \quad (2.16)$$

Here v is a vacuum field uncorrelated with $E(\mathbf{x})$. In comparison to this, the input-output relations of the crystal in a SPDC process is expressed as

$$e_i(\mathbf{q}) = U_i(\mathbf{q})E_i(\mathbf{q}) + V_i(\mathbf{q})E_j^\dagger(\mathbf{q}), \quad i \neq j = 1, 2. \quad (2.17)$$

Here $e_i(\mathbf{q}) = \int \frac{\mathbf{x}}{2\pi} e^{-i\mathbf{q}\cdot\mathbf{x}} e_i(\mathbf{x})$ is the signal ($i = 1$) or idler ($i = 2$) wave envelope operator at the output plane of the crystal, and † stands for Hermite conjugate. E_i are the corresponding fields at the input plane of the crystal in vacuum state. U_i and V_i are the gain functions.

In both of the quantum and classical cases, the two outgoing beams travel through two distinct imaging systems, which can be described by their impulse response functions $h(\mathbf{x}_i)(i = 1, 2)$. Thus, the fields at the detection planes are given as

$$c_i(\mathbf{x}_i) = \int d\mathbf{x}'_i h_i(\mathbf{x}_i, \mathbf{x}'_i) e_i(x'_i) + L_i(\mathbf{x}_i), \quad i = 1, 2 \quad (2.18)$$

where L_i is any possible losses in the imaging system, and depend on vacuum field operators, and the superscribe ' is to indicate the output plane of h . In the second-order correlation measurement, however, these possible losses can be ignored.

Information about the object is extracted from the spatial correlation function of intensities detected from D_1 and D_2 , as a function of position \mathbf{x} of the pixel of D_2

$$\langle I_1(\mathbf{x}_1) I_2(\mathbf{x}_2) \rangle = \left\langle c_1^\dagger(\mathbf{x}) c_1(\mathbf{x}) c_2^\dagger(\mathbf{x}) c_2(\mathbf{x}) \right\rangle. \quad (2.19)$$

Furthermore, the object information is concentrated in the correlation function of intensity fluctuations [27]:

$$G((x)_1, (x)_2) = \langle I_1(\mathbf{x}_1) I_2(\mathbf{x}_2) \rangle - \langle I_1(\mathbf{x}_1) \rangle \langle I_2(\mathbf{x}_2) \rangle, \quad (2.20)$$

where $\langle I_i(\mathbf{x}_i) \rangle = \left\langle c_i^\dagger(\mathbf{x}) c_i(\mathbf{x}) \right\rangle$ is the average intensity of the i th beam.

For thermal case, under Gaussian statistics assumption, by taking Eq. 2.16 into account, Eq. 2.20 can be written as:

$$G_C(\mathbf{x}_1, \mathbf{x}_2) = |rt|^2 \int d\mathbf{x}'_1 \int d\mathbf{x}'_2 h_1^*(\mathbf{x}_1, \mathbf{x}'_1) h_2(\mathbf{x}_2, \mathbf{x}'_2) \left\langle E^\dagger(\mathbf{x}'_1) E(\mathbf{x}'_2) \right\rangle^2. \quad (2.21)$$

On the other hand, Eq. 2.20 in the quantum case can be rewritten as

$$G_Q(\mathbf{x}_1, \mathbf{x}_2) = \left| \int d\mathbf{x}'_1 \int d\mathbf{x}'_2 h_1(\mathbf{x}_1, \mathbf{x}'_1) h_2(\mathbf{x}_2, \mathbf{x}'_2) \langle e(\mathbf{x}'_1) e(\mathbf{x}'_2) \rangle \right|^2, \quad (2.22)$$

where we define

$$\langle e_1(\mathbf{x}'_1) e_2(\mathbf{x}'_2) \rangle = \int \frac{d\mathbf{q}}{(2\pi)^2} e^{i\mathbf{q} \cdot (\mathbf{x}'_1 - \mathbf{x}'_2)} U_1(\mathbf{q}) V_2(-\mathbf{q}). \quad (2.23)$$

Comparing Eq. 2.21 and Eq. 2.22 reveals an analogy between the results in the quantum and thermal cases. The second order correlation $\langle E^\dagger(\mathbf{x}'_1)E(\mathbf{x}'_2) \rangle$ plays the same role in Eq. 2.21 as the correlation function $\langle e(\mathbf{x}_1)e(\mathbf{x}_2) \rangle$. In both cases, the fact that the modulus is outside the integral ensures the possibility of coherent imaging via correlation function. The correlation function $\langle E^\dagger(\mathbf{x}'_1)E(\mathbf{x}'_2) \rangle$ governs the properties of spatial coherence of the thermal source. A further analysis shows that this can happen in both near and far-fields, which is a complete mimic of quantum light in ghost imaging.

2.3.3 Speckle statistics

A speckle pattern is an intensity pattern produced from the interference of a set of wavefronts. This phenomenon has been intensively studied since the invention of continuous-wave lasers. When laser light is reflected from a rough surface such as a wall, a high-contrast, small-scale granular pattern can be observed. Although the incident laser light is in a relative uniform intensity, the intensity of the reflected patterns fluctuates across its space. This granularity is known as “speckle”.

The fluctuation of the speckle intensity is caused by the roughness of the surfaces where the light is reflected. According to Huygens, every point of the rough surface that is illuminated by the laser becomes a source of a spherical wave. And speckle is a result of the interference of these secondary waves. A wave can be described as a vector in the complex plane, with the amplitude and phase being represented by the length and direction of the vector respectively. The resultant vector at a point is the sum of all the vectors. As the phase and amplitudes of the secondary waves are totally random, so the sum of them gives a wave whose amplitude and therefore intensity varies randomly. This process can also be described as a 2 dimensional “random walk”. The sum of random vectors can be expressed as [35]

$$\mathbf{A} = Ae^{j\theta} = \frac{1}{\sqrt{N}} \sum_{n=1}^N a_n e^{j\phi_n}, \quad (2.24)$$

here N represents the number of complex vectors in the random walk. \mathbf{A} is the resultant vector, and A and θ are the amplitude and phase. The scaling factor $1/\sqrt{N}$ is to preserve

finite second order moments of the resultant vector. Under large number assumption, the resultant vector has a Rayleigh distribution of its amplitude

$$p_A(A) = \frac{\sqrt{A}}{\sigma^2} e^{-\frac{A}{2\sigma^2}}, \quad (2.25)$$

here σ is the variance of the amplitude. And the phase of the resultant vector is independent to the amplitude, with a uniform distribution in $[-\pi, \pi]$. Derived from the amplitude statistics, the intensities follows an exponential distribution:

$$p_I(I) = \frac{\sqrt{I}}{\sigma^2} e^{-\frac{I}{2\sigma^2}} \cdot \frac{1}{2\sqrt{I}} = \frac{1}{2\sigma^2} e^{-\frac{I}{2\sigma^2}}, \quad (2.26)$$

here I is the light intensity. And the moments of this distribution is

$$\bar{I}^q = (2\sigma^2)^q q!. \quad (2.27)$$

We find that the mean intensity $\bar{I} = 2\sigma^2$. Therefore the probability density function can be rewritten as

$$p_I(I) = (1/\bar{I}) e^{-I/\bar{I}}. \quad (2.28)$$

Equation 2.26 or 2.28 is an important character of fully developed speckles.

When an speckle is formed by illuminating a rough surface with a laser, it can be observed in the image plane. This speckle is called a subjective speckle pattern, because the speckle pattern structure changes depending on the viewing system. On the other hand, if laser light is scattered off a rough surface and then falls onto another surface, it forms an “objective speckle pattern”. Objective speckles are usually obtained in the far-field (the Fraunhofer region where Fraunhofer diffraction happens). Speckles can also be observed close to the scattering object. This is called near-field speckles. The statistics properties of a far-field speckle is determined by the form and dimension of the region hit by laser. For the near-field speckles, however, their statistical properties are mainly determined by the form and structure of the scattering object.

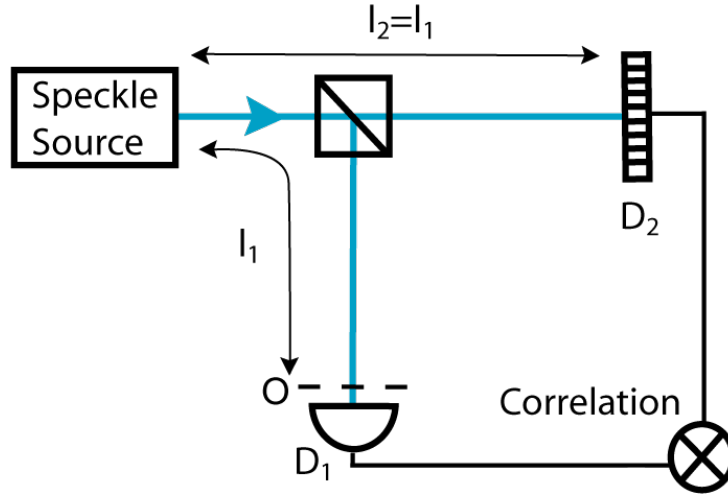


FIGURE 2.8: Illustration pseudo-thermal GI using speckles. Speckles are split by a non-polarised beamsplitter into two identical beams. The reference beam is captured by a CCD camera (D_2), and the object beam interacts with the object (O) and then collected by a bucket detector (D_1). D_2 and the object are placed in the same distance away from the speckle source.

2.3.4 Experimental demonstrations

Prediction of ghost imaging using thermal light was first demonstrated in experiments by both Valencia *et. al.* in [3] and Ferri *et. al.* in [4] independently. A schematic illustration of the experiment setup can be seen in Figure 2.8. In both of the experiments, the speckles are generated by passing a laser through a slowly rotating ground glass. Speckles are then split by a non-polarised beamsplitter into the object and reference beams. An imaging lens or lens system is insert in the reference beam. To get a correlation image, the object and reference detector are arranged in the conjugate planes of this lens (or the lens system). That is, if we regard the light source plane as a mirror and unfold the system according to Kryshko's advanced wave picture, the reference detector is in the image plane of the object with respect to the lens (or lens system). If a light source illuminates from the bucket detector, a clear image of the object can be seen in the reference detector plane. This setup assures that the speckle patterns detected by the reference detector are the same as those in the object plane. Therefore a correlation image can be derived from the correlation between the speckles and the bucket signals.

Details of the speckle statistics was also discussed in [4]. In the experiment, the ground glass rotates slowly enough to give a long coherent time of the speckle ($0.5s$). On the other hand, the exposure time of the CCD has to be adjusted to be much shorter ($1ms$) than the coherent time of the speckles so that speckle patterns are recorded with high-contrast. Also, to make sure that any two acquired speckles are uncorrelated, the acquisition speed should be set slow.

So far it had been proved both theoretically and experimentally that classical light source can mimic all correlation imaging of entangled bi-photons in both the near and far-field. Moreover, the switch between near- field and far-field correlation can be done by only changing the reference beam, which is the same as in a quantum setup.

Classical GI of a phase object using speckles was also reported. In 2006, a classical GI on a pure phase object was proved by using pseudo-thermal speckles [36]. The experiment setup is similar as that in [23], the only difference is the entangled bi-photons is replaced by speckles. In contrast to the normal GI setup, a different system was proposed for pure phase classical GI [37]. In this proposed system, the reference beam is the same as normal GI setup, where the speckles get recorded by a CCD. The object beam, however, is replaced by a Mach-Zehnder interferometer, with the object being placed in one of the two arms. In the output of the Mach-Zehnder interferometer, there are two bucket detectors. It is suggested that the correlation between the differential signals from these two detectors and the CCD signals from the reference beam reveals phase information of the object. This new approach for classical phase GI is recently realised by Zhang *et al.* [38].

2.4 Computational ghost imaging

The ghost imaging setup proposed in 2.3 can be further simplified by using a computer programmable optical device called spatial light modulator (SLM). In thermal ghost imaging system, rather than use laser light transmitted through a rotating ground glass as the source, we transmit a continuous wave (cw) laser beam through a SLM whose inputs are chosen to create the desired coherence behaviour. The light modulated is

then sent to illuminate the object and then collected by a bucket detector. Knowing the deterministic modulation applied to the cw laser beam allows us to use diffraction theory to compute the intensity pattern that would have illuminated the pinhole detector in the usual lensless ghost imaging configuration.

2.4.1 Theoretical background

In 2008, a new GI experiment system called computational GI was proposed by Shapiro [5]. It was derived from a Gaussian state theory of GI developed under classical electromagnetism and semiclassical photo detection theory in [39]. In the proposed system, a spatial light modulator (SLM) was used as the phase diffuser to generate random speckles. An object was at a distance of L away from the SLM window, after which a bucket detector was located to collect object light. Different from a conventional pseudo-thermal GI where a CCD camera is normally employed to get the spatial information of the speckles, the speckle patterns in computational GI was derived from some computational method. Under a Gaussian-Schell model of pseudo-thermal light, the intensity distribution of the speckles generated by illuminating a phase diffuser by a laser was characterised by its phase-insensitive correlation function. Using standard coherence propagation function [40], the correlation function at any distance after the SLM plane can be calculated, given that the original field distribution is known. Since an SLM is driven by a computer hologram, the rendering phase distribution and hence the complex field distribution could be predicted by the hologram. Once the speckles on the object plane were worked out, they were correlated with the corresponding signals to derive the spatial information of the object.

2.4.2 Experimental demonstrations

In 2009 an experimental demonstration of computational GI was reported in [41]. In this experiment a two-dimensional phase-only liquid crystal on silicon SLM was employed. The computer-controlled SLM was illuminated by a cw laser with a Gaussian intensity distribution to generate speckles. Suppose the incident light field was E_0 with a uniform phase distribution. After the SLM, a pseudo-thermal phase distribution $\phi_r(x, y)$ was

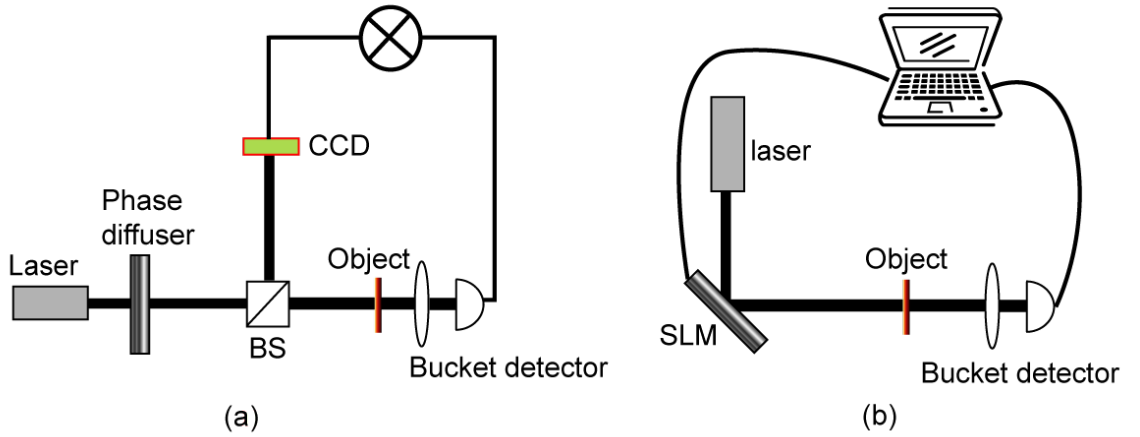


FIGURE 2.9: Comparison of (a) a conventional pseudo-thermal GI and (b) a computational GI setup. In computational GI, speckles are generated by a spatial light modulator and predicted by the controlling hologram. The reference beam together with the beamsplitter is removed from a conventional GI setup.

applied on the incident beam, so the out coming beam at the SLM plane was $E_r(x, y, z = 0) = E_r e^{i\phi_r(x,y)}$. The modulated light field was sent to the object and then collected by a bucket detector. Knowing the deterministic phase mask employed to the laser beam and the distance between the SLM and the object, the speckle patterns can be obtained [5, 40]. An image was derived from the correlation between the object signals and the calculated field patterns. It should be noticed that the image reconstruction can be conducted in any distance from the source, from the near-field to far-field, as long as the speckle distribution can be calculated. In [41], the object is placed in the far-field of the SLM. In Chapter .3 a computational GI system based on the near-field correlation which is built up in our lab is discussed.

2.4.3 Computational GI and single-pixel camera: comparison between structured illumination and coded apertures

GI in a computational apparatus is closely comparable to single-pixel camera [42], with the latter being a well studied area in computer science. In a single-pixel camera system, the object is illuminated under ambient light and imaged onto a SLM (normally a digital micro-mirror device (DMD)). The SLM is then controlled by hologram to code the image with a series of different patterns, the coded light intensities are detected by a

single-pixel detector. Correlation between the coded patterns and their corresponding intensities yields an image of the object. Single pixel camera was developed with the assistance of compressive sensing [43–47]. In a traditional camera system, in order to obtain an image with N pixels, the same number of sensors have to be employed. In a time sequential measurement with a single-pixel sensor (scanning), it has to be sampled N times (pixel number) to acquire a “perfect” image. This number of samples can be reduced by using compressive sensing based on the fact that natural images are “sparse”. More specifically, it is in the frequency domain rather than in a space domain where images are sparse and therefore easier to be compressed. Further, information of natural images mostly constrains in low frequency rather than high frequency. According to compressive sensing, therefore, an image can be reconstructed by cutting off some high frequency component but without losing much information. Based on this theorem, in a single pixel camera, an image can be obtained by sampling less than the pixel number. It is also realised that the best way to encode the image in the SLM plane is to employ totally random patterns. Consequentially, in a single pixel camera, a series of 2D random patterns and their corresponding object intensities are used in a compressive sensing algorithm to recover an image.

Both single pixel camera and computational GI use SLM and single-pixel detectors for measurement, and a recovery algorithm to retrieve images. Yet there are several different aspects of the two systems. In computational GI, a liquid crystal SLM is normally employed to generate structured illumination, which in most cases are greyscale pseudo-thermal speckles. A single-pixel camera, however, uses ambient light as light source, a DMD is put in the image plane of an imaging system and before the detection, to encode the image with binary coded apertures. Actually, in Chapter 4 our computational imaging system utilises a DMD to generate structured illumination. This brings the two systems (computational imaging and single-pixel camera) more comparable, the only difference being that DMD is used to generate structured illumination in computational (GI) imaging but used as coded apertures in single-pixel camera.

2.5 Ghost diffraction

Ghost diffraction [4, 29, 48, 49] is a similar phenomenon to GI, which can also be derived from correlation measurements between two light fields. In a GI setup with two fields, the object and the CCD camera should be placed in planes where the two light beams have strong intensity correlation, so that the intensity distribution obtained from the CCD coincide with that in the object plane. Differently, if the reference detector is located in the far-field with respect to the object plane, a diffraction pattern can be obtained from the same correlation measurement. This is called ghost diffraction.

Same as GI, the first ghost diffraction experiment was also reported using entangled photon pairs from SPDC. In the reference beam, the reference detector is placed to capture intensities that is equivalent to the far-field distribution of the intensity in the object plane. In the object beam, the bucket detector is replaced by a pinhole detector. Again, if the system is unfolded from the crystal plane according to Klyshko's advanced wave picture, this two-photon correlation diffraction can be simply explained via ray optics. Quantum ghost diffraction is achievable because entangled photons have strong correlation both in near and far-field. Therefore Gatti *et. al.* suggest that both quantum GI and quantum ghost diffraction can be achieved by changing the reference beam while keeping the object beam untouched, and this feature of quantum entanglement correlation can not be mimicked by classical light. However, a performance of both GI and ghost diffraction with pseudo-thermal light in the same system with the object beam unchanged was realised in the same group [4]. Even before that, a ghost diffraction patterns was also reported by using laser beams with classical correlated angles, by adding an imaging lens in the reference beam in Fig. 2.6.

So far all the quantum correlation effects from two-beams are achieved by classical light with only difference being that quantum correlation provides patterns with higher contrast. Therefore it is reasonable to believe that two-beam correlation is not an intrinsic quantum phenomenon. Any light source that contains spatial correlation in near and far-field can be used to generate ghost image and ghost diffraction. Entangled

photon pairs generate from SPDC contains spatial correlation in both near and far-field which guarantees quantum GI and quantum ghost diffraction, but entanglement consequentially non-locality is not necessary for this phenomenon.

2.6 Conclusion

In this chapter we have discussed the development and physics principle of GI. The development of GI experienced different modality, from quantum to classical to computational. The original idea of GI was predicted and demonstrated with quantum entanglement. It was subsequently demonstrated, however, this spatial correlation measurement is not necessary quantum induced. Generally, all GI experiments in different setup can be regarded as an phenomenon of second-order correlation between two correlated beams. As long as two beams are generated with spatial correlation, they are able to conduct GI experiments. The employment of SLM renders a GI system to a single beam correlation setup.

More GI work has been conducted beyond the discussed above. In addition to the near and far-field correlation, GI in Fourier plane were also discussed [50, 51]. Multiple wavelength GI was studied in [52, 53], and a full colour computational correlation imaging system was reported in [54]. GI using homodyne detection was reported in [55, 56]. Effect of the single-pixel detector's aperture on GI and ghost diffraction was discussed in [57, 58]. GI with true thermal light was reported in [59]. Fluorescence GI using speckles was reported in [60]. Resolution of quantum GI was discussed in [61]. An optical encryption based on computational GI was proposed in [62]. As a potential application, GI through turbulence is also studied in [63–65].

The remainder of this thesis is devoted to my research which focussed on classical and computational implementations of GI. The developments made, allow single-pixel detectors to be used more effectively in application to yield high-quality images, and may have considerable importance to a wide range of disciplines underpinned by imaging technologies.

Chapter 3

Normalised Ghost Imaging

In classical GI using pseudo-thermal speckles as a light source [2–4, 28, 66], a series of random light patterns illuminate an object. The light backscattered from the object is collected by a single-pixel, non-imaging detector. Here, this detector will be referred to as a “bucket detector”, the signal from which is referred to as the “bucket signal”. The bucket signal is an indication of how well each of the random patterns overlap with the object. A pattern that looks more like the object will result in more back-scattered light and hence a larger bucket signal, while a pattern that looks less like the object will give a lower signal. To obtain spatial information about the object, we have to combine our knowledge of the patterns and their corresponding bucket signals in a correlation function. At one pixel, this contains both the correlation between the pixel and its corresponding pixel intensities and that between un-correlated pixel intensities. While the correlation from correlated pixels contributes as signals in the image reconstruction, the correlation between un-correlated pixels renders noise [67]. This means pseudo-thermal GI contains intrinsic noise, therefore an efficient algorithm must be employed to suppress the background noise and give a high signal-to-noise ratio (SNR) for the image reconstruction.

A traditional GI algorithm (TGI) increases the SNR by using background subtraction. In addition to this method, other algorithms, called higher-order GI [68–74] and time-correspondence GI [75, 76], have been developed. In this chapter an algorithm called

“normalised ghost imaging” (NGI) developed during my research at Glasgow shall be discussed.

In essence, we have modified the weighting factor used in the TGI algorithm, to account for changes in the incited light intensity, unrelated to the intensity variations resulting from changing random patterns. It is shown that when appropriately normalised, a traditional ghost imaging algorithm can match the performance of a differential GI (DGI) approach, another common algorithm and approach yielding super results compared to TGI. We compare our NGI algorithm with these two other algorithms by analysing the SNR characteristics theoretically and furthermore validate this with experimental results. The system is based upon a computational GI system, which utilises a spatial light modulator to generate known random light patterns to illuminate a partially-transmissive object, and two detectors, one in the object path and one in the reference path. Towards the end of the chapter I shall discuss the application of the NGI method when adopting compressive techniques.

Much of the work in the chapter has been published [77]. My main contributions to this paper are as follows. I built up the computational GI setup and conducted the experiment. I realised the relation between TGI and DGI, and demonstrated it both in mathematical derivation and in the experiment. I also took the data for compressive calculation.

3.1 Introduction to existing iterative algorithms

In all approaches to pseudo-thermal ghost imaging (GI), an algorithm is employed to recover spatial information about the object using a series of measurements from the bucket detector, and random patterns which are either separately recorded or computationally predicted. The algorithms employed fall into two categories: iterative ones that give a refined estimate of the object after every new light pattern, and inversion ones which infer an object based on the entire series of patterns and measurements. In this next section two well-known iterative algorithms called traditional GI (TGI), differential GI (DGI) are discussed.

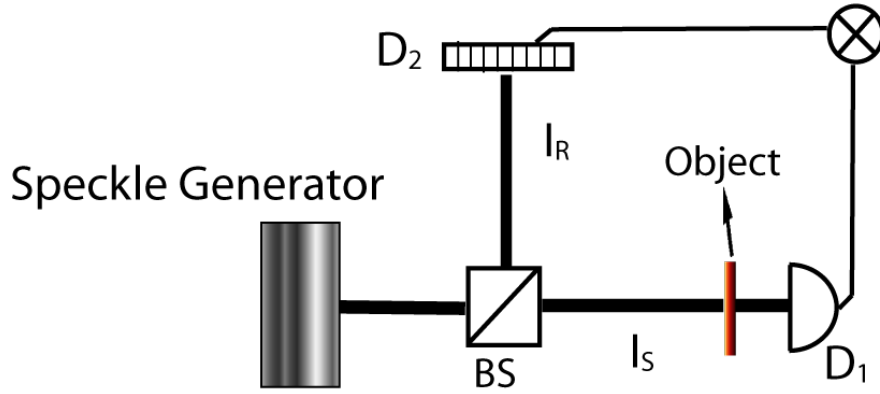


FIGURE 3.1: Illustration of thermal GI. Speckles pass through a beamsplitter (BS) and are separated into two identical beams. The object (signal) beam (I_S) illuminates the object and is collected by a bucket detector (D_1). The reference beam (I_R) is recorded by a CCD (D_2).

3.1.1 Traditional ghost imaging algorithm

Iterative GI algorithms use calculation of the correlation between every new measured bucket signals and their corresponding light patterns to retrieve the estimation of the object. Correlation between a bucket signal and its light patterns can be expressed as the second order correlation of the two beams. Consider a pseudo-thermal GI system illustrated in Fig. 3.1. The object (signal) beam and reference beam are defined as $I_S(\mathbf{x}_S)$ and $I_R(\mathbf{x}_R)$, respectively. According to Eq. 2.19 and Eq. ??, the correlation between the two beams can be expressed as

$$\langle I_S(\mathbf{x}_S) I_R(\mathbf{x}_R) \rangle = \langle I_S(\mathbf{x}_S) \rangle \langle I_R(\mathbf{x}_R) \rangle + \langle \Delta I_S(\mathbf{x}_S) \Delta I_R(\mathbf{x}_R) \rangle, \quad (3.1)$$

here $\Delta I(\mathbf{x}) \equiv I(\mathbf{x}) - \langle I(\mathbf{x}) \rangle$ is the intensity fluctuation of the two beams. The first term on the right hand side of this equation gives rise to a featureless background, while the second term gives the ghost image. In order to obtain an image with high contrast, the featureless background should be removed. This can be achieved by simply adding a DC filter in the correlation, and this method is called traditional ghost imaging (TGI) algorithm.

Following Eq. 3.1, a TGI algorithm can be written as

$$G(\mathbf{x}_S, \mathbf{x}_R) = \langle I_S(\mathbf{x}_S) I_R(\mathbf{x}_R) \rangle - \langle I_S(\mathbf{x}_S) \rangle \langle I_R(\mathbf{x}_R) \rangle. \quad (3.2)$$

The object here is restricted to be a two dimensional (2D) transmissive object for discussion convenience. Therefore the transmissive light power measured by the bucket detector can be expressed as

$$S = \int_{A_l} I(x_S, y_S) T(x_S, y_S) dx_S dy_S, \quad (3.3)$$

here A_l is the laser area and $T(x_S, y_S)$ is the (intensity) object transmission function.

For each iteration, i , we define the contribution to the image reconstruction to be [41]

$$G_i(x, y)_{TGI} = (S - \langle S \rangle) (I(x, y) - \langle I(x, y) \rangle), \quad (3.4)$$

here $\langle . \rangle \equiv \frac{1}{M} \Sigma$ denotes an ensemble average for M iterations. We obtain the final reconstruction by averaging over all iterations such that $G(x, y) = \langle G_i(x, y) \rangle$. Notice that in pseudo-thermal GI the signal and reference beams are separated by a 50:50 non-polarised beam splitter, in most cases we can safely assume that the two beams are identical $I(x_S, y_S) = I(x_R, y_R) = I(x, y)$ after the same propagation distance.

This TGI algorithm was first introduced in [27]. It is easy to understand the reconstruction as being derived from the weighted sum of the speckle field for each measurement. Therefore S is the weight for the speckle field for each measurement. Higher S means the light pattern looks more like the object, while lower S indicates the light patterns looks less like the object. In real experiments, however, this fluctuation of intensities can be caused by other factors, including changes in the laser (light source) power and changes in the efficiency with which the pattern is imprinted. All these sources of change become noise in GI reconstruction and render low SNR. For a transmissive object, more transmissive light intensity means higher noise. Therefore one drawback of this algorithm is that signal-to-noise (SNR) ratio is low, especially for highly transmissive object [67, 77]. Figure 3.2 shows some simulation results of two different objects. The method is shot-noise free, but simulates the fluctuation of incident light intensity and the hologram efficiency, which adds noise to the reconstruction. Fig. 3.2.(a) shows the reconstruction of a 2D binary (0s, 1s) transmissive packman, with a low transmission ratio. An image is obtained from TGI with relative high SNR after a number of iterations equal to the

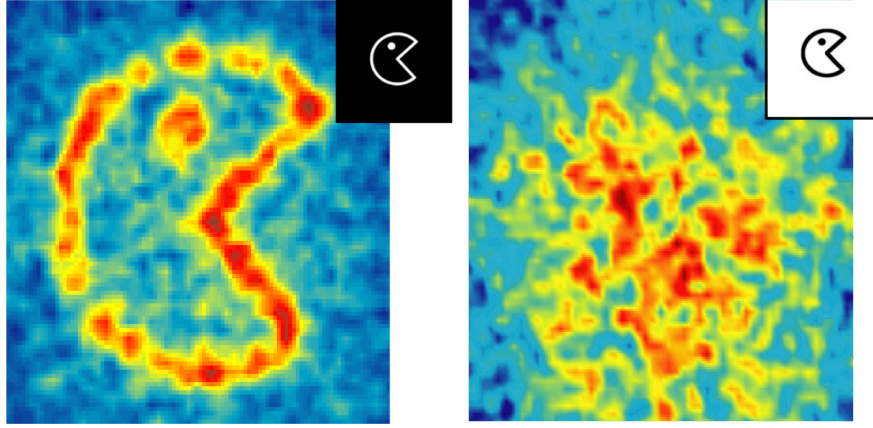


FIGURE 3.2: Simulation TGI reconstruction of a 2D binary transmissive *Packman* and its $(1s, 0s)$ inverse. Both results are obtained after a number of iterations equal to their pixel number. The packman on the right has more 0s in its area so it is more blocked, while its inverse on the right is more transmissive.

pixel number of the object. But the same reconstruction process fails to generate an image for the $(1s, 0s)$ inverse object which is in a higher transmission ratio. It shows that TGI for objects with high transmission suffers very low SNR. And this comparison is also proved in experiment as we are going to show later.

3.1.2 Differential ghost imaging algorithm

To overcome the low SNR of TGI, another algorithm was proposed by Ferri *et al* as differential ghost imaging (DGI) [67]. It utilizes a second bucket signal in the reference beam which is used to weight the speckle field based on the average transmission signal relative to the average reference signal. Similar to the bucket signal S in the object beam, the total reference light intensity can be expressed as

$$R = \int I(x_R, y_R) dx_R dy_R. \quad (3.5)$$

In a conventional GI setup, R can be obtained by summing up all of the pixel values on the CCD camera. While in computational GI, this can be obtained from a photodiode collecting all the reference photons.

The idea of DGI is to utilise a new differential signal rather than $\Delta S = S - \langle S \rangle$ as the weighting factor. Using two intensity signals S and R , the new differential signal is defined as

$$\Delta S_d = S - \frac{\langle S \rangle}{\langle R \rangle} R, \quad (3.6)$$

and the according iterative contribution of DGI can be expressed as

$$G_i(x, y)_{DGI} = \left(S - \frac{\langle S \rangle}{\langle R \rangle} R \right) (I(x, y) - \langle I(x, y) \rangle). \quad (3.7)$$

We observe the second term in brackets on the right hand side of Eq. 3.4 and Eq. 3.7 are identical, however, the first term in brackets of Eq. 3.7 is now weighted according to the average value of S , which is normalized to the average value of R . As demonstrated in [67] the DGI algorithm improves by order of magnitude the SNR of the measurement with respect to TGI. Moreover, a key difference from TGI, it is no longer sensitive to other sources of noise. For example, fluctuations in the laser power or changes to the SLM efficiency will affect both the reference signal and the transmitted signal, which is cancelled out in the weighting factor of ΔS_d , and thus the contribution to the reconstruction will be weighted more appropriately. Experimental and simulation results will be presented in later section to show the advantage of DGI compared to TGI.

3.2 Normalized ghost imaging

In this section we discuss an algorithm called normalised ghost imaging (NGI) that we proposed in our lab [77]. As mentioned before, key to all GI algorithms is that the changes in the measured signal should arise only from the overlap of the known random pattern with the unknown object. Obviously, other sources of signal change are possible, including fluctuations of the source intensity and changes in the efficiency of the phase diffuser. All these sources of change become noise in GI reconstruction and render low

SNR. Therefore the original motivation to propose NGI is to get rid of any unwanted fluctuation of the source intensity. To achieve this, a straightforward method is to use the relative fluctuation S/R rather than the change of absolute intensity S as the weighting factor. The algorithm used to describe each contribution to the reconstruction in NGI is given by

$$G_i(x, y)_{NGI} = \left(\frac{S}{R} - \left\langle \frac{S}{R} \right\rangle \right) (I(x, y) - \langle I(x, y) \rangle) . \quad (3.8)$$

By using a relative light intensity as weighting factor, effect from the light source fluctuation is removed. Besides this, NGI gives a much better SNR than TGI, especially for more transmissive object. Details will be covered later in the experiment discussion.

Moreover, it is noticed that NGI and DGI produce “almost the same” results, which indicates their equivalence to each other. The equivalence are then first proved mathematically. By assuming $\langle \frac{S}{R} \rangle \approx \frac{\langle S \rangle}{\langle R \rangle}$ for a large number of measurements, and comparing Eq. 3.7 and 3.8, we can get the iterative and total relation between NGI and DGI as

$$G_i(x, y)_{NGI} = \frac{1}{R} G(x, y)_{DGI} , \quad (3.9a)$$

$$\langle G(x, y)_{NGI} \rangle = \frac{1}{\langle R \rangle} \langle G(x, y)_{DGI} \rangle . \quad (3.9b)$$

To arrive at Eq. 3.9b from Eq. 3.9a we assume $G(x, y)$ and R are independent.

Equation 3.9 shows the amplitude of NGI and DGI reconstruction are only different by a constant scaling factor $\frac{1}{\langle R \rangle}$, which does not render any SNR difference, which is a first proof of the equivalence between NGI and DGI. Exactly, Eq. 3.9 shows DGI and NGI are equivalent in their signals. To quantitatively analysis the relation between these different algorithms, we need to analyse their SNR.

3.3 Signal-to-noise ratio analysis

SNR is an important method to analyse GI reconstruction [78–82]. To make a quantitative comparison between NGI and the other two existing algorithms, we analyse their SNR in this section. Here we adopt a similar definition of SNR as used in [67].

When the coherent size of speckles is much smaller compared to the feature size of the object (perfect resolution), the average quantity of GI reconstruction of $T(x, y)$ can be expressed as

$$\langle G(x, y) \rangle = A_s \langle I(x, y) \rangle^2 T(x, y), \quad (3.10)$$

here A_s is the average coherent length of speckles. According to Ferri *et al* [67], the corresponding signal can be defined as

$$(\Delta \langle G(x, y) \rangle)^2 = A_s^2 \langle I(x, y) \rangle^4 (\Delta T)^2, \quad (3.11)$$

where ΔT is the variation of the object transmission function to be detected. In our discussion, the object is restricted to binary, so $\Delta T = 1$. On the other hand, the noise associated to the measurement of $O(x, y)$ is the variance of the reconstruction amplitude which can be expressed as

$$\langle \delta G^2(x, y) \rangle = \langle G(x, y)^2 \rangle - \langle G(x, y) \rangle^2. \quad (3.12)$$

As we can see from Eq. 3.4, Eq. 3.7 and Eq. 3.8, GI with background subtraction always have a zero-mean average $\langle G(x, y) \rangle = 0$, thus the second term on the right hand side (RHS) of in Eq. 3.13 may be omitted. For TGI, under the assumptions of uniform illumination (the average speckle beams are constant over their area) and perfect resolution, variance in the reconstruction can be expressed as

$$\langle \delta G_{TGI}^2 \rangle = A_s^2 A_l^2 \langle I \rangle^4 \overline{T^2}, \quad (3.13)$$

here $\overline{T^2} = \int_{A_l} \langle I(x, y) \rangle \cdot T^2(x, y) dx dy / \int_{A_l} \langle I(x, y) \rangle dx dy$ is the average quadratic transmission function of the object. A_l is the area of the whole speckle beam. Therefore by combining Eq. 3.4, Eq. 3.10 and Eq. 3.13, we summarise the iterative signal, noise and SNR as

$$(\Delta \langle G_{TGI} \rangle)^2 = A_s^2 \langle I \rangle^4 (\Delta T)^2, \quad (3.14a)$$

$$\langle \delta G_{TGI}^2 \rangle = A_s^2 A_l^2 \langle I \rangle^4 \overline{T^2}, \quad (3.14b)$$

$$SNR_{TGI} = \frac{1}{N_s} \frac{\Delta T^2}{\overline{T^2}}. \quad (3.14c)$$

here $N_s = A_l/A_s$ is the number of speckles in the light field.

DGI retrieves the fluctuation of T , that is $\delta T(x, y) = T(x, y) - \bar{T}$, rather than T itself.

Similarly, we can express the signal, noise, and SNR of DGI as

$$(\Delta \langle G_{DGI} \rangle)^2 = A_s^2 \langle I \rangle^4 (\Delta T)^2, \quad (3.15a)$$

$$\langle \delta G^2(x, y)_{DGI} \rangle = A_s^2 \langle I \rangle^4 \delta T(x, y), \quad (3.15b)$$

$$SNR_{DGI} = SNR_{DGI} = \frac{1}{N_s} \frac{\Delta T^2}{\overline{\delta T^2}}. \quad (3.15c)$$

where $\overline{\delta T^2} = \overline{T^2} - \bar{T}^2$ and $\overline{T^2} = \int_{A_l} \langle I(x, y) \rangle T^2(x, y) dx dy / \int_{A_l} \langle I(x, y) \rangle dx dy$.

Now we calculate SNR of NGI. The calculation of SNR_{NGI} through the same method above is not straight forward. A simple way to achieve it is to use the relation between NGI and DGI, which is shown in Eq. 3.9. By combining Eq. 3.9b and Eq. 3.15a, we can express the signal of NGI as

$$(\Delta \langle O_{NGI} \rangle)^2 = A_s^2 \frac{\langle I \rangle^4}{\langle R \rangle^2} (\Delta T)^2. \quad (3.16)$$

Using linearization we can write

$$\frac{S}{R} \approx \frac{\langle S \rangle}{\langle R \rangle} \left(1 + \frac{\delta S}{\langle S \rangle} - \frac{\delta R}{\langle R \rangle} \right), \quad (3.17)$$

where δS and δR are the zero-mean deviation of S and R . Using Eq. 3.17 we rewrite noise of NGI and DGI as

$$\langle \delta G^2(x, y)_{DGI} \rangle = \langle S \rangle^2 \left\langle \left(\frac{\langle \delta S \rangle}{\langle S \rangle} - \frac{\langle \delta R \rangle}{\langle R \rangle} \right)^2 (I(x, y) - \langle I(x, y) \rangle)^2 \right\rangle, \quad (3.18a)$$

$$\langle \delta G^2(x, y)_{NGI} \rangle = \frac{\langle S \rangle^2}{\langle R \rangle^2} \left\langle \left(\frac{\langle \delta S \rangle}{\langle S \rangle} - \frac{\langle \delta R \rangle}{\langle R \rangle} \right)^2 (I(x, y) - \langle I(x, y) \rangle)^2 \right\rangle. \quad (3.18b)$$

Thus the noise of NGI can be obtained by exploiting the comparison of Eq. 3.18a and Eq. 3.18b and using Eq. 3.15b

$$\langle O_{NGI}^2 \rangle \approx A_s A_l \frac{\langle I \rangle^4}{\langle R \rangle^2} \overline{\delta T^2}. \quad (3.19)$$

Finally, we arrive at the iterative SNR contribution for NGI is

$$SNR_{NGIi} = \frac{1}{N_s} \frac{\Delta T^2}{\overline{\delta T^2}}. \quad (3.20)$$

Again, $N_s = A_l/A_s$ is the number of speckles in the field. By taking into account that the total SNR of GI is proportional to both the iterative SNR and the iteration M we get the final SNR for NGI and DGI after M measurements as

$$SNR_{NGI} = SNR_{DGI} = \frac{M}{N_s} \frac{\Delta T^2}{\overline{\delta T^2}}, \quad (3.21)$$

The SNR contribution for NGI is found to be identical to that of the DGI algorithm derived in [67]. Comparing Eq. 3.21 and Eq. 3.14c, we can examine the difference between the NGI (or DGI) and TGI algorithms by obtaining the ratio of SNR calculations, given as

$$\frac{SNR_{NGI}}{SNR_{TGI}} = 1 + \frac{\overline{T}^2}{\overline{T^2} - \overline{T}^2}. \quad (3.22)$$

As highlighted by Ferri *et al*, the difference is always greater than 1 and dependent only upon the variation in the object transmission function.

In this section we have mathematically analyse the SNR for NGI compared with TGI and DGI. Mathematical derivation shows that NGI performs as well as DGI in terms of GI reconstruction. And they are both better in improving the SNR of GI, especially for more transmissive object. In the following sections we are going to demonstrate these conclusion in our computational GI system.

3.4 Experimental setup

In this section we introduce a computational GI setup built up in our lab. Compared to conventional GI setup, computational GI setup only consists one beam: the object beam. The reference beam and therefore the CCD camera are removed from the system, rendering GI a real single-pixel imaging system. We test all the three iterative algorithms with experiment results obtained from our computational GI system.

3.4.1 General description

The experimental setup is shown in Fig. 3.3. Here a random light pattern is generated from a simulated superposition of plane waves using random numbers, which is then sent to a liquid crystal spatial light modulator (LC-SLM) (Boulder Nonlinear Systems) to produce a synthesized speckle field. The SLM has 512×512 pixels in the window of size 7.68×7.68 mm. We pass a collimated laser of wavelength $\lambda = 632.8$ nm through a polarizing beam splitter and a half-wave plate, before illuminating the SLM window. The speckle field is generated by modulation of the SLM and the returning light field is then magnified by a simple telescope system consisting of 150 mm and 450 mm biconvex lenses. The object is located at the focus plane of the 450 mm lens, which is also the image plane of the SLM window. A 50 : 50 beam splitter is placed before the object in order to split the speckle field into two beams; the object beam ($I(x_S, y_S)$) and the reference beam ($I(x_R, y_R)$). The object beam illuminates the object and is then collected by a bucket detector, thus providing an computational GI setup. The additional reference beam for monitoring the light differentiates our system from previous experimental computational GI configurations. Since we are generating a computer hologram that is then sent to the SLM to create the speckle field, we can therefore predict the light field at the reference arm, negating the demand for a CCD camera, and requiring only a second bucket detector. It should be noted that for TGI based on our computational GI setup, only the object bucket detector is needed. The additional bucket detector in the reference arm is only required for NGI and DGI. Light intensities detected by the object and reference bucket detectors are indicated by S and R respectively, and the speckle field is described by $I(x, y)$. As we use a 50 : 50 beam splitter, it is understood that $I(x, y) = 2I(x_S, y_S) = 2I(x_R, y_R)$.

3.4.2 Spatial light modulator and modulated speckles

A SLM is a transmissive or reflective optical device that is employed to modulate the spatial amplitude and (or) phase of a light field. In our experiment, we use an electro-optical driven SLM containing liquid crystals as the modulation material. The optical properties of the liquid crystals are modified by means of an electric field, which is one of

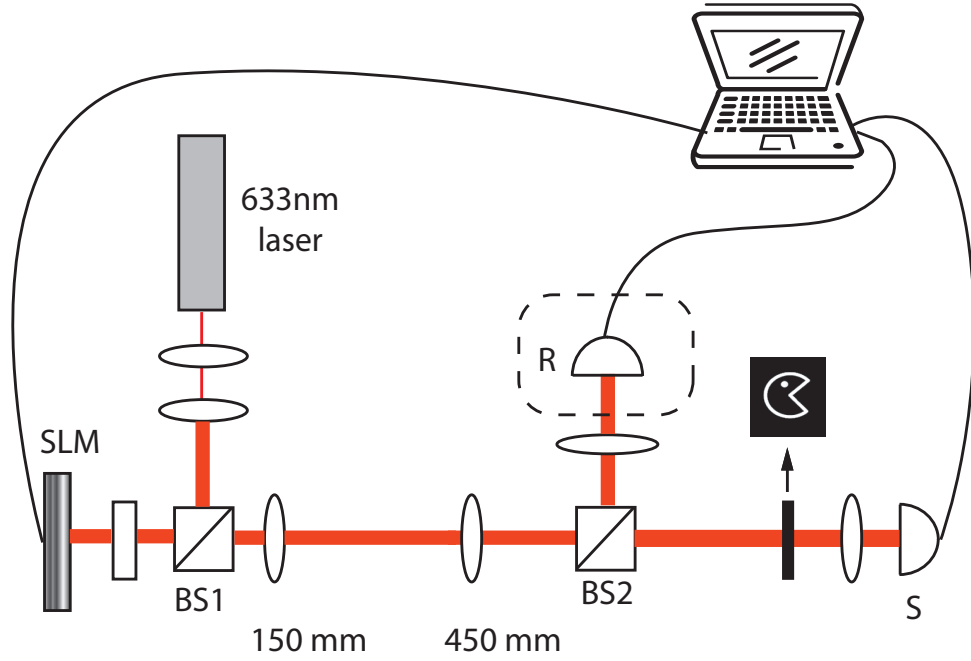


FIGURE 3.3: Computational ghost imaging setup used in the experiment. A spatial light modulator (SLM) is used to generate a random speckle field. A beam splitter (BS) is used to measure a reference signal R on a bucket detector before the object. The signal, S , is measured on a bucket detector which collects the light transmitted after the object.

the most commonly used modulation mechanisms in liquid crystal SLM. An important property of liquid crystals is that they are birefringent, which means they have different refraction indices associated with different crystallographic directions. In an electro-optical SLM, the voltage induced on each pixel produces an electric field to render a change of the properties of the liquid crystal, and therefore changes the polarisation of the incident light fields. To modulate the amplitude of the field, a system shown as Fig. 3.4 is required. In the system a polarised beam is reflected by a polarised beam splitter (PBS) toward the SLM window. A half-wave plate rotates the light into the frame of the optical axis of the SLM. Light is modulated by the SLM depending on the voltage of the reflecting pixel and then re-rotated by the half-wave plate. After the PBS a intensity distribution depending on the hologram on the SLM is achieved. For the SLM we use in our system, each pixel has a modulation dimension from 0 to 255, which corresponds to a polarisation change from 0 to 180° .

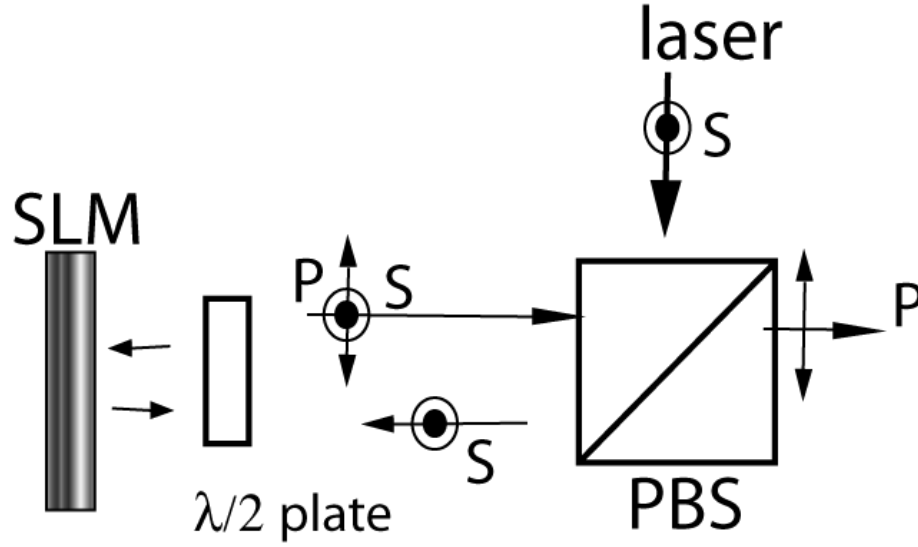


FIGURE 3.4: Illustration of a intensity spatial light modulator setup. Linear polarised laser passes through a half-wave plate and is modulated by the SLM, gets through the half-wave plate again. The transmissive light from the polarised beamsplitter (PBS) contains spatial information determined by the hologram.

Based on the speckle generator we introduced above, we generated a series of random speckle patterns by controlling the SLM with random generated holograms. The holograms are calculated by simulating the interference of many plane waves, to make sure that hologram-controlled speckles the real and imaginary amplitude components and the wave vector \mathbf{k} of each simulated plane wave is Gaussian distributed. Fig. 3.5 shows a typical example of the speckle patterns generated on the SLM and the exponentially distributed intensity for many patterns, implying that the speckle hologram has complex-Gaussian statistics, thereby a good approximation for real speckle fields [83].

3.5 Experiment results

3.5.1 Experimental comparison between different algorithms

A binary transmissive object, $5\text{mm} \times 5\text{mm}$ in size, is located after a 3 times magnification telescope in the image plane of the SLM. Since we know both the object and the random

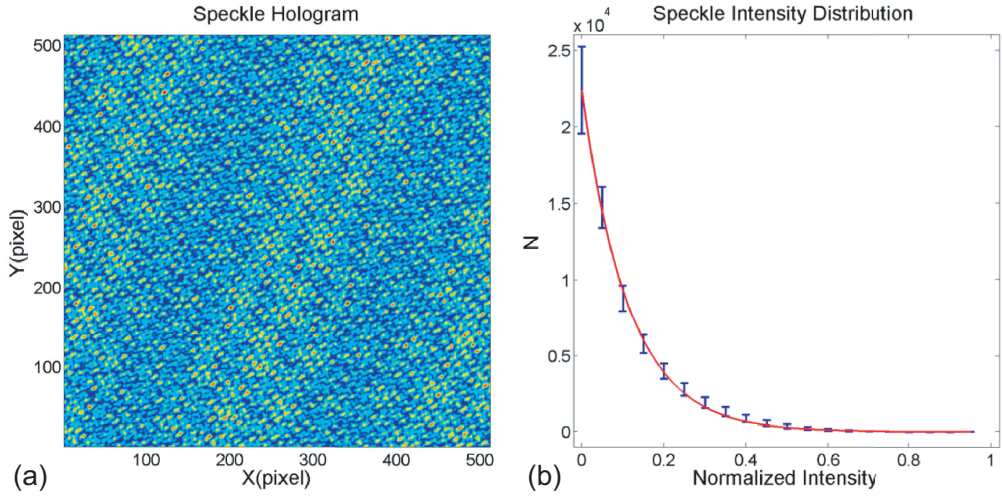


FIGURE 3.5: (a) A typical speckle pattern hologram. (b) The measured intensity distribution of the speckle pattern (blue) and an exponential curve (red).

speckle field projected to the SLM, we are able to simulate the expected results for comparison with our experiment. Experimental and simulated reconstruction results after 10000 iterations are shown in Fig. 3.6. The simulated reconstruction is produced assuming no external noise sources. The partially transmissive object used is indicated in the bottom right of Fig. 3.6. It is clear that the DGI and NGI algorithms provide very similar results, as predicted from the theory, and both show improved background subtraction compared to TGI.

Compared with the traditional computational GI setup, NGI algorithm requires a reference bucket detector. However, as discussed before, the advantage of computational GI means that we can replace this bucket detector with a virtual reference detector generating a simulated R . Thus we can negate the requirement for the reference detector and return the system to a true single element camera, which we call single-detector NGI (SNGI). The two major factors that dominate the value of R are from the different speckle patterns displayed on the SLM and fluctuations of the incident laser power. We can computationally predict changes to the value of R due to the speckle pattern, whereas fluctuations of the laser power can be simulated by using a rolling average for a particular series of S measurements. The bottom row in Fig. 3.6 shows the experimental results for reconstructing the object using the SNGI algorithm. We observe similar results compared with DGI and NGI algorithms indicating an improved performance

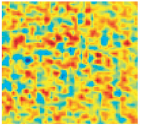
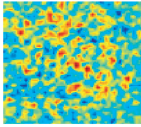
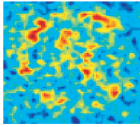
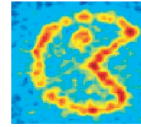
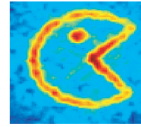
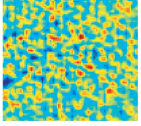
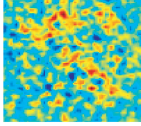
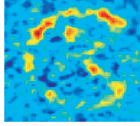
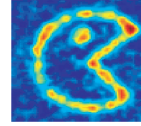
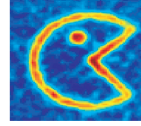
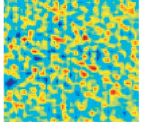
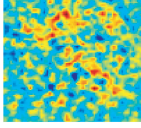
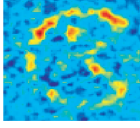
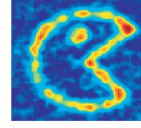
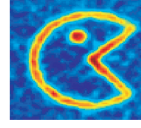
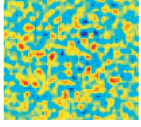
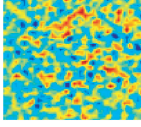
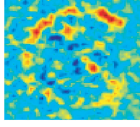
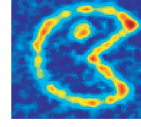

algorithm	experiment				simulation
TGI					
DGI					
NGI					
SNGI					
iterations	10	100	1000	10000	object

FIGURE 3.6: Experimental results (middle column) for TGI, DGI and NGI reconstruction algorithms as they evolve (10, 100, 1000 and 10000 iterations from left to right, respectively) with the corresponding simulated results (right column). The transmissive object is shown in the lower right. The bottom row shows the evolution for reconstructing the object with the NGI algorithm using a single detector and predicting the reference signal R , termed here the SNGI algorithm.

compared with the TGI algorithm for single element camera.

3.5.2 Experimental SNR Analysis

To demonstrate the effect of object transmission function on the performance of NGI compared with TGI and DGI algorithms we used a similar experimental approach to that in Ref. [67]. By scanning a knife edge (located in the image plane of the SLM, as before) across the speckle field in well defined steps (for which $\Delta T = 1$), we measured the SNR's for the final object reconstruction obtained after 5000 random speckle iterations. The beam size used was 10×10 mm and the speckle size at the plane of the object was found to be $\delta_s \sim 90 \mu\text{m}$, providing around $N_s \sim 12500$ speckles. The experimental results and theoretical predictions for the SNR's of each iterative algorithm are shown in Fig. 3.8. Note that the y -axis has been normalized to the number of iterations. We observe close quantitative agreement between the theory and the measurements. The results indicate that for low transmissive objects, all algorithms reconstruct with

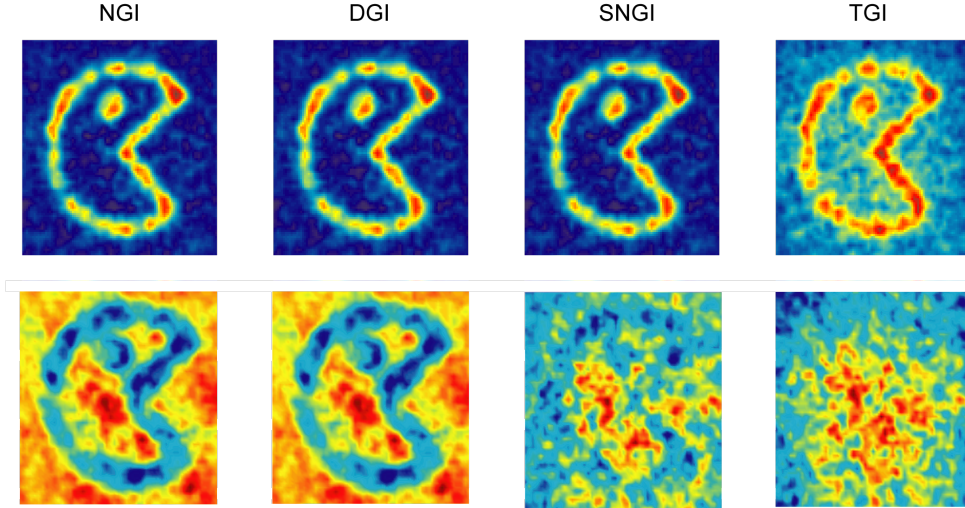


FIGURE 3.7: Experimental results of a *Packman* (top row) and *anti-Packman* (bottom row) from different GI algorithms.

similar SNR, while for more transmissive objects the DGI and NGI algorithms become more efficient in comparison to TGI due to the differential nature of the reconstruction. Furthermore, we observe that when using a single detector, SNGI is a more efficient algorithm for reconstructing objects of all transmissions compared to TGI. We observe that for increasing transmissive objects SNGI becomes less efficient than NGI, for which the reason is the subject of ongoing research. Similar to [67], we find a systematic discrepancy between the experimental results of TGI and the theoretical predictions.

3.6 Normalization in matrix inverse algorithms

3.6.1 Matrix inverse algorithms and compressive sensing

A problem of iterative algorithm is that it always requires many iterations in order to get an image with high SNR. For an object with N pixels, according to the Nyquist limit, one needs at least $M = N$ measurements in order to complete an image reconstruction. In pseudo-thermal GI, because the speckles have a lot of overlap, normally the actual

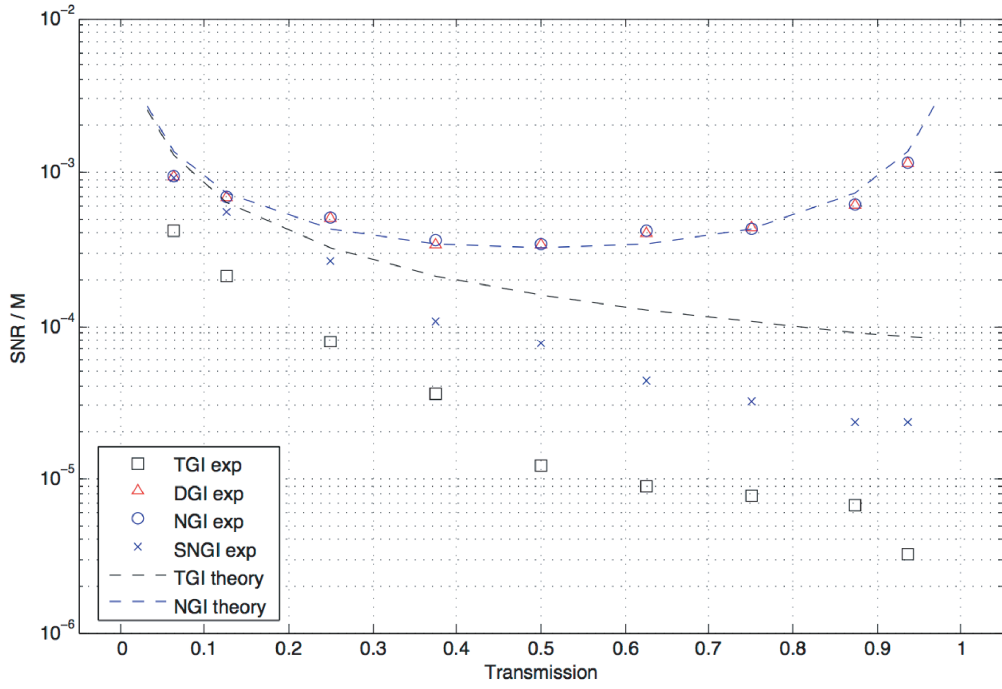


FIGURE 3.8: Signal-to-noise ratio's for DGI, NGI, SNGI and TGI versus transmitting area. Transmitting ratio is defined as the ratio between the transmitting area of the object and the area of the speckle field.

measurement step is much more than the pixel number $M \gg N$. It is very helpful if some more efficient algorithms is used to reduce measurement steps.

In an alternative way to the iterative techniques, we choose to record all the signals for a complete set of speckle patterns and then treat the image reconstruction as a problem of matrix inversion. For an object with N pixels, a series of M speckle patterns are used for reconstruction. If we represent each speckle pattern as a row vector, then the M speckle patterns can be represented by a $M \times N$ matrix. Then the vector containing the measured signals is a M element vector. And the acquisition process can be expressed as

$$\begin{bmatrix} S_i \\ \vdots \\ S_N \end{bmatrix} = \begin{bmatrix} I \end{bmatrix}_{M \times N} \times \begin{bmatrix} T_{(x,y)} \end{bmatrix}_M. \quad (3.23)$$

An image reconstruction can be achieved by solving this linear equation. To obtain a unique resolution for the linear equation indicated in Eq. 3.23, at least $M \times N$ measurements are required. And same for iterative algorithm, the overlap between speckles which reduce reconstruction efficiency also exists here. Therefore inversion algorithm

itself does not help to reduce the measurement steps for an image reconstruction. But there is a novel signal process method called compressive sensing that can be applied in inversion problem to help reduce the steps of measurement. Compressive sensing takes advantage of signal sparsity or compressibility in some domain [43–45]. Actually most of natural images are sparse, not in the spatial domain but in Fourier space. That is, if an image is transformed to its Fourier space, most of the Fourier coefficients are small, only the low frequency coefficients have large values. Based on this property, we can filter most of the values in frequency space to be zero without losing much information. Moreover, we send the rendered data to a convex optimisation program and derive an image which minimises the l_1 – norm in the Fourier plane

$$\min_G \|I \times G\|_{l_1}, \text{subject to } I \times G = S. \quad (3.24)$$

This method applies even when $M < N$. That is when the acquisition is under the Nyquist limit and therefore the system is ill-conditioned and calculating the inverse of the matrix is not straightforward. Problems of this type are wide spread in physics and techniques for solving them have been developed. Within our system the appeal is to reconstruct the image of N pixels from M measurements where $M < N$. That this is possible is based on the fact that natural images are sparse and the reconstruction can be obtained by solving a convex optimization problem [47], which is a generalization of a linear least squares problem. In contrast to iterative methods, compressive GI (CGI) needs to take all measurements, represented here, in some compressible basis (in this case a discrete cosine transform which has been applied to each row of the $M \times N$ matrix). Solving the convex optimization problem requires minimizing the ℓ_1 norm [46].

3.6.2 Normalized compressive ghost imaging

By normalizing the measured object signal relative to the reference signal as performed above, such that $S' \equiv S/R$, we can apply the CGI technique [84–88] to reconstruct our

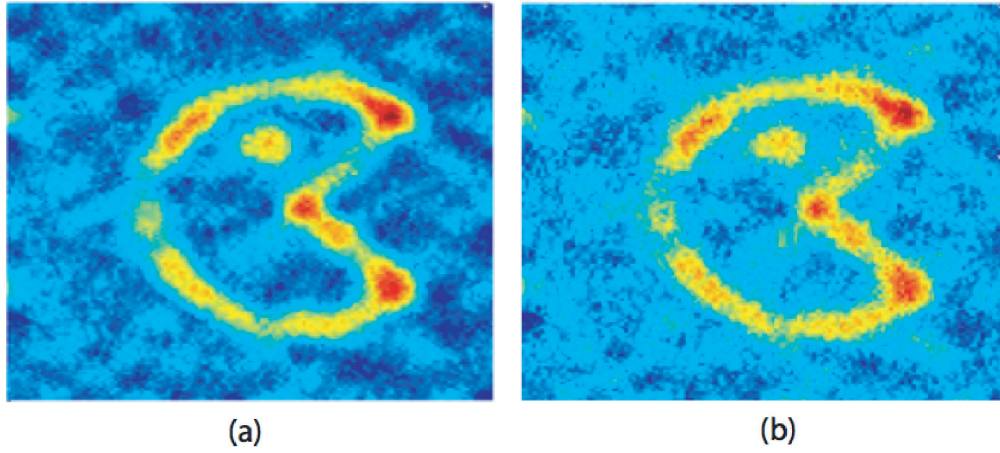


FIGURE 3.9: (a) Experimental result of Normalized known vector reconstruction method (S/R) having SNR = 9.95. (b) Standard CGI reconstruction from S having SNR = 7.39.

object. Equation 3.23 can then be written for normalized CGI (NCGI) as

$$\begin{bmatrix} S'_i \\ \vdots \\ S'_N \end{bmatrix} = \begin{bmatrix} I \end{bmatrix}_{M \times N} \times \begin{bmatrix} T_{(x,y)} \end{bmatrix}_M. \quad (3.25)$$

Performing both NCGI and CGI analyses using the same experimental data (acquired using the experimental setup in Fig.3.3) we obtain the reconstruction in Fig.3.9. We observe a clear improvement using the NCGI algorithm compared to the CGI algorithm, manifest as an increased SNR value. The efficiency with which NCGI can reconstruct sparse images over CGI is determined by the level of noise in the system. We find that when there is no system noise present, both reconstructions are essentially identical. Thus the main improvement in employing NCGI over CGI with the additional reference detector is the ability to protect the reconstruction from time varying noise sources.

3.7 Conclusion

In conclusion we have compared different iterative GI methods to reconstruct an object and studied a new GI algorithm, which we call normalized GI (NGI). The performance of the differential GI (DGI) and NGI algorithms show good quantitative agreement as

predicted by the theoretical foundations that support them. Our results indicate that by normalizing the measured signal relative to a reference signal, a more appropriate weighting factor is applied to the ensemble average of the estimated object, compared to the traditional GI (TGI) algorithm. Our analysis of the measured SNR and the object transmission shows a significant improvement for more transmissive objects in comparison to TGI. Furthermore, we have shown it is possible to apply normalization to systems with a single detector, SNGI, by estimating the reference signal. We have also investigated normalization within a compressive matrix inversion method, showing similar results to a non-normalized algorithm but with enhanced noise suppression. We believe the NGI algorithm will be a useful resource for imaging where alternative techniques are required in the future.

Chapter 4

3D Computational Imaging with Single-Pixel Detectors

In this chapter a modified computational GI system is detailed, capable of imaging large 3D objects compared to the previously studied objects that consisted primarily of small 2D binary template objects. Instead of using a liquid crystal spatial light modulator (SLM), we employed a digital micro-mirror device (DMD) to spatially modulate the light field incident on the object, and employed several single-pixel detectors located in different positions to measure the back-scattered light. The images obtained from each detector can be used in a separate algorithm to rapidly reconstruct a 3D profile of the object.

In the previously discussed GI setup a liquid crystal SLM is used to generate speckles for illumination, however for our system, a digital light projector (DLP) is utilised as the light source. The DLP contains a white light source and a DMD to generate binary (0s and 1s) structured illumination (light patterns). As the structured illumination can be predicted by the control holograms, the need for a spatially resolving detector is removed, and only single-pixel detectors are used. To distinguish our new system from a computational GI system, we call our new system a computational imaging system with single-pixel detectors. In a single-pixel computational imaging system, the object for imaging is extended from 2D transmissive objects to a three dimensional

(3D) real-life size reflective object. Using the same algorithms as used in GI, the single-pixel computational imaging system infers the scene by correlating the known spatial information of a changing incident light field with the total reflected (or transmitted) intensity. Compared to previous GI experiments, our system is able to improve the reconstruction to a much better level where 3D reflective object can be imaged with reasonable details.

In addition to 2D reconstruction, a 3D imaging system is also built up based on this technique. Rather than using only one detector in the system, four single-pixel detectors are employed in the system, each producing a 2D image. It is realised that all these images have the same shape but different intensity distribution. And the intensity distribution of an image is determined by the surface normals of the object and the detecting vector. With the knowledge of the intensity distribution in the four images together with the detecting vectors, the 3D profile of the object can be derived by employing an algorithm called “photometric stereo”.

In this chapter, we first discussed the limitation of the computational GI system introduced in Chapter 3. Furthermore, the adaptive single-pixel computational imaging system is introduced. Correlation imaging results obtained from the system will be discussed together with their shading properties. The 3D reconstruction utilising the shading property is then discussed. Most of the work in this chapter is published in [89]. My major contributions to this work was designing and conducting the experiment, improving the photometric stereo algorithm and performing the 3D reconstruction calculation.

4.1 Limitations of the existing GI experiment methodology

Original GI was first demonstrated using quantum entanglement which has sparked much debate whether or not GI is an intrinsic quantum phenomena. The nature of such experiments based on this principle therefore limited it to the use of binary transmissive

objects. However, GI has been shown to work using thermal light patterns which theoretically allow the use of multi shaded transmissive or indeed reflective objects. A prime limitation of classical GI using thermal light is that the low single-to-noise-ratio (SNR). To improve the reconstruction SNR, several advanced algorithms were developed, which are as discussed in Chapter 3. Among these algorithms, DGI and NGI work well to produce high SNR. On the other hand, the proposal of computational GI simplified the hardware of GI system and make GI experiment more applicable. In 2008, an experiment to image an reflective object was performed by Meyers *et. al.* in a GI system using chaotic light source [90, 91], but the result was limited as a 2D outline of the object. There are also other studies about GI using reflective photons, but mostly are limited to theoretical studies [65, 92–94].

Our experiment is therefore focused on to image a 3D object in a GI system. A first attempt was made in the computational GI system introduced in Chapter 3. The object (Fig. 4.1) consists two 3D letters *G* and *U*, which are 3D-printed from white plastic. Each letter is approximately $1\text{ cm} \times 0.5\text{ cm} \times 0.3\text{ cm}$. They are placed with some spatial separation in both transverse and longitude direction to contain some simple 3D information. Indeed the simplicity and dimensions of the object mean that there is a close similarity to the object appearing as if it were just 2D in this case. The GI reconstruction can be seen in Fig. 4.1. Similar as the results in [90], only an outline was obtained with little details and in a low resolution.

The relativity low SNR can be explained here in terms of the generally low reflectively of the object. In the computational GI system, speckles are generated by passing a laser beam through a spatial light modulator (SLM). The low efficiency of the speckle generator renders the modulated light fields at a low intensity, this is further exasperated since the light fields are subsequently magnified to illuminate a larger area. This issue does not majorly impact the result in the case where the collecting efficiency is high. After transmission through the object, almost all of the light can be obtained by using a collecting lens in the beam path. If the object is reflective, however, photon collection becomes difficult, since light is scattered into a large solid angle. Only a small portion of the incident light can be collected, even when a collective lens with a large numerical

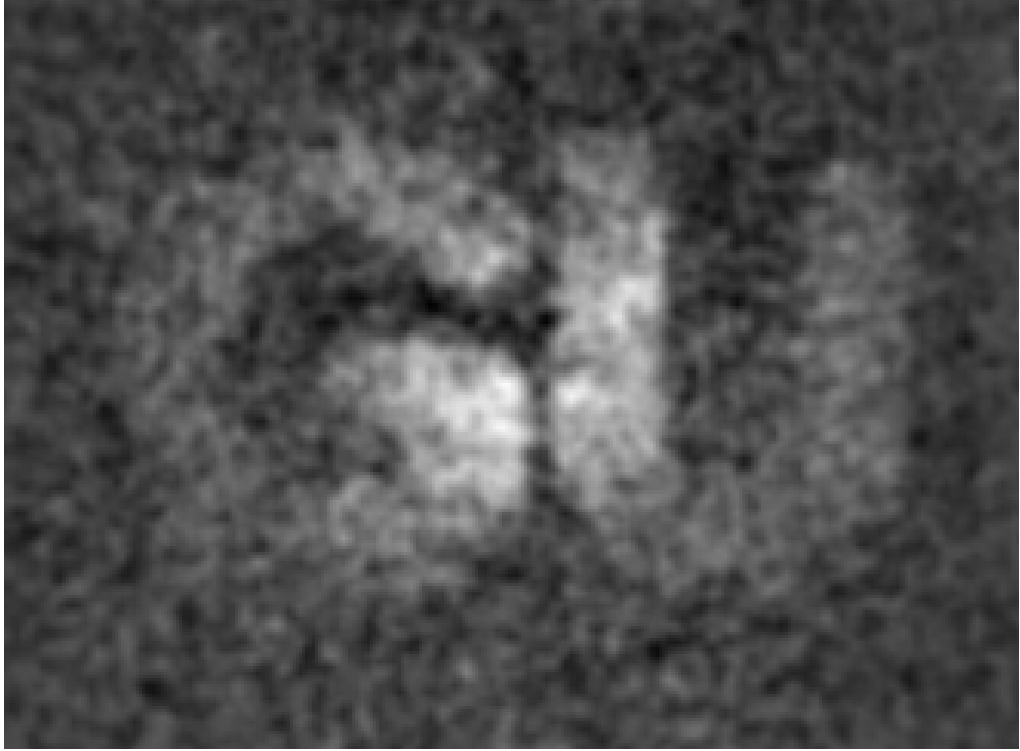


FIGURE 4.1: Reconstructed image of a 3D reflective object using computational GI setup discussed in Chapter. 3. The object contains two 3D-printed letters “G” and “U”.

aperture is used. Fig. 4.2 shows a comparison between two reconstructions of the same object. Fig. 4.2 (a) is obtained by using the transmissive light, while Fig. 4.2 (b) is obtained by collecting the reflective light. The reflective reconstruction with a much lower SNR indicates the difficulty to image a reflective object.

In addition to the low signal level, nonlinear response of the SLM also limits the reconstruction quality. Due to this nonlinear response of the SLM, what one predicts by the hologram is not exact what is generated. For a binary object, this nonlinearity is allowable, because the structure of the target is relative simple and easy to retrieve. For a 3D object with greyscale reflectivity, the generated speckles have to match the hologram well for a proper reconstruction of the complicated structure. One may think that the conventional GI setup which uses a CCD camera to acquire speckle patterns is able to get rid of the nonlinearity issue, however, the use of the CCD camera will introduce extra shot noise from the CCD chip which will also reduce the reconstruction quality, therefore conventional GI using a CCD camera does not necessarily produce

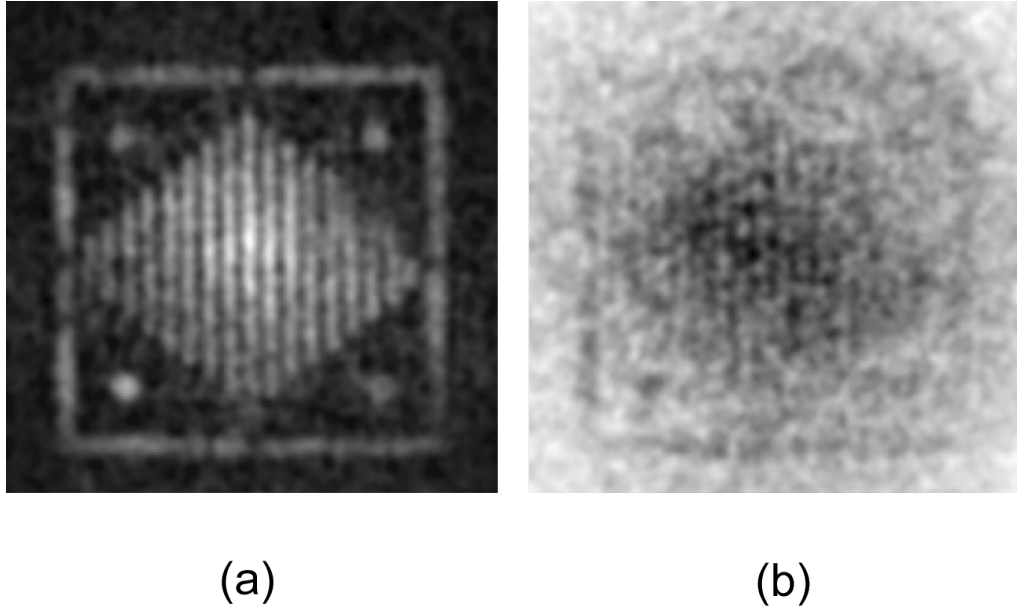


FIGURE 4.2: GI reconstruction of a transmissive object by measuring the transmissive (a) an reflective (b) photons.

better reconstructions than computational GI. To summarise, a 3D reflective object is much more complicated than a 2D transmissive object for GI reconstruction, and will need an adaptive system for correlation measurement.

4.2 Computational imaging with structured illumination

Based on the discussion above, we realise that an appropriate light source is the essential element to image a complex 3D object in GI. The new light source should consist of a programmable SLM with good linearity so that we can predict the speckles accurately. Also, it should be able to illuminate a large area with high intensity. To meet these requirements, we decide to use a light project as our light source. This change then instigates the switch of the structure illumination from thermal speckles to binary “chessboard” patterns. Details of the experiment setup will be discussed in this section.

4.2.1 Experiment setup

Our computational imaging experimental setup is shown in Fig. 4.3. It consists of a digital light projector (DLP) (Light Commander from Texas Instrument) to illuminate

an object with random binary light patterns, a single-pixel photodetector to measure the intensity of the reflected light, an analogue-to-digital converter to digitise the photodetector signals and a computer to generate the random speckle patterns as well as perform 3D reconstructions of the test object. One object investigated was a life-size white polystyrene mannequin head, with approximate dimensions $190 \times 160 \times 250$ mm.

Our bucket detector is composed of a photodiode and a collecting lens. As light intensity scattered from the 3D object is relatively low, a collecting lens is placed in front of the photodiode to increase the numerical aperture of the detector. On the other hand, as the object light cannot be focused into a spot (the smallest focus area of the object is about $5 \text{ mm} \times 5 \text{ mm}$), a photodiode with a sufficient detection area is required. Therefore we choose a Thorlabs PDA100A-EC Si Transimpedance Amplified Photodetectors with an active area of 75.4 mm^2 . It has a response spectrum from 340 nm to 1100 nm with the peak response at 970 nm. And the response speed (bandwidth range) is 2.4 MHz. There is also a gain control to adjust the detection to different sensitivity levels. Acquired photocurrent signals are then sent through an analogue-to-digital converter to a computer. The converter is a Data Acquisition device (DAQ) from National Instrument (NI): NI USB-6221 BNC. It utilises a BNC cable to receive signals from the photodiode and then a USB cable to connect to the computer.

4.2.2 Digital light projectors and digital micromirror devices

In this computational imaging system, the most important component is a programmable DLP. The DLP we use in our lab is a “Light Commander” from Texas Instruments. Structure of the DLP is illustrated in Fig. 4.4. It comprises of an illumination source which contains a red, green and blue light emitting diode to generate red, green and blue light separately. The RGB light is integrated by a integration tube into white light. The white light is then reflected by a mirror onto a digital micro-mirror device (DMD) and modulated with structure illumination. The modulated light patters are projected onto the object by a Nikon 50 mm focal length lens.

Within the DLP, the primary component is the (DMD). A DMD is a reflective spatial light modulator made up of metal mirror arrays [95, 96]. It was first invented in Texas

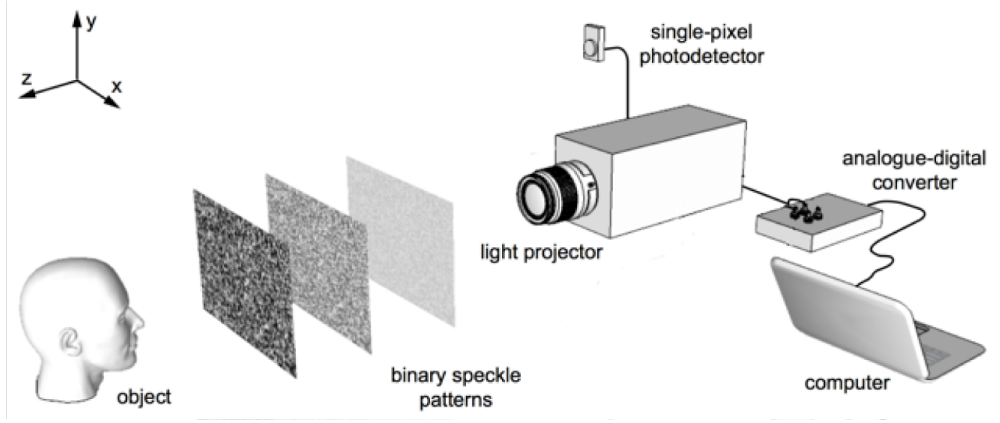


FIGURE 4.3: Illustration of the single-pixel computational imaging experimental setup. The light projector illuminates the object (head) with computer generated random binary speckle patterns. The light reflected from the object is collected by a single pixel photodetector. The signals from the photodetector are measured by the computer via the analogue-digital converter, and used to reconstruct a correlation image.

Instruments in 1980s and then widely used in light projection and optical modulation systems [97–100]. A DMD chip consists of a 2D rectangular array of microscopic metal mirrors. Each mirror can be individually rotated electrostatically by a certain angle ($+12$ degrees and 12 degrees), which corresponds to an on or off state (Fig. 4.5). In the on state, light from the projector light source is reflected into the lens, making the pixel appear bright on the screen. While in the off state, the light is reflected to an absorber, making the pixel on the screen appear dark.

Compared to a liquid crystal spatial light modulator, DMD can be operated much more quickly, with better projection precision and broader bandwidth. Importantly, the large operational bandwidth of the DMD ($300\text{ nm} - 2\text{ }\mu\text{m}$) would enable the use of this technique at other wavelengths that are potentially unsuitable for existing imaging technologies.

The computational imaging system using single-pixel detectors described above is adapted from computational GI. As mentioned before, we use “computational imaging” to distinguish it from computational GI. The two systems have some common aspects. Both of

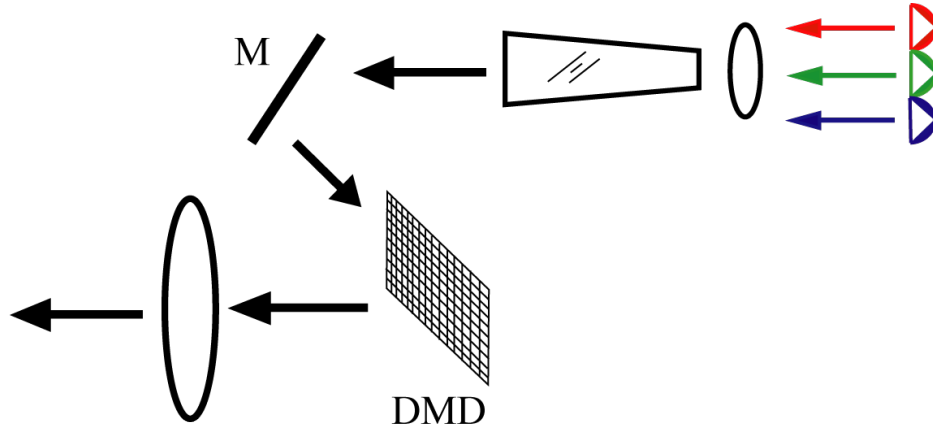


FIGURE 4.4: Illustration of light projector. RGB light are emitted from three photodiodes and passed onto the DMD chip. The modulated light field reflected by the DMD mirrors are projected by a lens onto the image plane of the DMD.

the two systems use structured illumination and single pixel detection. Images are both derived from correlation between the illumination structures and single-pixel signals. The correlation algorithms employed are the same. there are however subtle differences between the two approaches. The most fundamental difference is that a computational GI system utilises time coherent speckles as a light source, and the speckle patterns in a certain plane are calculated based on the propagation function. The computational imaging system, however, uses a projection lens to project binary patterns onto its image plane.

The computational imaging system is also similar to a single-pixel camera system. The only difference is our single-pixel computational imaging system uses DMD to encode the light source for illumination, while the single-pixel camera uses DMD to encode object light in the image plane. Details about the difference of these two systems will be discussed later in Chapter 5.

4.2.3 Depth of field of the projection system

To make sure that computational GI reconstruction is valid for a 3D object, we require the projection patterns to keep unchanged in the whole 3D object space. In other words,

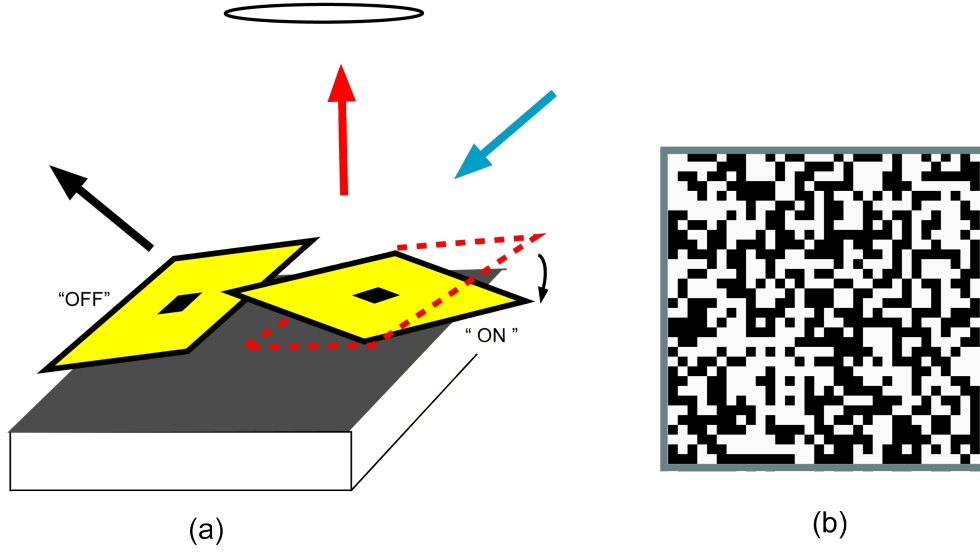


FIGURE 4.5: An illustration of the “on” and “off” states of a DMD pixel (a) and a modulated light pattern.

the depth of field (DOF) of the projection system has to be long enough to cover the longitude size of the object (the size of the object in the propagation direction of light). Here we define the DOF as the front and back plane where both the contrast of the patterns decrease to 50% of that in the focal plane. To quantitatively measure the DOF of the system, we send a strip pattern (Fig. 4.6 (a)) onto the object space and analyse the change of the contrast in the longitude direction. As DOF is related to the image resolution, we combine every 4 neighbouring column of DMD mirrors as a white or black strip, which means the size of the strip pattern in the horizontal direction is equal to that of the projected patterns used for computational imaging reconstruction. A CCD chip is placed in the object area to record the projected strip pattern. The CCD is first moved along the longitude direction to find the focal plane where we get the highest contrast. At this point the contrast is not 1, because the black area of the pattern is not actually “black” due to background light. Therefore we remove the background noise to make the average black pixel values zero. Taking this background subtraction into account, we move the CCD along the propagation of the projected light to locate the two planes where the image contrast reduces to 50% (one in front of the focal plane and the other in the back). The distance between these two planes is the DOF of the system. We get the DOF is 23cm, which means that the system is valid to retrieve a

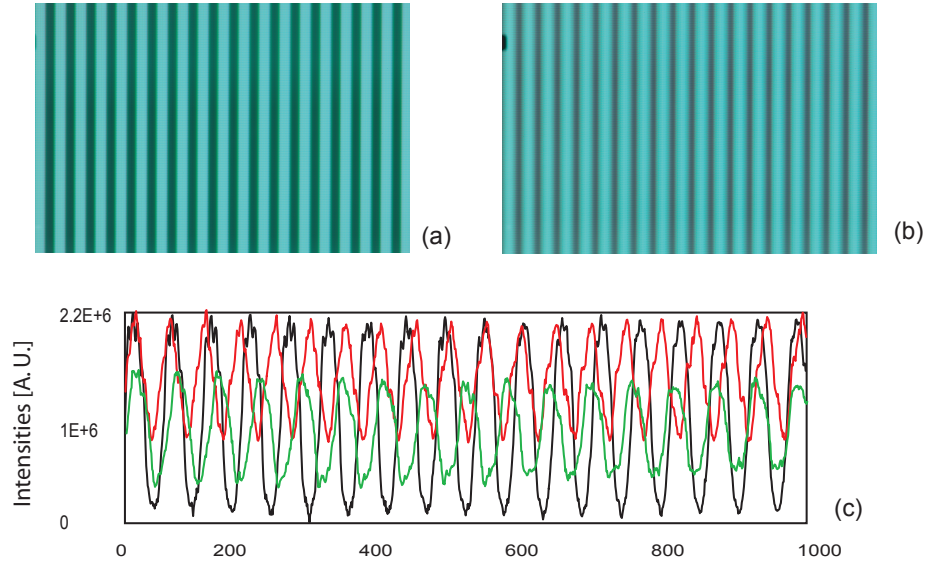


FIGURE 4.6: Measurement of depth of focus of the DLP system. (a) Image of black and white stripes obtained in the focal plane of the projection lens. (b) The image of the same pattern obtained with the contrast reduced to 50%. (c) shows the cross view of the magnitude of the pattern in the focal plane (black line), front out-of-focal plane (red line) and back out-of-focal plane (green line).

3D object within this depth. The mannequin head is 19 cm in the longitude direction, so the reconstruction should be valid.

4.3 Differential computational imaging

Despite the apparatus difference, computational imaging system shown in Fig. 4.3 uses the same correlation algorithms as used in GI for image recovery. The three algorithms discussed in Chapter 3 all use the changes of intensity fluctuation as the correlation varieties, which are obtained as the zero-mean object light intensities and are effected by background noise. To get rid of the background noise, a differential signal acquisition method is introduced. It utilises the bit-plane display of the DLP to display every structured illumination followed by its inverse. The object intensity therefore can be represented as the differential of the two intensities from these two opposite illumination. This differential signal method helps remove the influence of all background noise with a lower frequency to the display speed.





	Iteration 1		Iteration 2	
Structure Light Patterns	l_1 	l_1' 	l_2 	l_2' 
Detected Signal	S_1	S_1'	S_2	S_2'
Differential Signal	$S_{1d} = S_1 - S_1'$		$S_{2d} = S_2 - S_2'$	

FIGURE 4.7: Illustration of speckles and their inverse. l_1 and l_2 are two speckles, and l_1' and l_2' are the inverse. The differential signals are obtained by subtracting S' from S .

4.3.1 Acquisition of differential signals

As discussed in Chapter 3.1, direct correlation of the two beams contains not only the object spatial information, but also featureless background. To eliminate the background noise and increase SNR, the DC component is subtracted from both the bucket signal and the 2D speckles from their correlation (Eq. 3.2). In computational imaging system using binary patterns, as the speckle can be manipulated computationally, the only thing to acquire is zero-mean bucket signals. Rather than measuring the absolute intensity signals and subtracting the mean value, an alternative way to do this is to project pairs of patterns, with each pair containing a pattern and its inverse. The differential of the corresponding signals becomes the zero-mean signals for the pattern.

This method can be easily achieved by taking advantage of the bit-plane display of the DMD. Bit-plane display is a technique that represents of a non-binary number at each pixel of an image with a set of bits. In computer graphics, a true colour (RGB) display employs a 24-bit number to represent a RGB pixel. Within this 24-bit number, each colour is represented by 8 bits. Therefore each colour can be displayed in a space of 256 degrees (0 – 255). In the case of light commander, the display can be switched between two modes. In a video mode, the DLP system works in a way to display true colour images in a high speed (60 Hz). For one true colour image, the R/G/B components are displayed alternatively within a period of 1/60 second (one frame). In any time

of such a frame, one colour get displayed, by switching the corresponding LED on and displaying the corresponding bit planes on DMD chip. In the other mode, which is called “structure light mode”, all the three LEDs are on at all the time to produce a white light illumination, and the 24 bit numbers are displayed in sequence. This structure light mode is an ideal situation for displaying binary patterns with their inverse. For one frame, we combine a binary pattern and its inverse (Fig. 4.7) alternatively for 11 times, which takes 22 bits of the frame. The other 2 bits left are used as triggers for synchronisation measurement. This process is shown in Fig. 4.8. Every frame starts with a bit plane with all the pixels on to generate a high signal, and then follows the second bit that turns all the pixels off. The other 22 bits are coded alternatively with a speckle and its inverse. Once a 24 bit number is integrated as a frame and sent to the DMD (and note that it is the minimum unit that DMD can be controlled through computer), it will be displayed repeatedly in 60 Hz. To acquire the signals from a whole frame, we force the system to acquire two triggers in order to distinguish a whole frame. The DAQ is set to sample at a rate of 57.6 kHz, which means from every frame there are 960 samples. To make sure we acquire two triggers to select a frame, we take 2000 samples (slightly more than two frames) for every speckle (Fig. 4.8 (a)). Once a frame is picked out (Fig. 4.8 (b)), a digital filter as shown in Fig. 4.8 (c) is used to modulate the signals. Notice that mirrors in the DMD chip are switched in every bit plane, and because of their finite response speed, signals measured in the raising and falling period of each bit plane display may contain noise. In order to get ride of these noisy signals, the first 2 and last 3 samples for every bit plane is discarded, leaving 30 samples for each bit plane. The filtered signals are then averaged to 11 signals (the first 2 bit planes are also discarded), and the average of the these 11 signals finally works out the signal for the corresponding speckle pattern.

4.3.2 Experimental results

These differential signals together with their light patterns are then sent to the correlation algorithm to retrieve an image. As the differential signals are zero-mean signals already, the correlation function can be simplified as

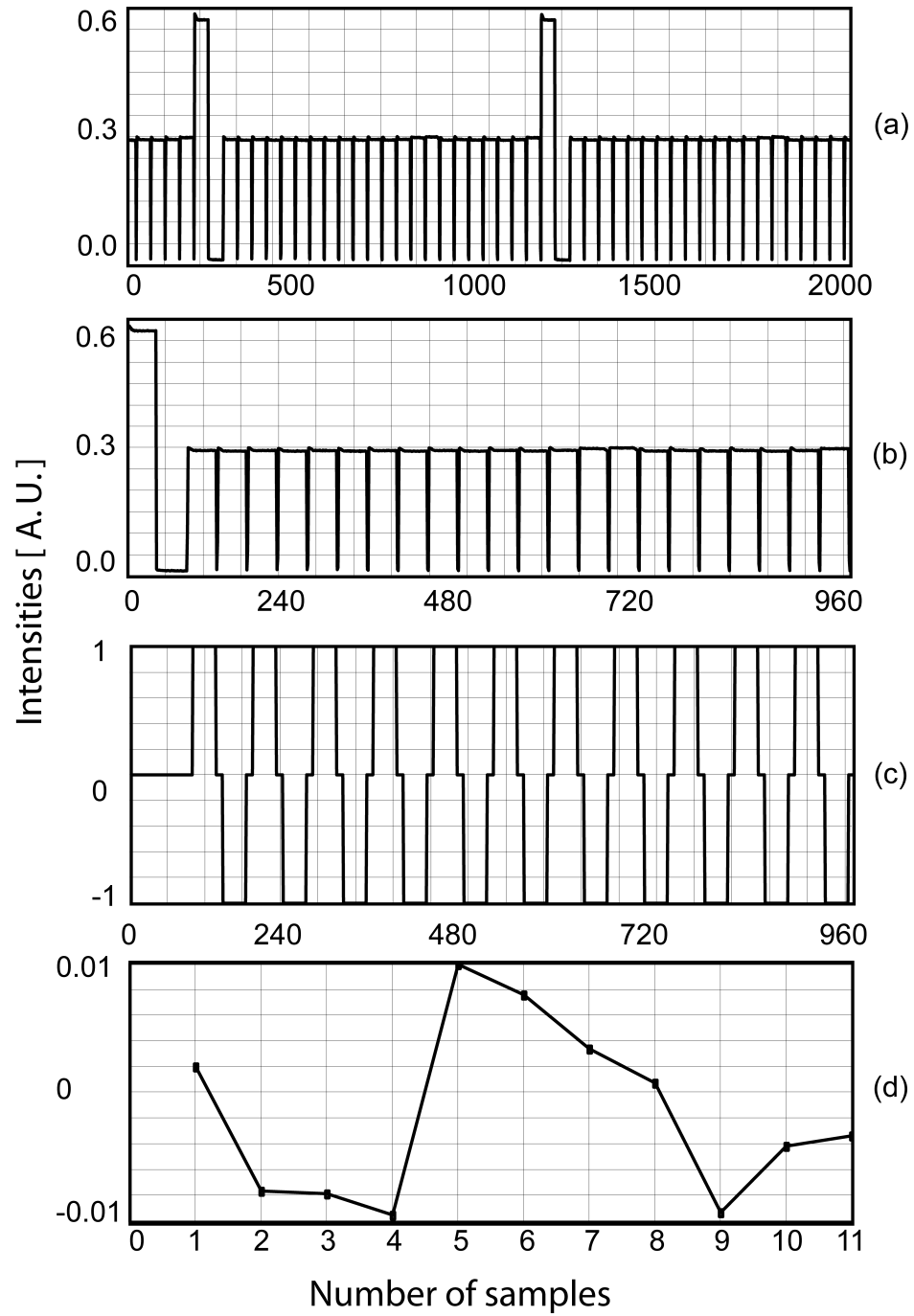


FIGURE 4.8: Differential signals. (a) Acquisition of 2000 samples. It contains signals for one light pattern and its inverse and two pair of triggers. (b) Signals of one frame of illumination from the DLP. (c) Filter for signals in one frame. (d) The differential signals.

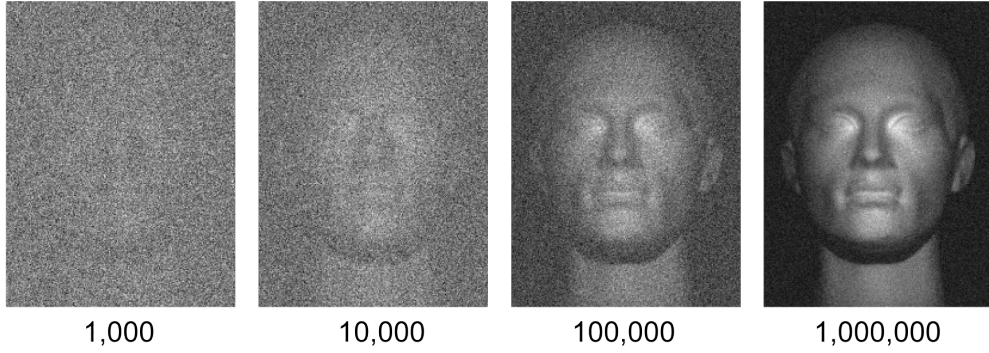


FIGURE 4.9: Source ghost image reconstructed using the TGI iterative algorithm iteratively from 1000 to 1,000,000.

$$I(x, y) = \langle \langle S_i \rangle \langle P_i(x, y) \rangle \rangle, \quad (4.1)$$

here $P_i(x, y)$ are binary patterns containing -1 s and 1 s rather than 0 s and 1 s, with all the 0 s being replaced by -1 s.

The Light Commander contains an array of 1024×768 mirrors in the DMD chip, which determines the maximum pixel numbers of the projected patterns. In our experiment, we assemble every 4×4 mirrors into one unit (pixel), so that the projection patterns are in 2D arrays of 256×192 pixels. During the projection, each “pixel” is randomly switched on or off, rendering the projection as binary patterns (0 s and 1 s). The patterns are then projected onto the object, which is placed 1.2m away from the projection lens. To increase SNR of the reconstruction, we set the black (0) to white 1 s pixel ratio in all projection patterns as 1:1, so that our system is a SNGI system as discussed in Chapter 3. Using Eq. 4.1 we obtain 2D reconstructions of the object, shown in Fig. 4.9. The four images are obtained after 1 thousand, 10 thousand, 100 thousand and 1 million iterations respectively. The final image reconstructs the object with reasonable details. Fig. 4.10 shows some other images obtained from the system.

Although images in Fig. 4.9 are obtained in a dark room without background noise, the advantage of using differential signals enables us to perform the same experiment with low frequency background light on. As one differential signal is obtained during the display of two bits ($1/720$ seconds), it automatically filters low frequency noise. In

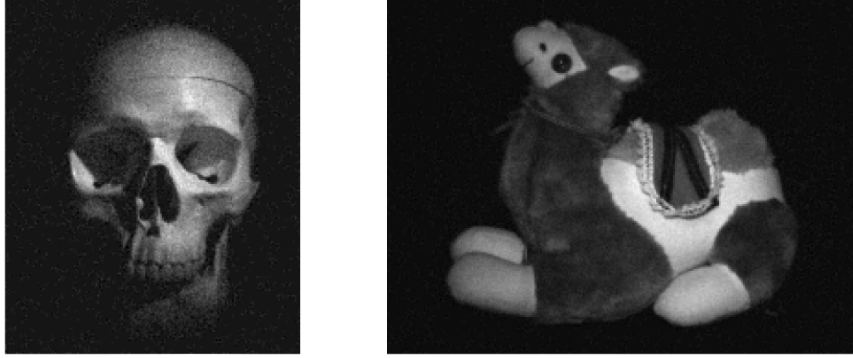
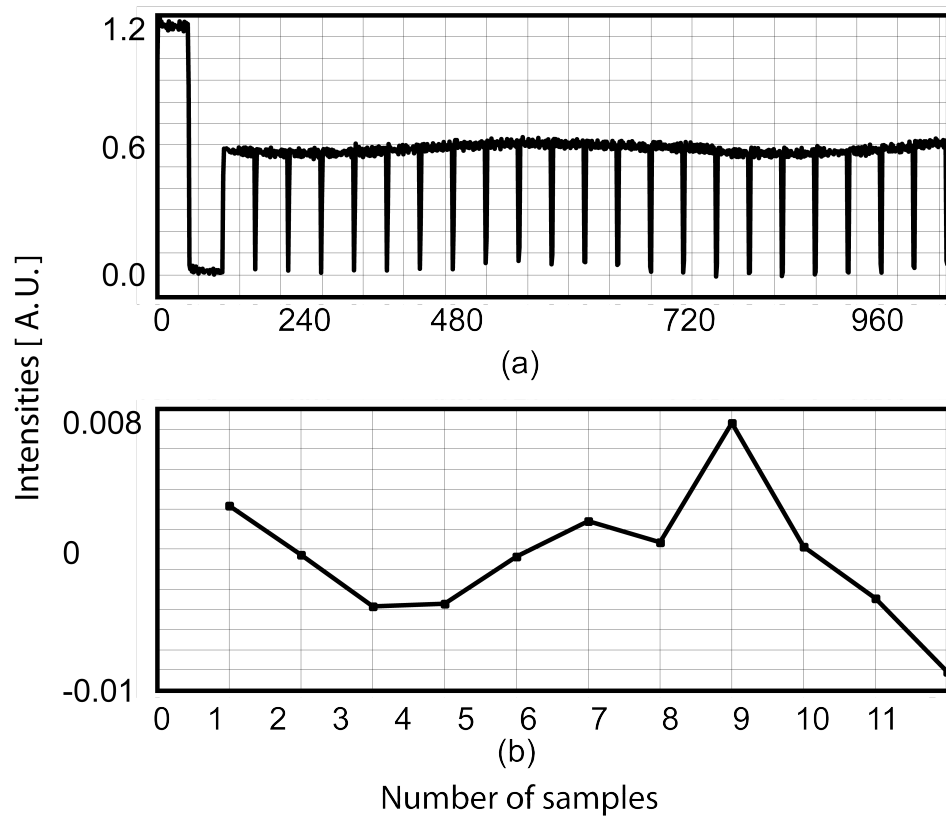


FIGURE 4.10: 2D computational images of a sample skull and a toy camel.

our case, the frequency of oscillation from room lights is 100 Hz, which is much lower than the frequency of the differential signals in 720 Hz. Therefore the room light can be filtered out automatically. Fig. 4.11 shows a comparison between reconstructions with and without room light. Fig. 4.11(a) shows signals acquired with room light in one frame. Compared to Fig. 4.8(a) it contains a fluctuation with a longer period. This low frequency signals, however, cannot stop us to work out the effective differential signals (Fig. 4.8(b)). The image obtained with room light (Fig. 4.8(d)) is slightly noisier than that obtained from a darkroom, but still in a good quality.

4.4 3D computational imaging utilising structured illumination

In this section we extend the technique developed above to retrieve the 3D form of the object. This is achieved by using several single-pixel detectors in different locations around the object. From each detector we derive a 2D image that appears to be illuminated from a different direction whilst using a single digital projector as light source. All these images have the same shape, but different shadings, which is determined by both the surface shape and the detecting directions. Using an approach called shape from shading, the surface gradients and hence the 3D reconstruction of the object can be obtained by comparing the shading information of from different images. We compare



(c)



(d)

FIGURE 4.11: (a) Signals of one frame illumination obtained with room light on. (b) The rendered differential signals. (c) A reconstruction of a toy skull without room light compared with the same reconstruction with room light on (d).

our 3D result to that obtained from a stereo-photogrammetric system utilising multiple cameras.

4.4.1 Computational imaging setup with multiple single-pixel detectors

The experiment setup for 3D reconstruction is adapted from the 2D reconstruction system discussed in Section 4.2. All the setups are the same except that there are four single-pixel detectors rather than one. It is worth mentioning that crossed polarisers in the DLP and detectors are used to get rid of specular reflection. Details will be discussed later.

The four spatially separated single-pixel photodetectors are positioned in a plane 1000 mm away from the object, separated by 500 mm and each pointing towards a common point on the object to record the back-scattered light (Fig. 4.12). The whole space can be marked as a Cartesian coordinate system with three axes (x, y, z) , with the origin being chosen as the centre of the projected light patterns on the image plane. Therefore the four detectors are at $(-50, 0, 100)$, $(50, 0, 100)$, $(0, 50, 100)$, $(0, -50, 100)$ in the unit of *centimetres*. For every binary pattern projected, the corresponding object intensity is measured by each photodetector, which is fed to a computer algorithm. Iterative results from the four detectors are shown in Fig. 4.13. All the images here are in a resolution of 192×256 pixels.

Now we focus on the final results obtained after one million iterations, shown as the last row of Fig. 4.13. By comparing these four images we find that all these four images have the same shape, and the only difference is their intensity distribution. For example, the one obtained from the top detector has a strong shading in the chin area. It indicates that the direction is determined by the position of the detectors in GI. And this properties will be discussed in detail and employed for the 3D reconstruction.

4.4.2 Shading property of computational images

In this section the shading property of the image from the previous computational imaging system is discussed. As mentioned above, the shading profile in a computational imaging system with single-pixel detectors is determined by the detection element rather than illumination, which is reciprocal to a conventional camera system. This is because

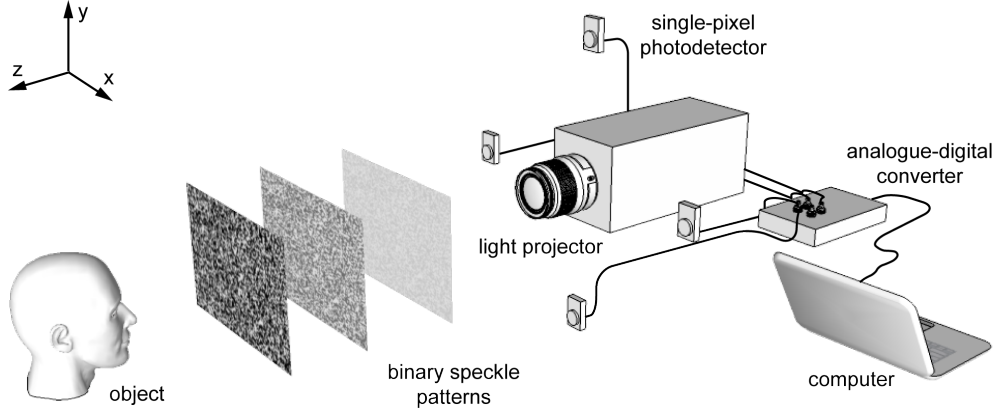


FIGURE 4.12: Illustration of the experimental setup used for 3D surface reconstructions. The light projector illuminates the object (head) with computer generated random binary speckle patterns. The light reflected from the object is collected on 4 spatially separated single pixel photodetectors. The signals from the photodetectors are measured by the computer via the analogue-digital converter, and used to reconstruct a ghost image for each photodetector.

the detection element in single-pixel imaging is non-pixelated, just as the illumination in a camera imaging process. In our computational imaging system, once the illumination direction is fixed, the intensity distribution of the reconstruction is determined by the relative orientation of the object surface and the relative position of the detector.

In both GI and computational imaging using single-pixel detectors, a pixel in the GI reconstruction is determined by a corresponding pixel (P^0) in the structure illumination. This is because the light source is the component that contains spatial information (pixel related), and the detector simply only measures the total power. Once the emission power from the illumination pixel is fixed, the projection power on the corresponding area of the object space is conservative, though both the projection area size and surface light intensity may vary due to different incident light angles (Fig. 4.14 (a)). Assuming a Lambertian surface that conducts perfect diffuse diffraction, the scattered light luminance in all direction is the same, therefore the power of the scattered light detected by the bucket detector is only dependent on the cross area of the projection area viewed by the bucket detector. And according to TGI algorithms shown as Eq. 4.1, the intensity value at any pixel of a computational image is proportional to the total light intensity

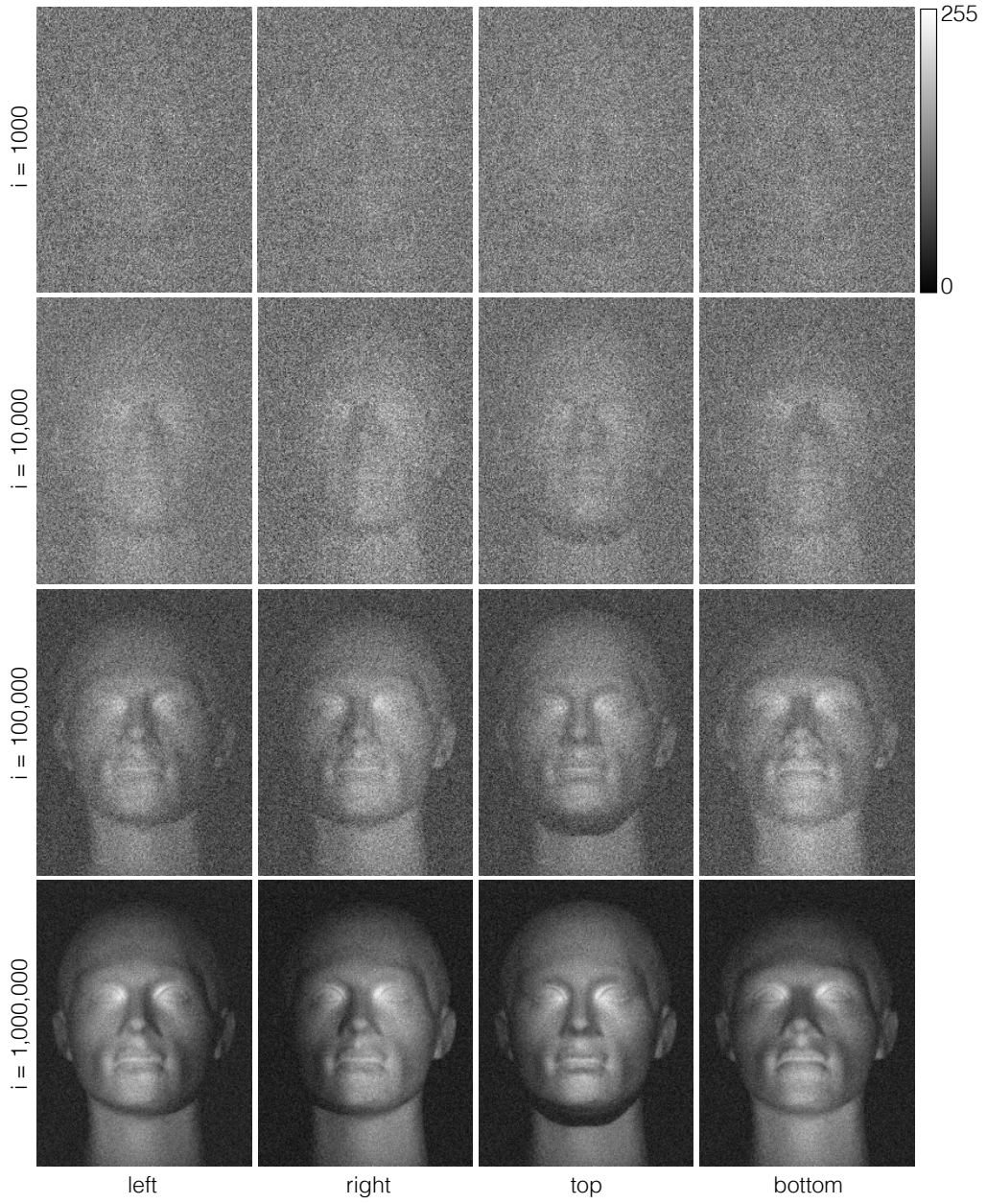


FIGURE 4.13: Source ghost images from each photodetector employed in the system, reconstructed using the TGI iterative algorithm iteratively from 1000 to 1,000,000. The spatial information in each image is identical, however the apparent illumination source is determined by the location of the relevant photodetector, indicated underneath.

from the corresponding area. Therefore once the incidental light is fixed, the pixel intensity will change as a function of the detecting vector. Based on the discussion above, the image intensity of a pixel from computational correlation imaging (Fig. 4.14 (b)) can be expressed as

$$I \propto I^0 \cdot (\mathbf{n} \cdot \mathbf{d}). \quad (4.2)$$

Here (I^0) is the incident light intensity, S is the bucket signal, and \mathbf{d} and \mathbf{n} are the detecting vector and surface normal at this pixel. Note that both \mathbf{d} and \mathbf{n} are unit vectors pointing outwards from the object surface.

To further understand the shading property of a computational imaging system, we compare the computational imaging system with a normal camera system, where we replace the projector with a camera and the bucket detector with a light bulb (Fig. 4.14 (e)). In this conventional imaging scheme, the intensity of a pixel is determined by the field of view of the imaging lens. Once the field of view of the lens is fixed for a given camera, the pixel intensity on the image is only effected by the scattered intensity in the detecting direction. Again, for a Lambertian surface, this scattered intensity is only determined by the incident light, while is independent to the detecting angle. Therefore the pixel intensity in a camera image is

$$I = I^0 \cdot (\mathbf{n} \cdot \mathbf{l}). \quad (4.3)$$

To compare these two image systems with experimental data, the four detectors shown in Fig. 4.12 are replaced with four LED light sources and the projector is replaced with a camera. Four images are taken using the camera, each with only one light source on. The four camera images (Fig. 4.14(f)) obtained have the same intensity distribution as the corresponding computational image (Fig. 4.14(c)). Although light travels in opposite directions for the two imaging systems in, the images acquired from both are equivalent. The usual rule, that the image brightness (strictly the luminance) depends on the angle to the light source and not the angle to the camera or eye, must be re-stated to be compatible with computational imaging: the luminance of the image depends on the angle between the surface and the non-pixelated element, and not in the angle between the surface and the imaging component. In conventional imaging, the non-pixelated element is the light source and the imaging component is the camera, or an observer's eye. For computational imaging systems however, the pixelated component is the projector (i.e. the light source), and it is the detector that is the non-pixelated element.

4.4.3 Computational imaging with multiple illumination directions

The discussion above is about a computational imaging experiment with different detections which renders different shading of the image. While the non-pixelated element in an imaging system determines the shading property of an image, the pixelated element determines its shape information. In a computational imaging system with single-pixel detectors, the pixelated element is the light source. Therefore a complement experiment to that discussed above is done with the light project being placed in different positions relative to the object. The experiment setup can be understood through Fig. 4.3, with only one light source and one detector. The experiment is done twice, each with the light projector being placed in a different point of view relative to the object. When taking real data, this can be simply achieved by rotating the mannequin head relative to the DLP. Fig. 4.15 shows two images of the mannequin head with different shapes, with the perspective set by the position of the DLP. Same pictures can be taken with a camera from two view points (left and right) where the DLP is placed.

4.5 3D GI reconstruction using photometric stereo

In this section we utilise the shading properties discussed above to retrieve the 3D information of the object. In a conventional camera system, the intensity distribution of an image is different under different illumination. In a computational imaging system with single-pixel detectors, the intensity profile looks different when it is detected from different directions. In both cases, the different appearance in the 2D images can be utilised to infer the lost 3rd dimension, recovering the depth information of the scene. The technique that uses this observation to reconstruct a 3D surface from a single image under a particular illumination is called shape from shading (SFS). In this section we are going to apply this technique developed for use with conventional cameras onto our computational imaging system for 3D reconstruction.

4.5.1 3D imaging methodology

Depth information of a scene is otherwise lost in a 2D image, but there are instances where it can be inferred. Both conventional camera and single-pixel imaging systems image a scene by projecting 3D space onto a 2D plane, thus in order to obtain 3D information from 2D computational images we must perform the inverse problem.

In any one pixel of a 2D image the intensity is determined by the surface reflectance and surface geometry at that point, as well as the incident lighting. The technique that retrieves 3D information utilising this 2D intensity image is called 'shape from shading' [101–110]. Using a single image this method relies on the shadows cast by geometrical features to reveal the depth of the scene, and assuming a uniform Lambertian reflectance model and known light sources located at infinity, such that the incoming lighting vector is constant. An extension of this technique known as “photometric stereo” [111–115] provides a better solution by adopting the same assumptions but requiring multiple images from the same view point under different illumination. Although the single viewing point limits both these techniques to estimate depth from only one side and is consequently only able to recover 2.5D, the method benefits by not having to establish correspondences between pixels like other methods.

A different approach for deriving 3D surface information utilises multiple 2D images of a scene from different points of view taken simultaneously and finding the correct correspondences between pixels, sometimes referred to as 'dense stereo' [116, 117]. Points from different images are in correspondence when they are from the same physical point in space via perspective projection. Once correspondence is established, it can be used to determine the 3D profile of the object. This can be simply done by triangulating the position of the correspondence [118]. For shape reconstruction, similar priors such as uniform reflectance and constant illumination are typically assumed.

Another 3D mapping method known as “structured illumination” [119], actively illuminates a scene using a set of specially designed 2D patterns and taking images from a particular viewpoint. Many different techniques exist within this topic but the underlying principles behind them all is that geometrical features in the scene will create

distortions to the incident patterns from the viewpoint of the imaging device. It is by accurately measuring the pattern distortions in the images that 3D surface information can be obtained.

As will become apparent to the reader, the method described here to retrieve 3D surface information with computational images, is an amalgamation of all aforementioned techniques. The imaging system utilises a light projector to produce random speckle patterns from a single source (structured illumination) from which the reflected intensities are measured by multiple single pixel detectors (dense stereo) and correlated to produce images. However the use of multiple detectors does not offer different perspectives of the scene but instead provides identical spatial information under different illumination (photometric stereo) in the ghost images retrieved (Fig. 4.13).

4.5.2 Shape from shading to photometric stereo

Shape from shading recovers 3D information from a single 2D intensity image based on the fact that surface reflection follows certain principles. To solve the SFS problem from a single image, usually some reflectance property is assumed. Also, most methods assume orthographic or perspective projection so that each scene point has the same incoming light distribution. Fixed scene illumination, surface-reflectance properties, and imaging geometry can be integrated into an explicit model that allows image brightness to be related directly to surface orientation.

Thus we can associate with each point in gradient space the brightness of a surface patch with the specified orientation. The result, usually depicted by means of isobrightness contours, is called the reflectance map, $R(p, q)$. It is convenient to denote the surface gradient by the first partial derivatives of z with respect to x and y :

$$p = \frac{\partial z}{\partial x}, q = \frac{\partial z}{\partial y}. \quad (4.4)$$

$R(p, q)$ is used to represents the relationship between surface orientation and surface brightness. The map is defined in gradient space. The reflectance map is a convenient

tool, since it provides a simple representation of the constraint inherent in one image-brightness measurement. Once the brightness map, $E(x, y)$, is known, one can ask what the surface orientation might be. A measurement of image brightness restricts the possible surface orientations at the corresponding point on the surface of the object. This constraint is expressed by the image-irradiance equation

$$R(p, q) = E(x, y), \quad (4.5)$$

Therefore to solve the SFS problem is abstracted into solving this equation. However, the SFS problem is known to be an ill-posed problem. For example, a number of articles show that the solution is not unique. This can be simply understood in the way that because for each point of the surface, there are two unknown variables (p, q) in the reflectance map, while there is only one restriction (the intensity map), rendering the problem under determined.

An extension of SFS called photometric stereo (PS) [111] also utilises the shading information of 2D images from 3D mapping. The difference is PS uses several images rather than one image for the 3D reconstruction. And the images used are taken from the same viewpoint but with different illuminations. Each image leads to a equation as Eq.4.5. With a large number of restrictions, the problem can be fully determined. Although this is developed under conventional camera system, the principle can be adapted by the computational GI system.

In computational imaging using single-pixel detectors, multiple images are not taken from different illumination directions. Instead, the structured illumination of the system (Fig.4.12) is uniform, while it is the different detection directions that produce different images with different intensities as the source images. As the only pixel-related component, the light source determines the spatial distribution of the image. Therefore all the images obtained have the same shape. The difference between these images is solely their intensity distribution.

The intensity distribution is determined by the relative orientation between the object surface and the detection direction. According to Eq.4.3, the intensity of a pixel, $I(x, y)$,

in the image obtained from the n^{th} detector can be expressed as

$$I_n(x, y) = \alpha (\mathbf{L}_n \cdot \mathbf{N}) , \quad (4.6)$$

here α represents the surface reflectance, \mathbf{L}_n is the unit illumination vector pointing from the detector to the object and \mathbf{N} is the surface normal unit vector of the object.

$$\mathbf{L}_n = (l_x, l_y, l_z)_n . \quad (4.7)$$

The surface orientation cannot be determined from a single intensity, since many orientations can bring about the same intensity. Therefore to fully determine the image geometry we must obtain at least three separate images, but in our system it is just as simple to capture four images. Thus for all images we can write Eq. 4.6 in matrix notation as

$$\begin{bmatrix} I_1 \\ I_2 \\ I_3 \\ I_4 \end{bmatrix} = \alpha \cdot \begin{bmatrix} l_{x1} & l_{y1} & l_{z1} \\ l_{x2} & l_{y2} & l_{z2} \\ l_{x3} & l_{y3} & l_{z3} \end{bmatrix} \cdot \begin{bmatrix} n_x \\ n_y \\ n_z \end{bmatrix} ,$$

which can be represented as $\mathbf{I} = \alpha \cdot \mathbf{L} \cdot \mathbf{N}$,. For any pixel (x, y) the unit surface normal is given

$$\mathbf{N} = (1/\alpha) \mathbf{L}^{-1} \cdot \mathbf{I} , \quad (4.8)$$

and the reflectance is given by

$$\alpha = |\mathbf{L}^{-1} \cdot \mathbf{I}| . \quad (4.9)$$

From the surface normals calculated at each pixel it is possible to determine the gradient between adjacent pixels from which we obtain the surface geometry by integration. In fact, as we record four images, the problem becomes overconstrained as the surface normals represent only two degrees of freedom per pixel. We can thus remove our assumption of uniform reflectivity and recover an estimate of the surface reflectance α at the same time as finding the object's shape.

4.5.3 System calibration

All of the discussion above is based on the assumption of Lambertian reflection. A Lambertian surface is a reflection surface that obeys Lambert's cosine law for reflection. Lambert's cosine law says that the radiant intensity measured from an ideal diffuse reflecting surface is directly proportional to the cosine of the detecting vector and the surface normal. The luminance (or generally intensity) from such a surface is therefore uniform when viewed from any angle. The intensity is the same because both the emission power and the apparent size from a certain area is reduced by the cosine of the detection angle, therefore the intensity as the ratio of these two variables keep as a constant. However, for most objects, the surface reflectance contains both specular and diffuse (Lambertian) components. While diffuse reflection scattered light uniformly in all directions, specular surfaces cause the reflectivity to be nearly zero everywhere except at the angle of incident light while diffuse surfaces reflect light nearly equally in all directions.

The mannequin head we use is made from polystyrene with a smooth surface. The reflection off the object is mostly Lambertian but also contains a small part of specular reflection, which should be eliminated because it will reduce the 3D reconstruction accuracy. It is known that specular reflection conserves polarisation while diffuse reflection produces random polarisation. Therefore to get rid of the specular reflection, we add some cross polarisers in the system. A linear polariser is added in front of the projection lens and polarisers with the orthogonal polarisation are added on the photodetectors. To test the Lambertian property of the surface with the use of cross polarisers, we conduct an experimental measurement using a flat white surface made of the same material (polystyrene) as the mannequin head. We set the surface normal of the flat surface to point towards the light source, and measured the light reflected on a photodetector at different angles from the illumination vector. During the measurement, the photodetector always points towards the centre of the surface and keeps the same distance from it. We observe close agreement between our results and the theoretical curve representing Lambert's cosine law for luminous intensity. The reflection properties has been shown

in Fig. 4.16. The cosine line of the reflection intensity shows that the mannequin head surface viewed after cross polarisers is a good Lambertian surface.

It is worth noting that the use of crossed polarisers in the illumination and detection apparatus ensures that our experiment is unaffected by specular reflections.

Before conducting the 3D reconstruction process, the system is calibrated to guarantee measurement precision. As discussed, the photometric stereo method works with the assumption of Lambertian reflection.

To make sure that all the detectors face towards the centre of the object exactly, we use a flat polystyrene surface perpendicular to the projection light to calibrate the system. We adjusted the angles of the detectors so that they all receive a maximum signal from the flat surface.

To test the calibration of the system, we first 3D reconstruct a object with simple geometric complexity: a ball made from the same material of the mannequin head. The 2D images from the four detectors can be seen in Fig. 4.17. And the 3D reconstruction can be viewed in Fig. 4.18. The diameter of the ball is 15cm, and the relative errors of the 3D reconstruction is 1%. The data shown here is just to show the precision of the system, while the detailed process of the reconstruction will be discussed in the next part with the use of the mannequin head.

4.5.4 3D reconstruction algorithm

The process of 3D reconstruction can be seen in Fig. 4.19. We first calculate the surface normals pixel by pixel based on Eq. 4.8. Pixel intensities are from the four 2D images obtained from the four detectors (the last row on Fig. 4.13), and detecting vectors are measured from the experiment setup. Calculated surface normals and the reflectance can be seen from Fig. 4.20. We then calculate the surface gradients from the surface normals for each pixel

$$p = \frac{n_z}{n_x}, q = \frac{n_z}{n_y}. \quad (4.10)$$

The gradients were subsequently integrated to recover a depth-map of the object. Starting in the centre of the object and working outwards, the height for each pixel was estimated based on the height and the gradient at each of its nearest-neighbour pixels. Thus, the integration was performed iteratively, each pass over the object estimating the height of all the pixels having at least one nearest neighbour with a height estimate to work from. For pixels that have more than one nearest neighbour with an estimated height, the height is calculated from the average of those pixels. This simple algorithm works from the middle of the object outwards, and is capable of integrating around holes in the object where there is no information.

4.5.5 Quantitative analysis of the 3D profile

To quantify the accuracy of our approach the 3D reconstruction of the test object was compared with a 3D image captured from a stereo-photogrammetric camera system (Di3D[®]). The system uses normal digital cameras and flash illumination to capture simultaneously pairs of stereo images of a object. Each stereo pair of images is processed using passive stereo photogrammetry software to derive a dense range map image. The range map images and original 2D images are then merged together to form a complete 3D surface image.

The Di3D system consists of two camera pairs placed at two sides of the face to take stereo images. Each pair contains a pair of digital cameras. The cast was simultaneously illuminated by a flashlight. The resolution of the cameras is 4500×3000 pixels, with a focal length of 50 mm. The four 2D images obtained by the cameras are sent to a matching algorithm to recover the height map. The accuracy of this system with facial shapes is well documented [120] to have a root mean square (RMS) error of order 1 mm. Unlike other methods of 3D scanning, DI3D does not require any pattern projection or laser scanning onto the scene. Instead, the image capture process is instantaneous and produces the highest resolution 3D surface images with true photographic quality.

To compare the facial profiles measured by the two systems, the shapes are characterised by anatomical landmarks, which are well-defined facial locations [121] (for example, nose tip, mouth corners etc.). Fig. 4.26 shows two sets of 21 landmarks superimposed on the

facial images by a trained observer. After lateral and angular registration and subsequent depth scaling, the RMS error of our ghost profiler is found to be slightly below 4 mm.

Beyond showing that high-quality images of real life objects can be captured using a single-pixel photodetector, our experiment demonstrates that by using a small number of single-pixel detectors, computational ghost imaging methods can give 3D images.

We have applied this 3D ghost imaging technique to record a facial shape, indicating good quantitative agreement with existing imaging technology based on stereo-photogrammetric systems that employ several high-resolution cameras. An important difference in our approach is that a single projector determines the spatial resolution of the system, removing issues of pixel alignment associated with multiple cameras. Furthermore, reversing the fundamental imaging process allows for simpler, less expensive detectors to be utilised. The operational bandwidth of the system is limited not by the efficiency of a pixelated imaging detector but instead by the reflectivity of DMD used for light projection, whose efficiency extends well beyond the visible spectrum. Development of such technology, for example the use of a broadband white light source, could enable computational imaging systems to become a cheaper alternative for applications in 3D and multi-spectral imaging.

4.6 Computational imaging with single detectors detecting object light reflected by a wall

As discussed in Section 4.4.2, a single-pixel imaging system and a normal camera system are reciprocity in terms of image shading properties. The detectors in computational imaging with single-pixel detectors play a counterpart role as setting the apparent illumination angle. In a camera system, the imaging process does not require the light source to illuminate the object directly. Light can be reflected before arriving at the object (Fig. 4.24(b)). The imaging process can be achieved as long as there is some light scattered onto the object. Inspired by this phenomenon, we can setup a computational imaging experiment with the detector receiving the object light indirectly. As shown in Fig. 4.24(a), a screen is set between the object and the detector so that the reflected light

off the object cannot be “seen” by the detector directly. Yet, there is a polystyrene plane placed in a way that the object light can be made incident onto the detector. As the detector in this computational imaging system is the non pixel-related device and can only measure light power, as long as the phase diffuser can reflect light proportionally to the object, a computational imaging reconstruction can be observed.

We test this idea in our system shown in Fig. 4.12 with the detection part adjusted. The single-pixel detectors are tilted so that they cannot receive the object light directly. One square polystyrene flat plane ($10\text{ cm} \times 10\text{ cm}$) is placed in such a way that the object light can be reflected onto the detector. The 2D reconstructions are shown in Fig. 4.25. The shading distribution indicating the detection direction is still obvious, which indicating the possibility of 3D reconstruction using Eq. 4.8. However, the detecting direction here is determined by the positions of the polystyrene planes rather than the detectors. Because of the relative large size of the detection area, the detecting vector from one “detector” has a large variation. According to Eq. 4.8, the recovery of surface normals and hence the 3D profile are therefore less precise.

4.7 Conclusion

To summarise, we have developed a single-pixel computational imaging system using a digital light projector (DLP) as the light source for structured illumination. A series of binary random patterns were generated to illuminate a real-life size 3D object. A single-pixel photodiode was used to collect the back-scattered light intensity. These detected light intensities were then collected to correlate with their corresponding binary patterns to give an image of the object. This single-pixel computational imaging system was adapted from our computational ghost imaging (GI) system discussed in Chapter 3. An important change was that the speckle generator was replaced by a DLP. Also a differential signal acquisition method was employed by projecting any patterns with their inverse using the bit plane display technique of the DLP. Compared to the original GI system, it provided a much better reconstruction of a 3D reflective object with reasonable details. A high speed performance of the differential signal acquisition method enabled

us to isolate low frequency room light noise and conduct the imaging process with high level background noise.

A computational imaging system with four single-pixel detectors was developed which extended the image reconstruction from 2D to 3D. The 3D reconstruction was achieved by using the four 2D images with different intensity distribution in an algorithm called “photometric stereo”. To obtain four 2D images, the 3D computational imaging system utilised four single-pixel detectors located with spatial separation in the back-scattered space to collect object light from different directions. Each detector generated an independent image. The images from the four detectors all had the same shape but different shadings. Under the uniform illumination, the shading information was determined by the detecting angle between the surface normals of the object and the detecting vector. This was reciprocal to a camera system where shading information was determined by illumination vector. Moreover, based on the fact that the shading property of an image was determined by the detecting vector, the technique called photometric stereo could be employed to retrieve 3D information of the object. Taking the detecting vectors into account, the surface normals and hereby the height information of the object can be derived by comparing the different shading information in the four images. The 3D profile obtained from the computational imaging system was compared to that obtained from a commercial system which showed high precision.

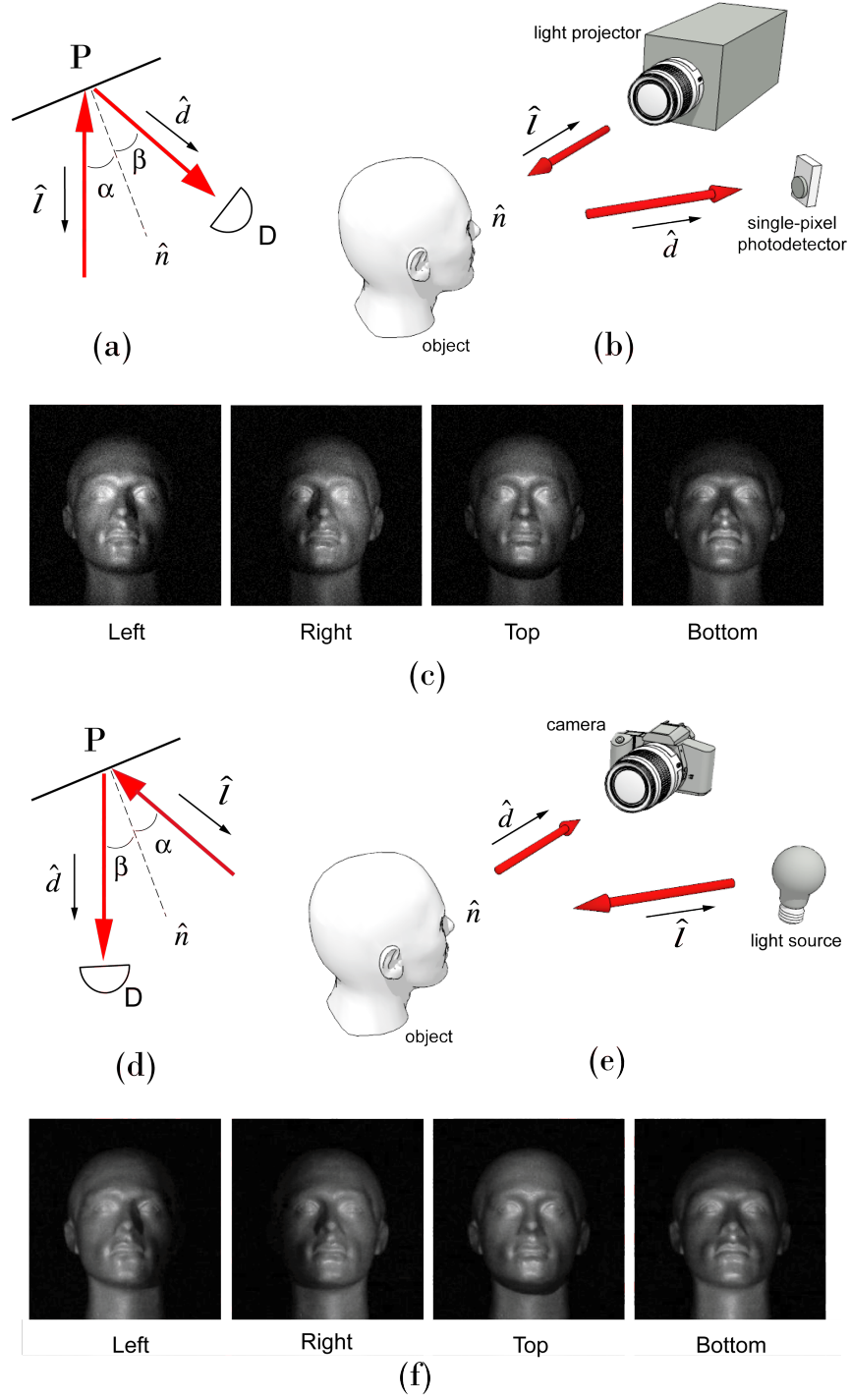
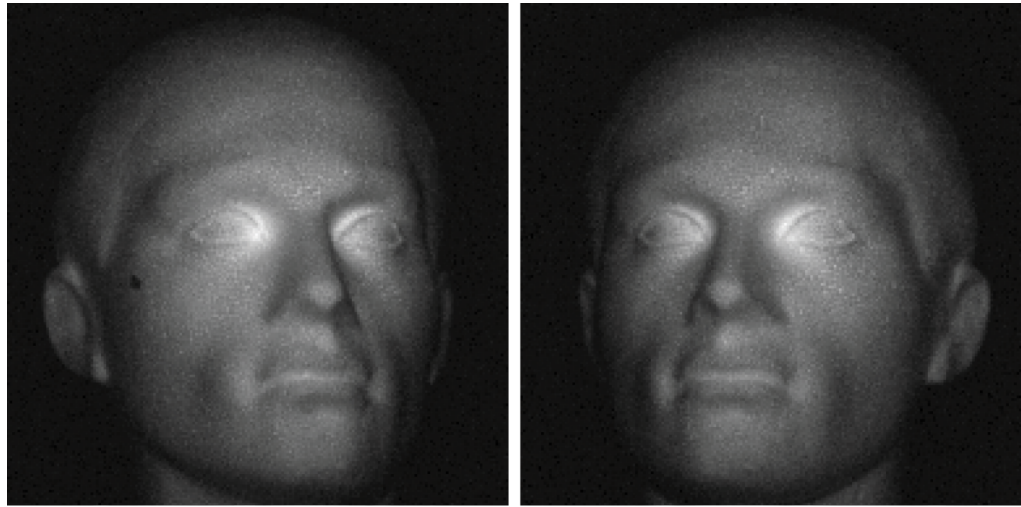


FIGURE 4.14: Validation of imaging system reciprocity. Simplified schematic of a conventional imaging system (b) and the computational imaging system (e) with the illustration of light propagation (a) and (c) respectively. In a conventional imaging system the light travels from the source to the object and the reflected light is measured on a spatially resolving detector. In our computational imaging system, a spatially resolved light pattern is projected on the object and the total reflected intensity is measured on a single-pixel detector. The images acquired from both approaches ((c) and (f)) are equivalent as shown indicated below, whereby the apparent lighting of the object is determined by the location of the non-imaging element.



(a)

(b)

FIGURE 4.15: Computational images obtained with different illumination directions: (a) from the left side of the head and (b) from the right side of the head.

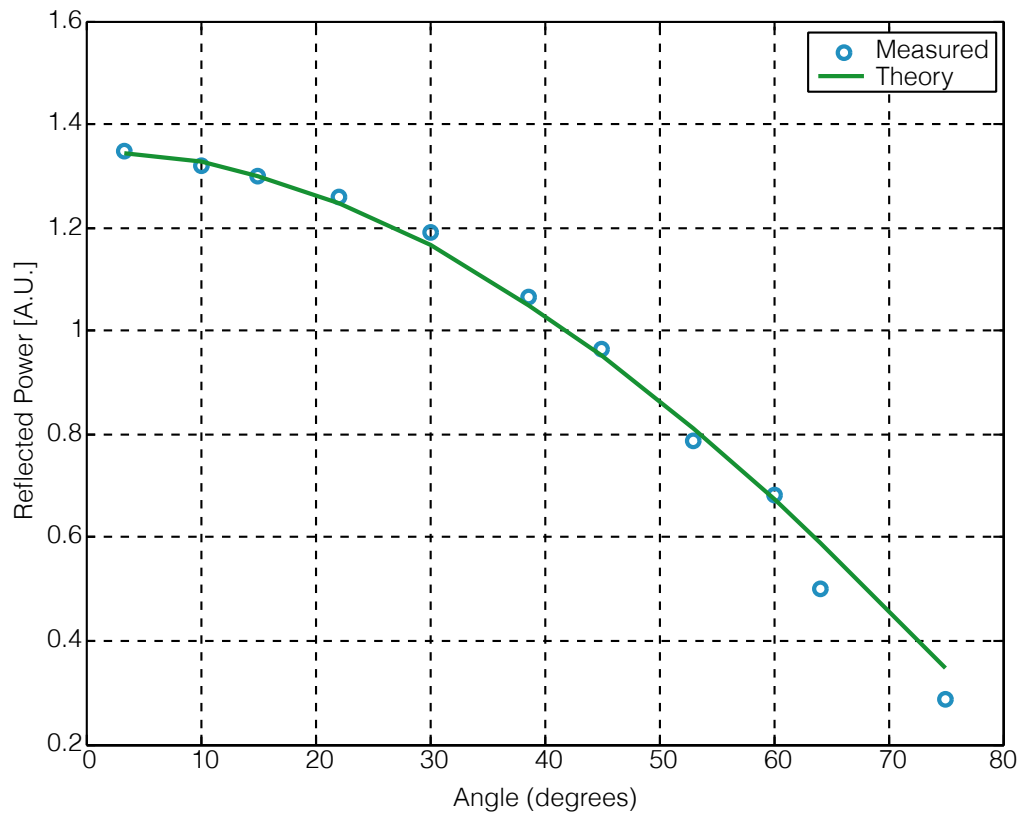


FIGURE 4.16: Measurement of Lambertian surface properties. Measured reflected power from a flat polystyrene surface (circles) and the theoretical curve representing a cosine function (solid line).

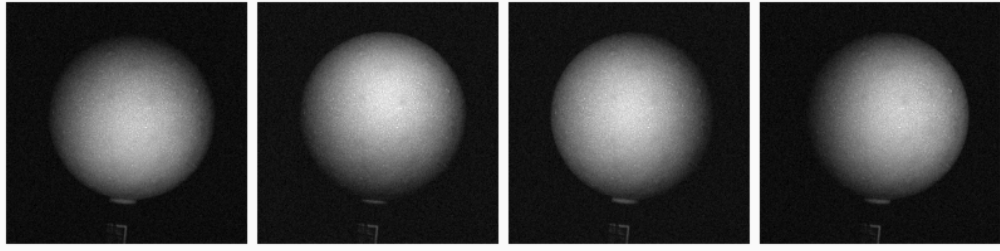


FIGURE 4.17: 2D reconstruction of a polystyrene ball .

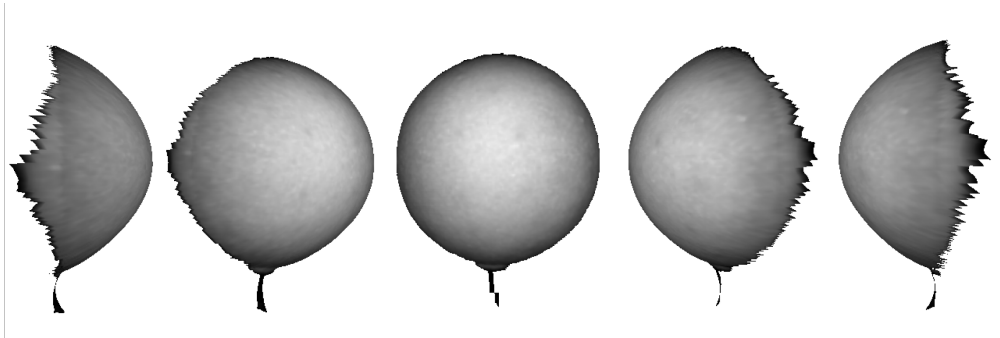


FIGURE 4.18: 3D reconstruction of a polystyrene ball .

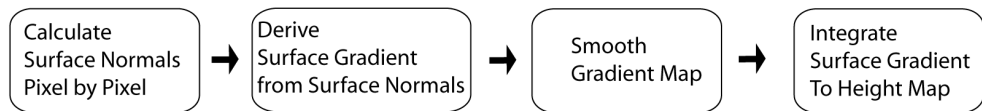
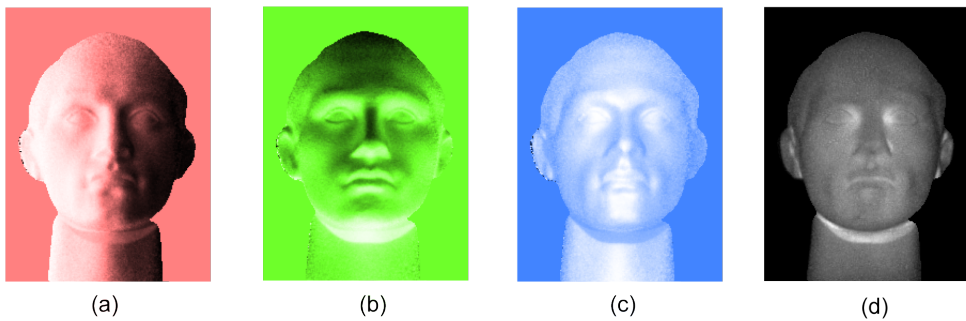


FIGURE 4.19: Process of the 3D Reconstruction.

FIGURE 4.20: Surface Normals and Reflection. (a)-(c) are surface normals in the x , y and z direction and Reflection.

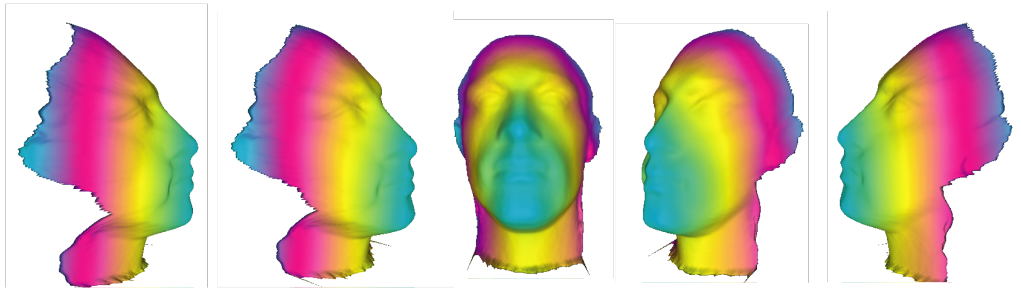


FIGURE 4.21: Rendered views of the reconstructed facial surface derived by integration of the surface normal data and overlaid with the reflectance data (movie included in supplementary material).

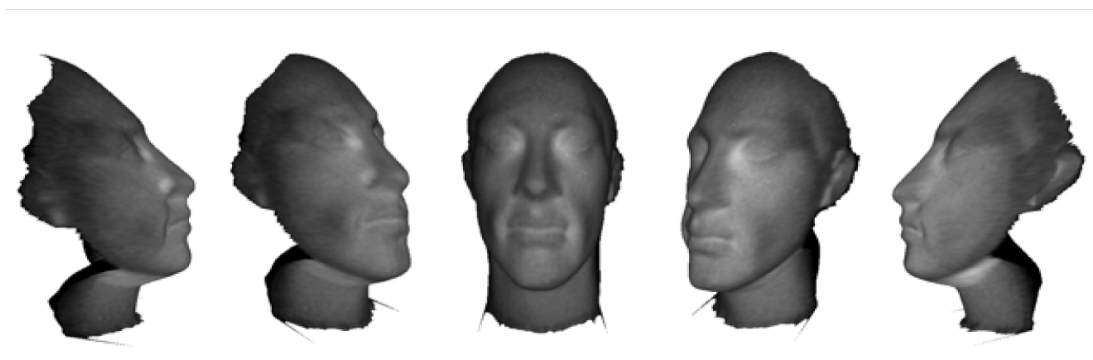


FIGURE 4.22: Rendered views of the reconstructed facial surface derived by integration of the surface normal data and overlaid with the reflectance data (movie included in supplementary material).

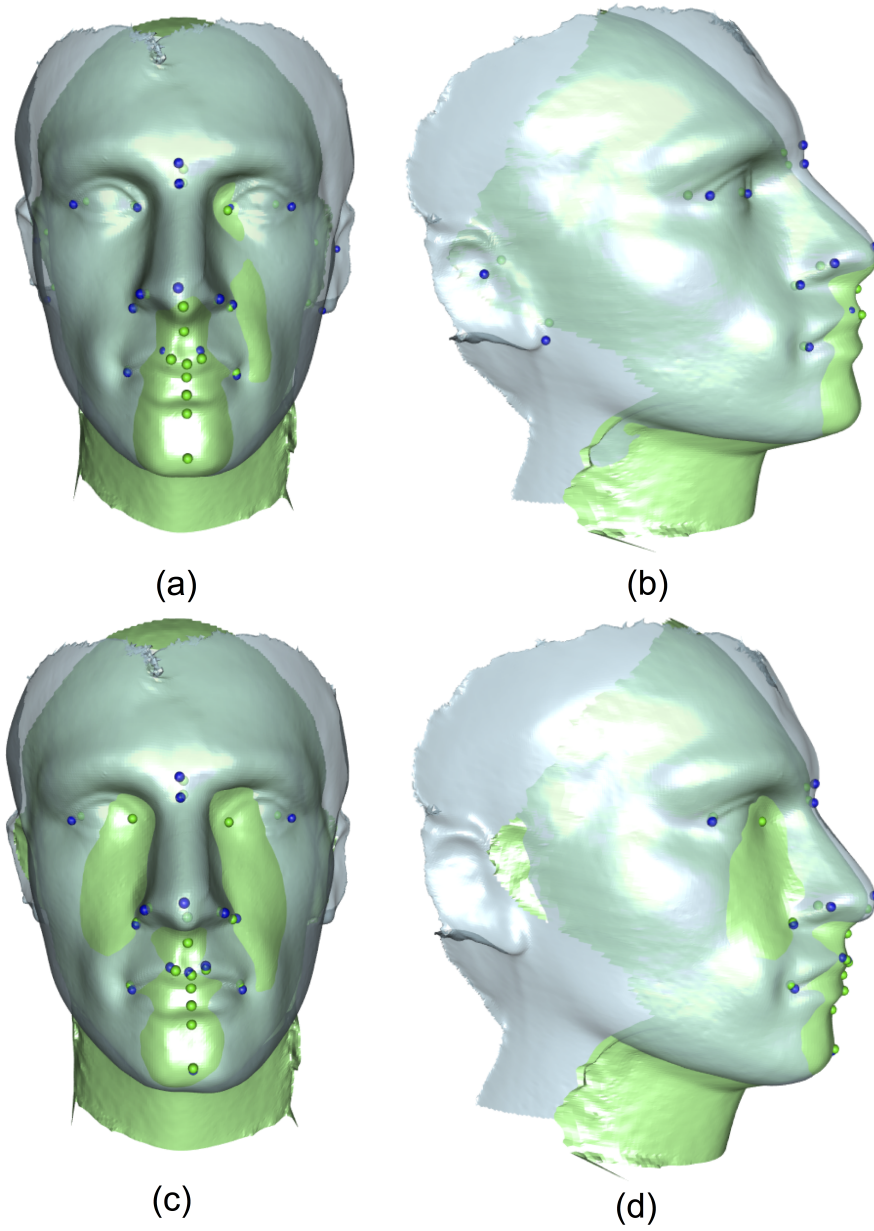


FIGURE 4.23: The matched ghost imaging (green) and stereo-photogrammetric (blue) reconstructions of the mannequin head, from frontal (a) and profile (b) viewpoints, and with anatomical landmarks (colour coded green and blue respectively) added.

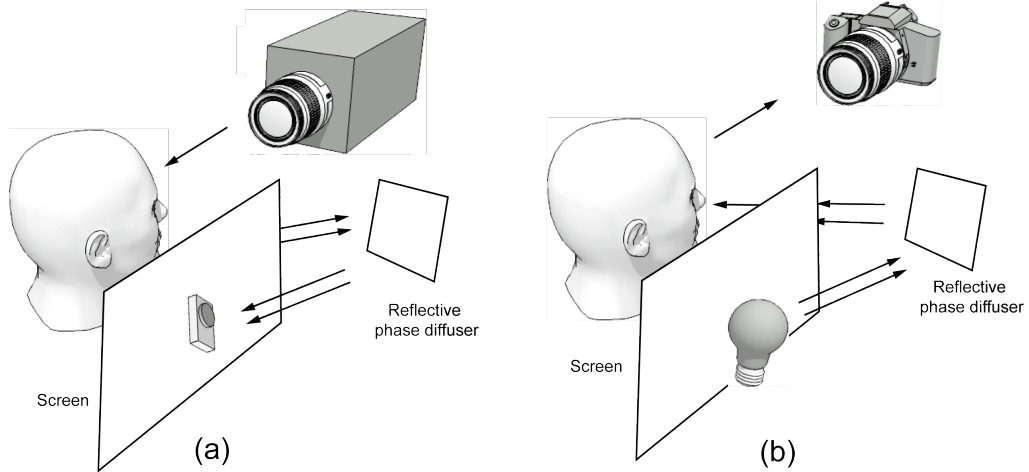


FIGURE 4.24: (a) Illustration of an imaging process of a computational imaging system with a single-pixel detector, where the single-pixel detector measures object light reflected by a wall. (b) Imaging process of a camera where the object is illuminated by light reflected by a wall.

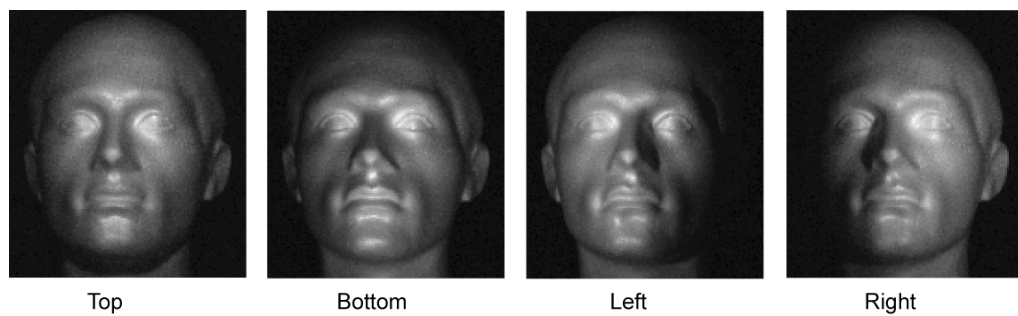


FIGURE 4.25: Images obtained from a computational imaging system with four single-pixel detectors. All four detectors are arranged in a way that light scattered from the object can not illuminate the detectors directly, but can only be reflected into the detection windows from pieces of polystyrene planes.

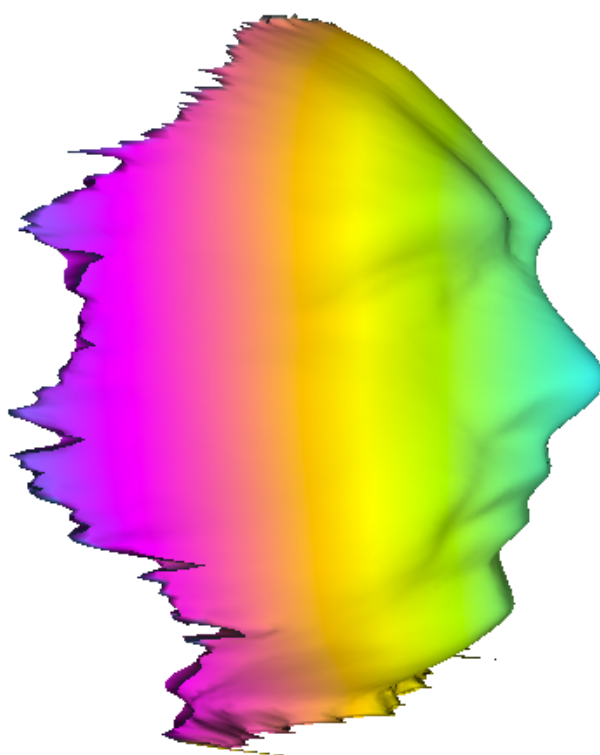


FIGURE 4.26: Side view of a 3D reconstruction using the four images shown in Fig. 4.25.

Chapter 5

Single-Pixel Real-Time Video

Any computational imaging technique with single-pixel detectors requires a number of samples to produce an image. The total acquisition time, therefore, is determined by the number of samples together with the sampling speed. Most examples of previous single-pixel computational imaging were conducted in a slow speed that it usually required a long time to obtain an image, and therefore only static object could be imaged. Some studies have aimed to improve the imaging speed, but are constrained in a single-pixel camera system using compressive algorithms [122–125]. General compressed sensing algorithms make use of some prior knowledge about the image and will itself require a non-negligible amount of computer processing time to yield an image. When concerned with real-time video applications this can therefore present a considerable challenge. In this chapter, an real-time computational video system with single-pixel detectors single-pixel based on an iterative algorithm is developed. To increase the total imaging speed, effort has been devoted to both reducing the sampling steps and increasing measurement speed.

In single-pixel imaging, sampling efficiency varies between different sampling methods, and so does the number of measurement required to form an image. The simplest sampling method is to scan the image, one pixel at a time, however the optical efficiency of this approach scales inversely with the number of pixels in the image. Another approach, as discussed in Chapter. 4, is to sample many random pixels simultaneously, which increases the signal measured with respect to the noise floor of the detector.

This many-pixel sampling method, however, is always in a low efficiency because the sampling pixels are always randomly selected. To increase the efficiency, some special basis of 2D patterns can be used. In the first section of this chapter, a sampling method using orthogonal patterns to achieve high sampling efficiency is discussed. By using orthogonal sampling, the sample efficiency is highly improved that it is able to produce an image with high visibility within the Nyquist limitation, where a sampling method using random patterns is difficult to produce a high visibility.

In addition to the sampling efficiency, measurement speed is another aspect that affects the imaging speed. Two aspects can be exploited to improve the measurement speed: the sampling apparatus and the process structure. Normally a single-pixel imaging process includes pattern projection, signal acquisition and computing process, which work together to determine the measurement speed. In a given hardware, the measurement speed changes depending on the way in which these different parts of measurement is arranged. In the second section of the chapter, the measurement speed of a computational imaging system based on a commercial digital light projector is discussed. Different measurement speed can be achieved by using different processing structures. A highest measurement speed of 660 Hz is achieved when all measurement parts run in parallel, and higher measurement speed is limited by the projection speed of the light projector. To overcome this limitation a high speed digital micro-mirror device (DMD) is employed. The DMD provides a trigger signal to enable synchronisation measurement between mask modulation and signal acquisition so that a stable parallel measurement system is guaranteed. It can generate spatial masks (or indeed structured illumination) at a rate of 22 kHz. A high speed single-pixel imaging system is developed based on the projection of a series of orthogonal patterns in this high-speed DMD. For a given sampling method, the sampling steps required for an image is proportional to the image resolution. To achieve high speed video frame, the resolution of images is chosen as 32×32 pixels, and an image reconstruction can be achieved by using 1024 (which is the Nyquist limitation) orthogonal patterns together with their inverse. This single-pixel video system can produce real-time videos in 32×32 pixels in 10 Hz. Finally an optimiser used in compressive sensing algorithms is employed to reduce the noise in the reconstruction.

5.1 Coded masking based on Hadamard patterns

It is realised that totally random patterns is not the best choice for correlation imaging, because two different patterns might contain overlap information that will reduce the correlation efficiency. To achieve maximum correlation efficiency, it is best to choose a set of orthogonal patterns. In mathematics, Hadamard matrix is such kind of matrixes that provide orthogonal structured patterns. This is earlier studied in the single-pixel camera area where compressive algorithms are used for reconstruction [126, 127]. In our computational imaging system with single-pixel detectors, Hadamard patterns can also be employed to replace totally random patterns to encode light intensity. In this section, the property of Hadamard matrix and its application in correlation imaging measurement is discussed.

5.1.1 Hadamard matrix

In mathematics, a Hadamard matrix [128] is a square matrix whose elements are either +1 or −1 and whose rows are mutually orthogonal [129–131]. In other words,

$$HH' = H'H = HH^T = nI_n, \quad (5.1)$$

here H' and H^T are the inverse and transpose of H , and n is the order of the Hadamard matrix H . Therefore the transpose of a Hadamard matrix is still a Hadamard matrix. In a Hadamard matrix, every two different rows have same elements in exactly half of their columns and opposite elements in the remaining columns. If any two rows are multiplied element by element, the sum of all the multiplication is zero. In other words, every two different rows in a Hadamard matrix can be represented by two vectors those are perpendicular to each other in the vector space. Consequently all these properties hold for columns as well as rows.

The order of a Hadamard matrix n could be 1, 2, or $4i$ where i is a positive integer. Here only Hadamard with an order of 2^n is discussed, which can be expressed as

$$H_2 = \begin{bmatrix} 1 & 1 \\ 1 & -1 \end{bmatrix}.$$

Higher order Hadamard matrices can be obtained as

$$H_{2^n} = \begin{bmatrix} H_{2^{n-1}} & H_{2^{n-1}} \\ H_{2^{n-1}} & -H_{2^{n-1}} \end{bmatrix} = H_2 \otimes H_{2^{n-1}},$$

here \otimes stands for Kronecker product.

5.1.2 Hadamard patterns in iterative correlation imaging

To utilise Hadamard derived patterns in correlation imaging, we choose a Hadamard matrix in the order of 2^{2k} , and then reshape every row (or column) into a $2^k \times 2^k$ 2D array. For simplicity, such a pattern derived from a row of a Hadamard matrix is referred as a Hadamard derived pattern in this thesis. Therefore a Hadamard matrix in the order of 2^{2k} can be transferred into a complete set of k $2^k \times 2^k$ Hadamard derived patterns in 2D. These k 2^k Hadamard derived patterns are used for structured illumination. In our first experiment here, a 4096×4096 Hadamard matrix is used to generate 4096 of 64×64 2D Hadamard derived patterns to modulate the light source. As the 4096×4096 pattern is too big to show here, a 64×64 Hadamard and one of the 8×8 Hadamard derived pattern is shown for illustration. Fig. 5.1 (a) shows the 64×64 Hadamard matrix, and the derived 2D pattern from the 14th row is shown as Fig. 5.1 (b).

The 4096 2D Hadamard derived patterns are used in iterative GI reconstruction according to Eq. 4.1. It should be noticed that Hadamard patterns contains $+1$ and -1 elements, while DLP could only project black/white (0/1) pixels. However, by using differential projection method introduced in Chapter 4, the effective projection patterns are in ± 1 rather than 0s and 1s.

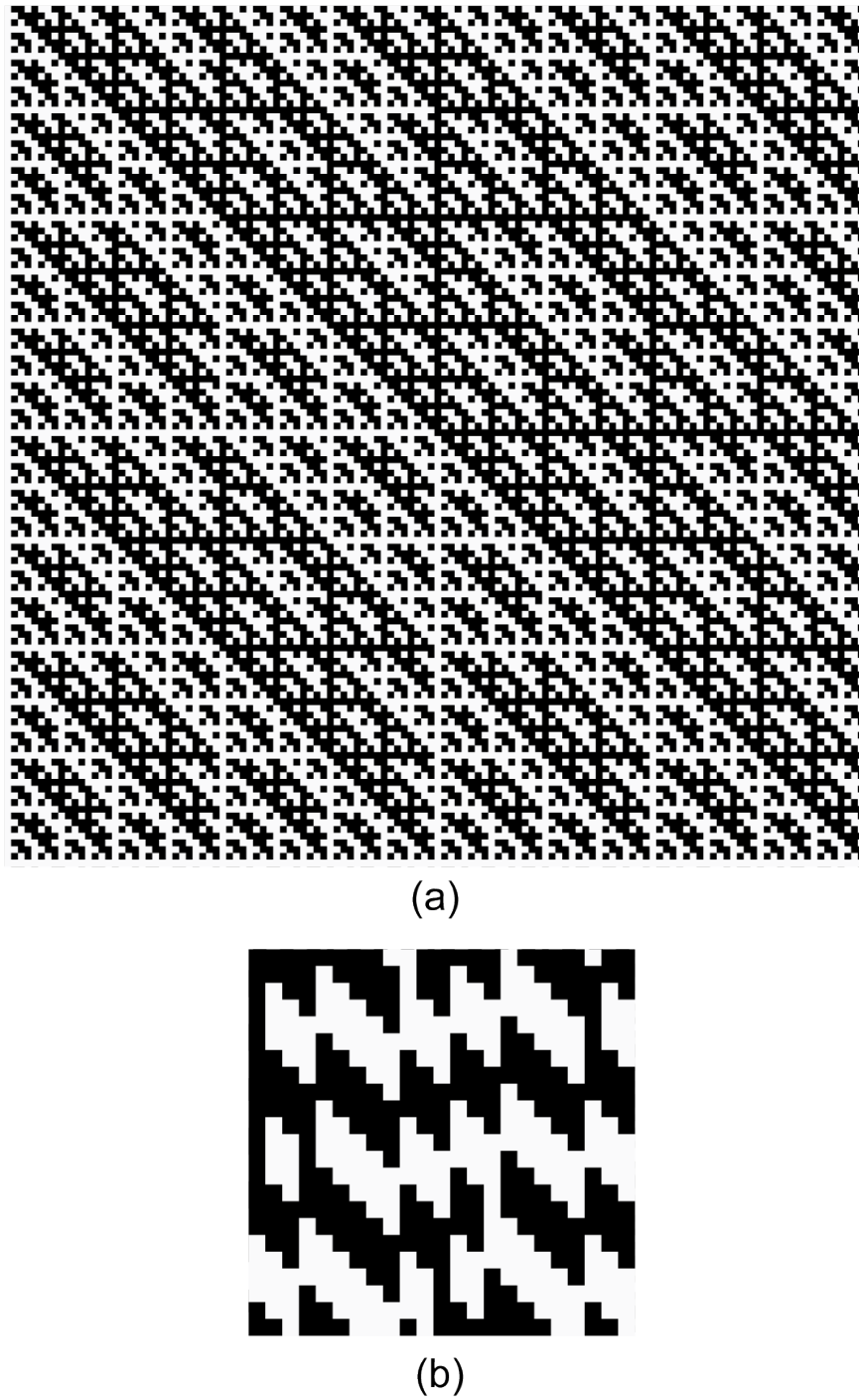


FIGURE 5.1: (a) A 64×64 Hadamard matrix and (b) the derived 2D pattern from the 14th row.

Results from a TGI correlation algorithm using Hadamard derived patterns are shown in Fig. 5.2. Compared with TGI using random patterns after the same iteration (Fig. 5.3), the final reconstruction quality is significantly improved. The reason why Hadamard

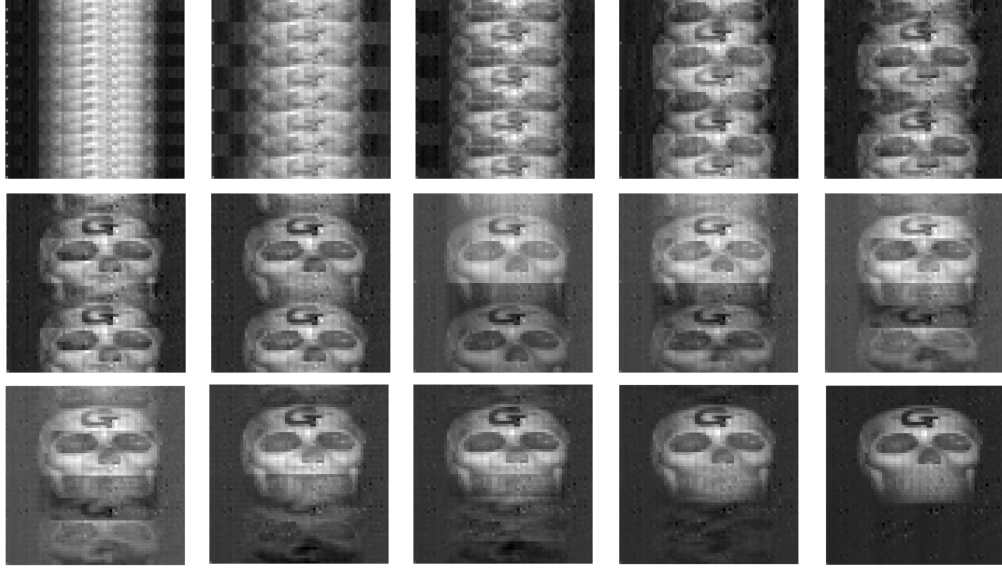


FIGURE 5.2: Reconstruction of a toy skull from a full set of Hadamard derived patterns. The Hadamard derived patterns are in 64×64 derived from a 4096×4096 Hadamard matrix. From top-left to bottom-right are results after 300, 600, 900, 1200, 1500, 1800, 2100, 2400, 2700, 3000, 3300, 3600, 3800, 4000 and 4096 iterations.

derived patterns work much better for correlation imaging is that they are orthogonal to each other. Therefore the correlation contains no overlap between each other and the reconstruction efficiency is much higher. On the other hand, the mid results contain overlaps before the whole set of patterns are completed employed in the correlation function (Eq. 4.1). This is determined by the structure property of the Hadamard matrix, especially by some 2D Hadamard derived patterns contains low resolution and period structures. The overlap disappears when the whole set of correlation is done because of the completeness of the patterns.

The differential signals from the whole set of Hadamard derived patterns for the reconstructions in Fig. 5.2 are shown in Fig. 5.4 (a). Some of the patterns have significant high signals than the others, indicating that they are much more weighted and may affect the measurement precision of the others with small values. These nonuniform spectrum distribution can be adjusted by using randomising the Hadamard subarrays [132, 133], which can be achieved according to

$$h_{rand} = h \oplus R \quad (5.2)$$

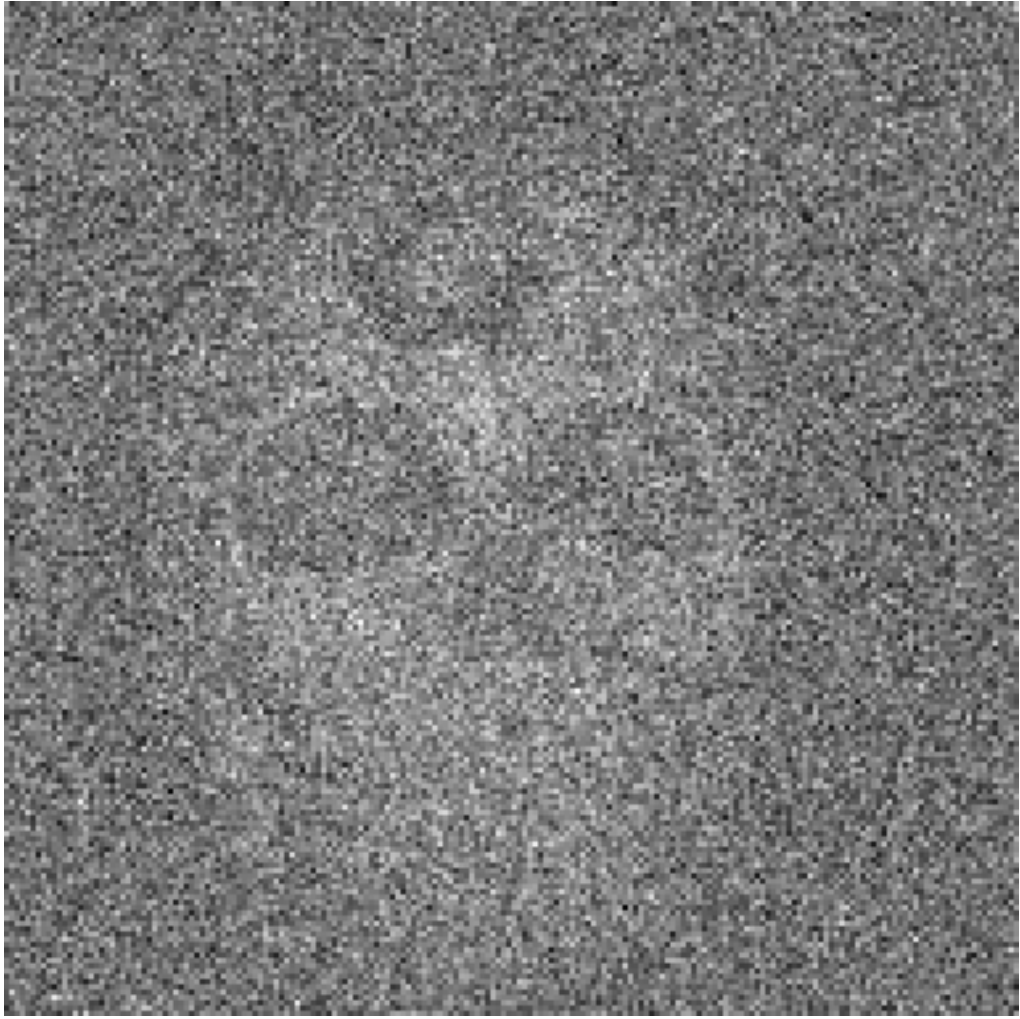


FIGURE 5.3: TGI reconstruction of a toy skull using 4096 random binary patterns.

Here h is a 64×64 Hadamard derived pattern, R is a random array in the same dimension, with half of its elements being $+1$ and the other half -1 . \oplus indicates the boolean operation *exclusiveor*, and h_{rand} is the randomised array. The *exclusiveor* operation follows the rule as: $\pm 1 \oplus \mp 1 = +1$, $\pm 1 \oplus \pm 1 = -1$. A comparison of a original Hadamard derived pattern and its randomised version is shown in Fig. 5.5. The same randomisation is applied for all the 4096 Hadamard subarrays using the same random pattern. The randomised patterns are still orthogonal to each other, but the randomisation spread the spectrum distribution of the Hadamard derived patterns more uniform and therefore all overlap intensities are in the same level, as shown in Fig. 5.4 (b). The consequential reconstruction process is shown in Fig. 5.6. The final reconstruction after the whole set of correlation keeps the same as in Fig. 5.2, which is obtained using Hadamard derived

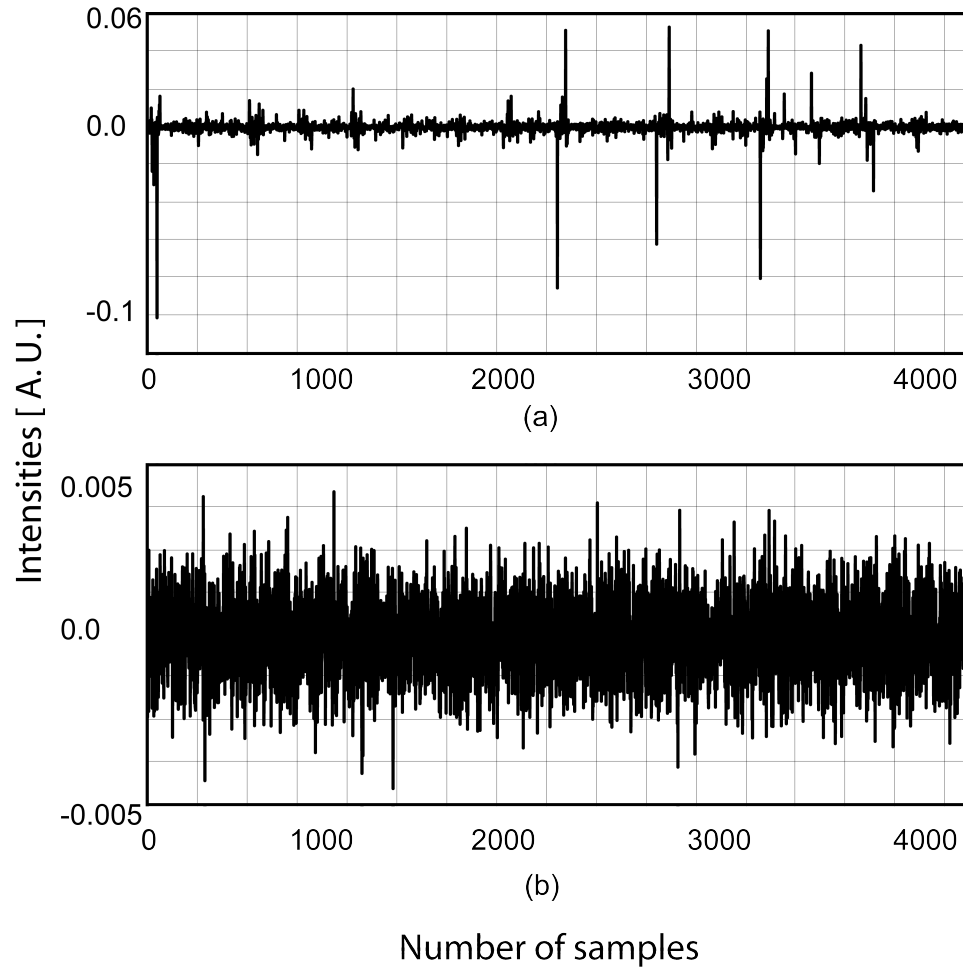


FIGURE 5.4: (a) Signal distribution of the 4096 Hadamard derived patterns from the reconstruction shown in Fig. 5.2, and (b) signals of the randomised Hadamard derived patterns from the reconstruction shown in Fig. 5.6.

patterns without randomisation.

5.2 Computational imaging using a commercial light projector

In this section, the measurement speed of the computational imaging system described in Chapter 4 is discussed. As described in Chapter 4, the system consists a digital light project (DLP) (Texas Instruments light commander), several single-pixel detectors, an analog to digital converter and a computer. The DLP runs in a typical frame rate of

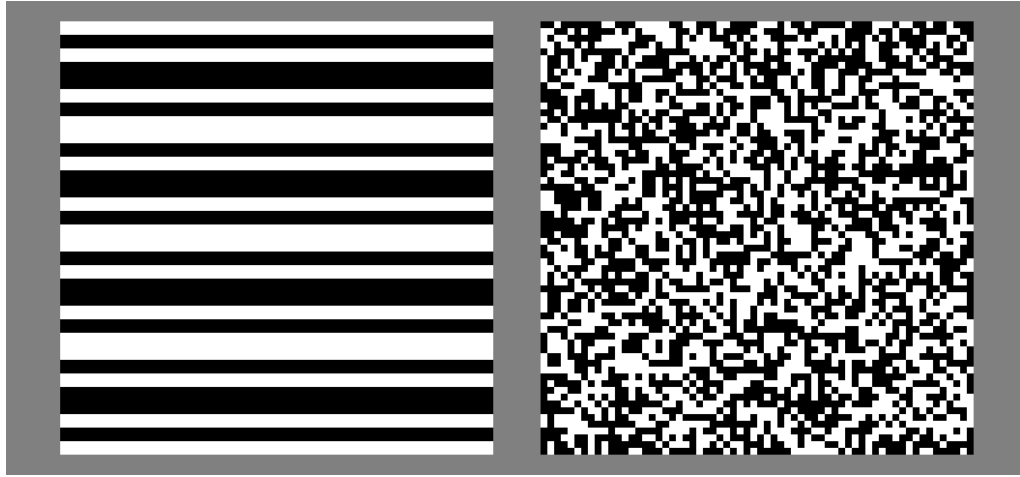


FIGURE 5.5: A Hadamard derived pattern derived from a row of a 4096×4096 Hadamard matrix (left) and its randomised format (right).

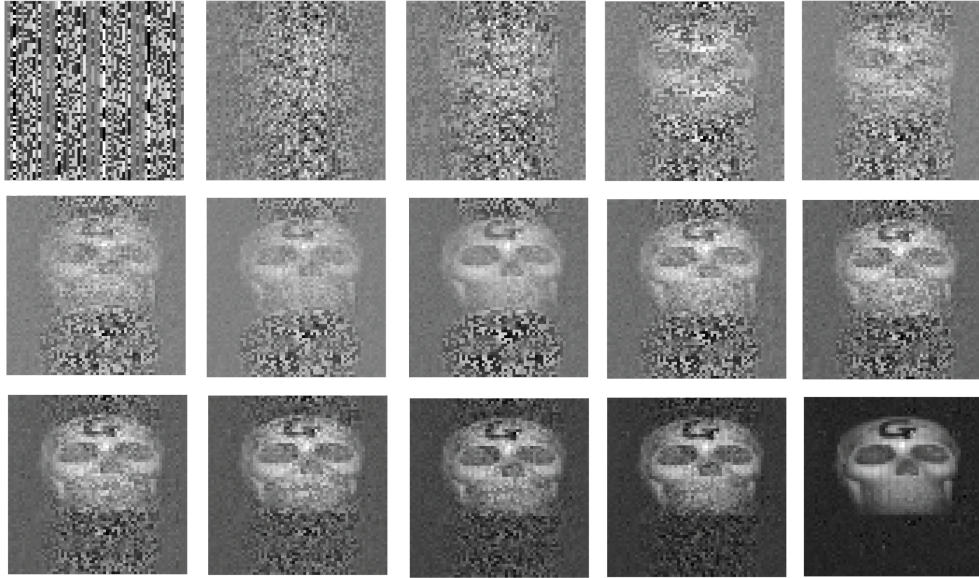
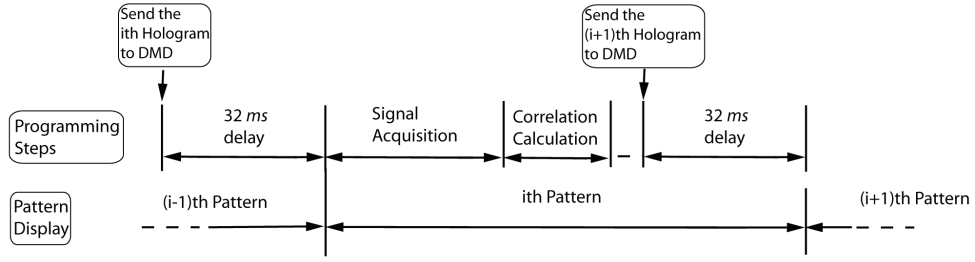


FIGURE 5.6: Reconstructions from a whole set of randomised Hadamard derived patterns. The randomised Hadamard derived patterns are in 64×64 pixels derived from a 4096×4096 Hadamard matrix. From top-left to bottom-right are results from after 300 up to 4096 iterations, with an increasing step of 300 iterations between any two neighbouring ones.

60 Hz, and in each frame there is further modulation to provide 24 bit colour depth, resulting in a total pattern projection rate of ~ 1440 Hz. Acquisition of back-scattered light is performed using a Thorlabs PDA100-EC silicon photodiode and a National Instruments 6221 analogue-to-digital converter, with a maximum sampling rate of 250kS/s. The computer processing is performed using the Labview software package on an intel Xeon computer processing unit. The overall frame rate of the system is limited by

FIGURE 5.7: Sequential experiment procedure of GI using a *Light Commander*.

the speed of spatial light modulation, the acquisition of photodetector signals and the computer processing. Depending on how these measurement portions are arranged, the system can run in different frame rates. A basic sequential method where different measurement portions run in series operates the system in 10 Hz. Higher frame rate can be achieved within the system using parallel measurement.

5.2.1 Sequential processing

In the computational imaging system with single-pixel detectors in Chapter 4, light is modulated by a DMD chip controlled by hologram in a frame rate of 60 Hz. The photodetector is set at a sampling rate of 57.6 kHz. For each projection pattern, it takes 34.7ms to obtain 2000 samples. In our system, there is an approximate 30ms delay for a light pattern to get displayed after a hologram is sent to the DLP. To make sure that a single-pixel detector acquires the right signals from the corresponding projection, a 32ms wait is added between the hologram display and the signal acquisition in the control software (Fig .5.7). Besides, the random hologram generation and iterative reconstruction calculation also take a certain period of time. All this procedure together determines the length of each iteration. The measurement speed is around 10 Hz.

5.2.2 A 110 Hz system by exploiting bit-plane display

A much faster system can be achieved by using bit-plane display in the same experiment setup. As discussed in Chapter 4, each frame of a DLP display contains 24 bit planes, which can be coded to project positive and negative patterns. It benefits the system

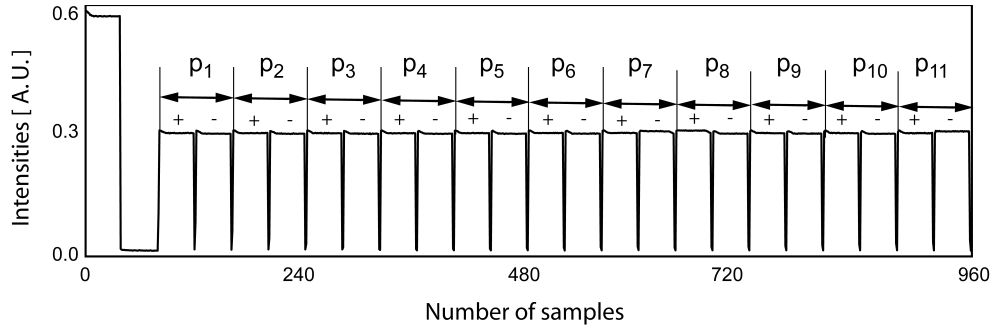


FIGURE 5.8: Signals in a frame which are associated to 11 different light patterns ($p_1 - p_{11}$). The two bit planes on the left end are used as triggers.

with differential signals which are free from low frequency background noise. An extension of this method can help increase the measurement speed. As each bit plane can be associated to a binary pattern, 24 different patterns can be coded into one frame. In order to achieve differential signal measurement, two bit planes are distributed to one pattern. Therefore 11 different patterns can be coded into one frame, and the other two bit planes are used as triggers for synchronisation measurement (Fig. 5.8). Once a frame is displayed, there are 11 different patterns get displayed consequently. Signal acquisition is performed in the same way as shown in Fig. 5.7. To ensure a good SNR of the acquired signals, the $32ms$ delay is used. The only difference is that now every measurement is for 11 different patterns rather than only one. The signals are then chopped according to Fig. 4.8 and correlated to their corresponding patterns. As each frame contains computation and correlation calculation of 11 patterns, the actual reconstruction speed is about 110 Hz.

5.2.3 A 660 Hz GI system

In all the measurement methods discussed above, the display of light patterns and signal acquisition are performed in series. Signal acquisition does not start before the pattern is displayed and detected by the detector. And the display for the next pattern starts after the last signal acquisition is finished. In contrast to a series measurement, a parallel performance of the pattern display, signal acquisition as well as correlation calculation could take better use of the computing power and boost the imaging reconstruction speed.

To achieve parallel measurement, some Labview function called “Queue Operation” is employed in the controlling program. A “Queue” in Labview is used to communicate data between different sections or even other VIs. It is a similar function as “stack” in C programming. To start, a queue is built up with its optional name, data type and size. A reference is distributed to access the queue since it is created. Data can be added to the front or end of the queue. Also they can be read and deleted from the queue. In our parallel GI program, we build up two queues. One is to store light patterns and the other to store measured signals. Once a pattern gets displayed, it will be added to the end of the queue. Meanwhile acquired bucket signals are also added to their queue in order. Patterns and their corresponding signals are released from the queue for correlation reconstruction. For the reconstruction, is important to match a pattern with its correct signals. As there is no inherent trigger signals from the DLP, to ensure synchronisation measurement, some trigger signals are created using light pattern display. In the beginning of the measurement, a all black pattern is displayed for a period of time so that we can measure the background noise level. Right after that, a trigger frame with alternative all black and all white pixels are displayed. Compared to the background light, these trigger signals have a high level fluctuation. Therefore by measuring the root mean square (RMS) of the obtained signals, we can recognise the starting point of the trigger. Followed the trigger frame there are patterns projected for reconstruction. The same trigger frame is repeated every 100 frames to maintain the measurement synchronisation. As all parts of the measurement are running in parallel, the measurement speed is determined by the display speed. As the DLP runs in 60 Hz, and each frame contains 11 different patterns, the total reconstruction rate is around 600 Hz.

A problem of the parallel system is that the trigger is effected by the environment. Any small fluctuation of the background light will interfere the synchronisation of the program, therefore the parallel measurement is very unstable.

In summary, the reconstruction speed of GI system is effected by a few factors: the hologram display speed, signal acquisition speed as well as computation speed (which includes hologram generation and correlation calculation). For a given system setup,

the highest reconstruction speed is achieved when all different parts of the experiment operate in parallel. In fact, the time spent on hologram generation and correlation calculation is trivial, and the acquisition speed is relative fast. In our single-pixel computational imaging system, the bandwidth of the Thorlabs PDA100A-EC Si Transimpedance Amplified photodetector is from DC to 2.4 MHz. Therefore, the speed of a parallel computational imaging system is mainly limited by the projection speed of the DMD. On the other hand, in order to achieve a stable parallel measurement system and guarantee synchronisation measurement, some stable trigger signals have to be employed.

5.3 Real-time video from a computational imaging system with single-pixel detectors

In this section, a high speed computational imaging system with single-pixel is introduced. The system displays Hadamard derived patterns in a high-speed DMD. With the assistance of the trigger signals from the DMD controlling circuit, the signal acquisition is able to run in parallel and synchronise to the light pattern display. As the pattern display, signal acquisition as well as reconstruction calculation all run in parallel, the system can operate in a high speed which is determined by the speed of DMD display.

5.3.1 Experimental setup

The experiment setup here is illustrated as Fig. 5.9. The system contains a DMD system and three photodetectors. A white light source is used to illuminate the DMD chip and encoded into binary light fields (0s and 1s). The structured light patterns are then projected by a lens onto the object. Three photodetectors for red, green and blue (RGB) light detection are put together to receive light scattered by the object. A major change in this system compared to the system shown in Fig. 4.3 is that the Light Commander is replaced by a high speed DMD called Accessory Light modulator Package (ALP) 4.2 from Vialux. It contains a DMD chip with 1024×768 pixels and a control circuit connected to computer via a USB cable. The application programming interface is written as a dynamic-link library (DLL) file which provides a convenient interference

between of control software (Labview) and ALP driver. Patterns are first loaded from the controlling software to the ALP board RAM in sequence. The bit depth of the displayed patterns can be chosen from the following values: 1, 2, 3, 4, 5, 6, 7, 8. And the display time can also be adjusted manually through the control software. In our experiment the bit plane depth is chosen to be 1 so that the display can run in the highest speed. The display time for each pattern is set to be $45\mu s$ as the minimum. Therefore the maximum display speed of the DMD is 22 kHz. Besides the high speed projection, another important advantage of the ALP is that it provides synchronisation trigger signals in reference to its display. That is, when one pattern gets displayed, there is a trigger signal released from DMD control circuit. This trigger signals is connected to the DAQ input to trigger a series of data acquisition. Signals are acquired after every trigger signal, and the sample numbers are determined by the display time and sampling rate. The DAQ used here is a National Instrument portable USB DAQ (NI USB-6221/16) with a maximum acquisition rate of 250 kHz for all channels. As there are three channels employed, sampling rate for each channel is set to 83 kHz. Given that each pattern is displayed for $45\mu s$, there are 3 samples acquired for each pattern.

5.3.2 Single-pixel computational video

Based on the computational imaging system described above, Hadamard derived patterns are displayed for a video frame correlation imaging reconstruction. The Hadamard derived patterns are derived from a 1024×1024 Hadamard matrix. The differential display method is also employed here. Therefore a full set of reconstruction contains 1024 iterations, and in each iteration a 32×32 Hadamard derived pattern is displayed followed with its inverse, and a reconstructed image needs 2048 display frame and the corresponding signal acquisitions. The DMD system runs in its fastest speed in 22 kHz, so it takes about 0.1s for a complete reconstruction. The displayed images are updated after a full set of reconstruction is finished, so the video frame rate is 10 Hz, while the correlation measurement frame rate is 10 kHz. Fig. 5.10 shows 40 video frames for 4s. Each frame is built up from a full set of 1024 Hadamard derived patterns in a resolution of 32×32 pixels. The three channels for RGB colours are independently reconstructed

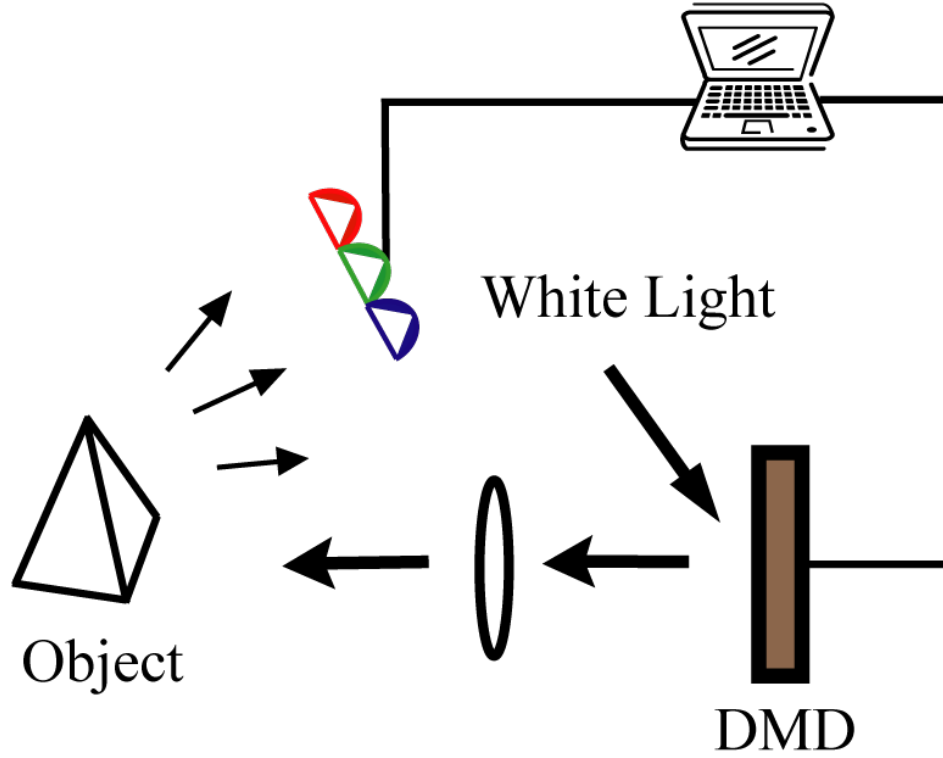


FIGURE 5.9: Illustration of a fast single-pixel computational imaging system. Uniform light is directed to the DMD, modulated into binary patterns and then displayed onto the object by a projection lens. Reflected signals are collected by three single-pixel detectors for red, green and blue light and then sent to a computer.

in parallel, and then combined to form a colour image under the simple assumption that the RGB colours weight equally to each other. To assure a correct colour balance, all the three detectors are switched on the same gain level. Also a white target is imaged to test the colour balance, which is verified when the image of the white object is white.

5.4 Real-time video from a single-pixel camera

Computational imaging system with single-pixel detectors employs coded light patterns for illumination, therefore background light behaves as noise in correlation imaging reconstruction. As an alternative way of computational imaging with single-pixel detectors, a single pixel camera uses the ambient light as light source. Instead of modulating

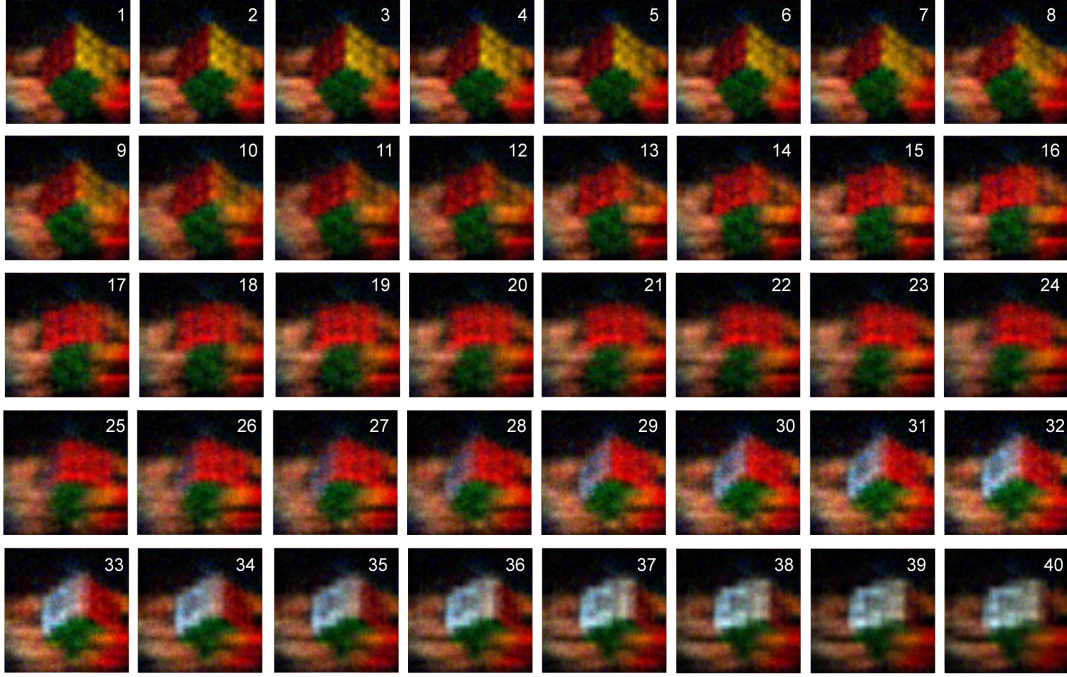


FIGURE 5.10: Video frames from a 10 Hz single-pixel computational imaging system in 4s. Each image is obtained from the correlation of 1024 Hadamard derived patterns in 32×32 pixels, which is finished in 0.1 Hz. The scene is about a Rubik's cube rotated by hands.

the light with SLM before illumination, single pixel camera projects the object image illuminated under ambient light onto a DMD chip and modulate the object image with random patterns before detected by a bucket detector. Fig.5.11 shows such a single pixel camera system adjusted from the single-pixel computational imaging system shown in Fig. 5.9. Compared to the computational imaging system, the white light source is removed and replaced by a detecting package. Object illuminated by the ambient light is imaged onto the DMD chip and then sent to a composite dichroic beamsplitter (X-Cube). The dichroic beam splitter is used to spectrally direct red, green and blue light towards different outputs and allow subsequent measurement on three unfiltered single-pixel photodetectors. The single-pixel detectors are Thorlabs amplified photomultipliers (PMM02). PMM02 is an photomultiplier tube designed for detection of light from DC to 20 kHz. A buffered output drives a 50Ω impedance up to 5V. It also contains a control (voltage from 0 to 1.8V) to adjust the gain level. The spectrum range is 280 – 850nm.

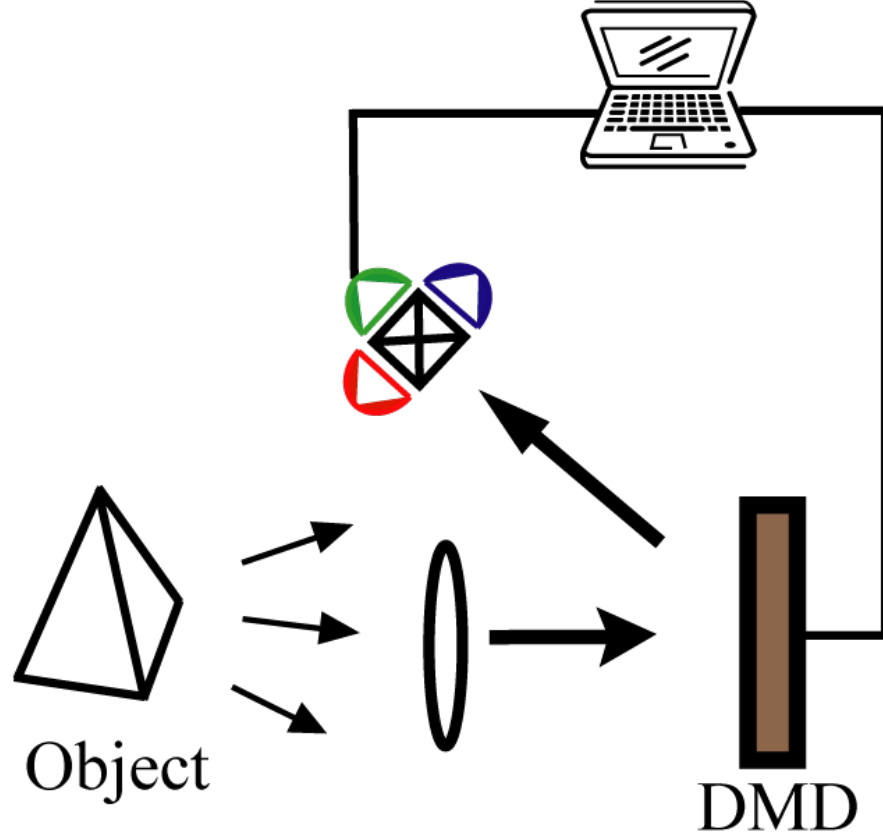


FIGURE 5.11: Illustration of a fast single pixel camera. Object under the ambient light illumination is imaged onto the DMD. Light is then split by a composite dichroic beamsplitter (X-Cube) into three channels for red green and blue light, each being detected by a unfiltered single-pixel detector and sent to a computer.

PMM02 is designed with high sensitivity and low dark current, which is ideal for detection of low level light.

Figure 5.12 shows 40 frame images for 4s. Each image is reconstructed from 1024 32×32 Hadamard derived patterns. The three photomultipliers are adjusted into the same gain level so that the system has the same response to different colours. Compared with Fig.5.10, the image quality is much better which is mainly attributed to the utilisation of the photomultipliers.

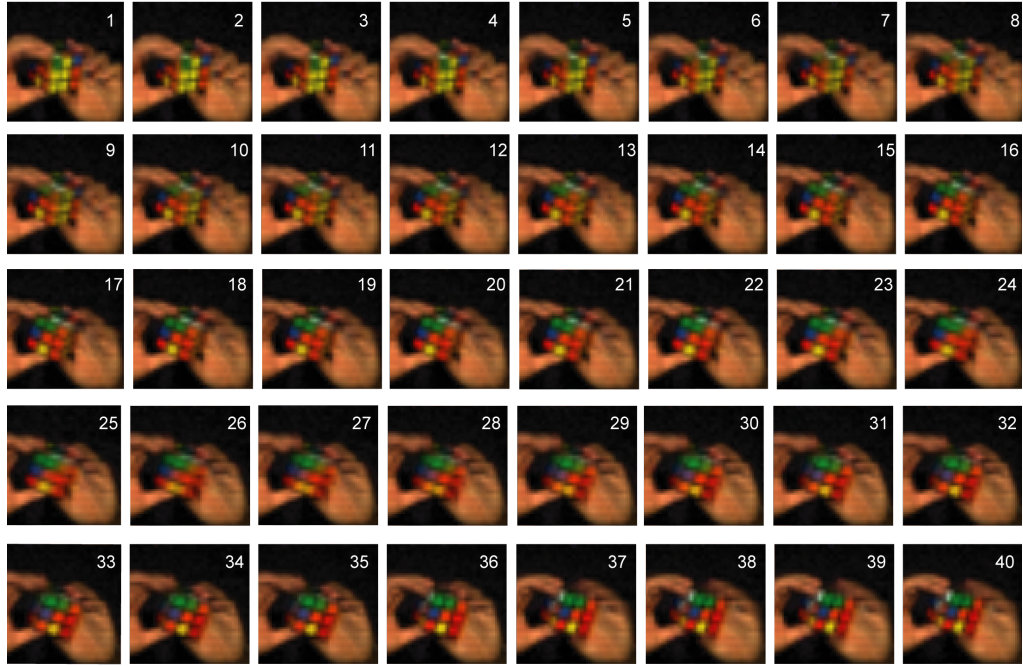


FIGURE 5.12: Video frames from a 10Hz single pixel camera in 4s. Each image is obtained from the correlation of 1024 Hadamard derived patterns in 32×32 pixels, which is finished in 0.1 Hz. The scene is about a Rubik's cube rotated by hands.

5.5 Noise reduction using an optimiser

In a video frame imaging system, signal acquisition for a certain pattern has to be finished due to the short period of time. In the two fast single pixel imaging systems described in Section 5.3 and 5.4, each pattern gets 3 signals for the positive pattern and 3 for its inverse pattern. A less number of samples means a higher noise level in reconstruction. To improve the reconstruction by reducing the noise level, an optimiser is employed here with the use of the light patterns and their corresponding intensity signals.

In computational imaging using single-pixel detectors or single-pixel camera, there are two kinds of reconstruction algorithms, iterative algorithms and compressive algorithms. When the patterns and signals are fixed, the results from a given iterative algorithm is fixed. Compressive algorithms, however, behaves differently that better results could be obtained if more calculation time is spent. In compressive sensing, an optimiser is

used for the reconstruction with the assumption of image sparsity. In fact, most images, $O_{x,y}$ are sparse, not in their intensity values but in their spatial frequencies. This latter algorithms using an optimiser can not only build an image from scratch but also be employed to reduce the noise of an achieved reconstruction. Such an optimisation algorithm utilises the measured signals and patterns within a forward-model. The optimisation algorithm suppresses noise by maximising the image sparsity within the statistical bounds of the fit to the data. Optimising for sparsity of the spatial frequencies is similar to a minimisation of the image derivatives, the latter being far quicker to compute and hence more applicable to a real-time computational video system. In this experiment, optimisation is applied to each of the colour plane images separately, based on minimisation of its spatial curvature and its frame-to-frame temporal derivative. The n^{th} image of the sequence is obtained by minimisation of its cost function, C_n , given by

$$C_n = \frac{1}{N} \sum_{j=1}^N \left(\frac{\sum_{i=1}^N A_{ij} O_{j,n} - S_{j,n}}{\sigma_s} \right)^2 + \lambda_1 \left(\sum \left| \frac{d_2 O_n}{dx^2} \right| + \left| \frac{d^2 O_n}{dy^2} \right| \right) + \lambda_2 \sum_{j=1}^N |O_{i,n} - O_{i,n-1}|, \quad (5.3)$$

here σ_s is the standard deviation of the noise associated with the measurement of $S_{j,n}$ and O_n is the image expressed in 2D form. The first term corresponds to a minimisation of χ^2/N of the image with respect to the measured data, the second term represents a minimisation of the total image curvature and the third term corresponds to a minimisation of the difference between the current and previous image. Values of λ_1 and λ_2 are picked empirically to ensure that, once optimised, $\chi^2/N \simeq 1$. Utilising an image resolution of 32×32 pixels, our optimisation algorithm runs approximately 5 times faster than the full frame acquisition time, which is able to suppress the noise

A comparison between TGI before and after the optimisation is shown in Fig. 5.13. The object is a moving toy robot, and the scene is recorded in 32×32 pixels. Fig. 5.13 (a) shows a series of scenery obtained from TGI using 1024 Hadamard derived patterns in 32×32 pixels. Fig. 5.13 (b) are the corresponding optimised TGI results. Though TGI without optimisation gives images in reasonable SNR, the optimisation improves the results even better. These improvement is more obvious for TGI obtained using random patterns. Fig. 5.14.(a) shows the same scenery obtained from TGI using random

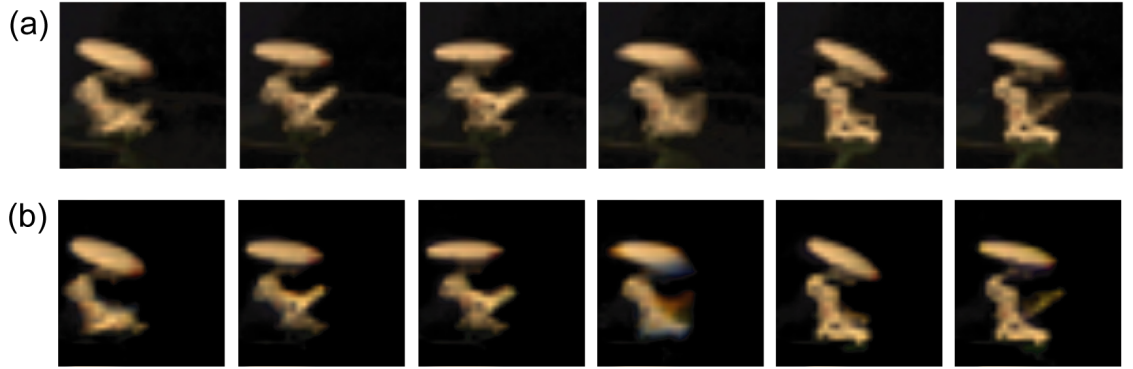


FIGURE 5.13: Video frames of a moving toy robot from TGI algorithm (a) without optimisation and (b) with optimisation. Each image is obtained using correlation of 1024 32×32 Hadamard derived patterns.

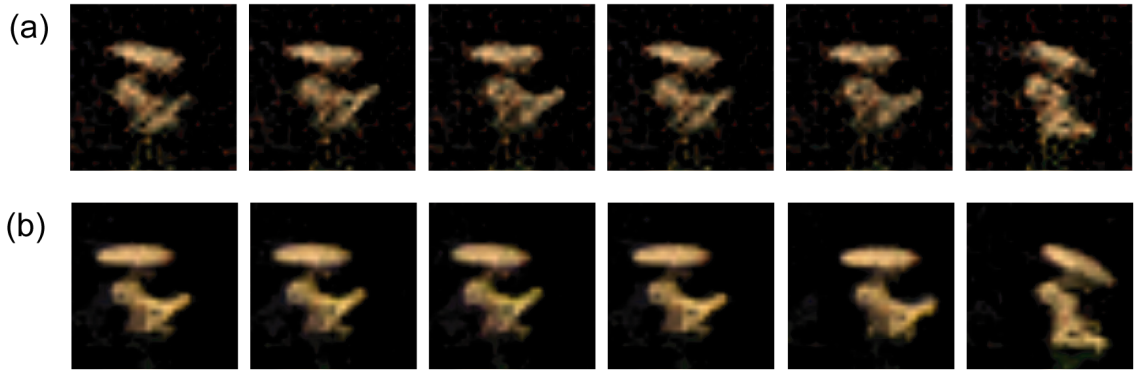


FIGURE 5.14: Video frames of a moving toy robot from TGI algorithm (a) without optimisation and (b) with optimisation. Each image is obtained using correlation of 1024 32×32 random binary patterns.

patterns. Images reconstructed from random patterns are much more noisy compared to those obtained using Hadamard derived patterns shown in Fig.5.13. (a). However, the optimiser can efficiently removes the noise and provide a much better image (Fig. 5.14.(b)).

All videos discussed are recorded in 32×32 pixels. Reconstruction in higher resolution requires much longer time, and the video frame rate will be much slower. For a 64×64 image, the time for the same iteration number is increased by 4 times than that for a 32×32 image. Therefore the video frame rate for 64×64 images is around 2.6 Hz. An approach to increase the frame rate is to abandon the differential signal method, which means the frame rate can be increased to 5 Hz for a 64×64 resolution video.

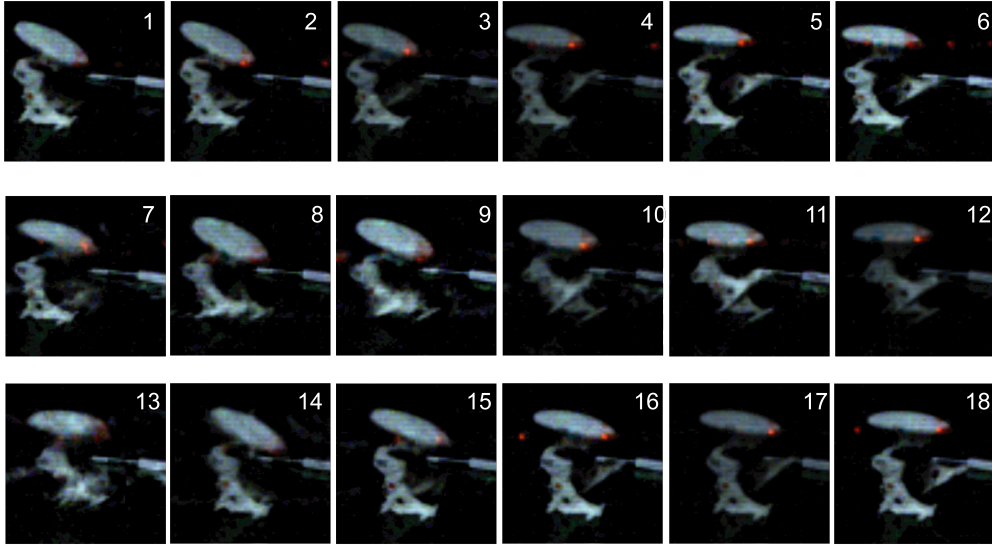


FIGURE 5.15: Video frames of a moving toy robot from TGI algorithm and after optimisation. Each image is obtained using correlation of 4096 64×64 Hadamard derived patterns.

5.6 Conclusion

In this section two high speed correlation imaging systems were achieved. Real-time computational video system was first tried in the computational imaging system with a *Light Commander* DLP as for structured illumination. The fastest iteration speed of 600Hz was achieved when light pattern display, signal acquisition and computational calculation were arranged to run in parallel. However, as there was no inherent trigger signal from the system, synchronisation of the system was very unstable, and the system cannot run consistently in long time. To guarantee synchronisation measurement, a fast DMD with inherent trigger signals was employed to generate light patterns. The DMD can display binary patterns in 22kHz , each display accompanying with a trigger signal. These triggers can be used to run signal acquisition in synchronise to light pattern display. Moreover, a series of orthogonal patterns derived from Hadamard matrix were employed to achieve higher correlation efficiency. A 1024×1024 Hadamard matrix was used for correlation imaging in a resolution of 32×32 pixels. For each reconstructed image, 1024 Hadamard derived patterns in 32×32 were correlated with their signals. Under differential signal acquisition mode, an image needs 2048 display, which mean that it requires 0.1s to obtain an image in the fast DMD system, and the frame rate

is therefore in 10 Hz. A real time single-pixel camera in 10 Hz was also developed in a similar setup. The only difference was that a single-pixel camera utilised ambient light as the light source and therefore no extra light source was needed. Finally, an optimiser was applied to the image reconstructions to reduce noise.

Chapter 6

Conclusion and Future Work

Imaging systems discussed in this thesis can be called correlation imaging using single-pixel detectors. In general, correlation imaging with single-pixel detectors utilises spatial correlation of light to form an image. It employs a series of 2 dimensional patterns to encode the spatial information of an object into a series of corresponding intensities. An image is derived from the correlation between the light patterns and their object intensities. This technique is mainly derived from two different fields: computational ghost imaging (GI) and single-pixel camera. In both cases, a spatial light modulator (SLM) is employed to encode light. In computational GI, an SLM is used to generate structured illumination. In a single-pixel camera, however, a SLM, or more specifically a digital micro-mirror device (DMD), is utilised to encode the image of the object in its image plane. In both cases, light interacting with the object is only detected by single-pixel detectors, therefore only intensities are recorded with no spatial information. The spatial information of the object, however, is recovered by correlating the patterns with their corresponding light intensities.

The work discussed in this thesis originated from computational GI, which was a specific scheme of classical GI using correlation of pseudo-thermal light. GI was first conducted using quantum entanglement, but was later demonstrated using classical light. In a classical GI system using pseudo-thermal light, thermal speckles are generated as the light source for illumination. In a conventional classical GI system, a beamsplitter splits the speckles into two beams: the object beam where speckles illuminate the object and

are then collected by a single-pixel detector, and the reference beam where the speckle patterns are recorded by a CCD. Both these two beams are then sent to a correlation algorithms for image reconstruction. This classical GI system could be simplified by using a programmable spatial light modulator (SLM) to generate speckles. As speckles generated from an SLM can be predicted by the driven holograms, the CCD camera and beamsplitter can be removed from the system, resulting the system to be a real single-pixel imaging system. This system is called computational GI. The work in this thesis contributed by improving the computational GI into a more applicable technique.

Correlation algorithms play an important role in classical GI, because the reconstruction method itself contains intrinsic noise. In our first work, an advanced correlation algorithm was achieved for higher correlation efficiency. In a traditional GI (TGI) algorithm, the reconstruction signal-to-noise ratio (SNR) was affected by the fluctuation of the total intensity of the incident speckles. This fluctuation could be normalised by introducing a reference beam as an indication of the incident intensity. The normalised object intensity provides a more precious indication of the spatial correlation between the object and the illumination structure, and therefore performs a higher SNR compared to TGI, especially for a more transmissive object. This algorithm was called normalised GI (NGI), and was demonstrated by both simulation and experimental results. In the experiment, a computational GI setup was built up to test the algorithm. The system consists of an normal object beam and a reference beam where only a bucket detector was located. NGI was compared with other algorithms using the data from this system, and was proved to perform the same SNR in reconstruction as another algorithm called differential GI (DGI). Furthermore, in a single-beam computational GI system, the reference intensity can be obtained from simulation prediction. This method called single-detector NGI (SNGI) was able to improve the reconstruction using exactly the same data acquisition of TGI, but not able to perform as good as NGI. The normalisation method was also applied in compressive algorithms and was able to improve the reconstruction SNR for experimental results.

In our second experiment, the computational GI was adapted into a computational imaging system using single-pixel detectors. Compared to a computational GI system, the

most important change was that a digital light projector (DLP) was used for structured illumination. The DLP contained a digital micro-mirror device (DMD) and a white light source, which worked together to generate random binary patterns and projected onto the object space. Light reflected by an object within the depth of the projection was collected by a single-pixel detector and then correlated with the corresponding illumination structure. The same algorithm used in GI was used for image reconstruction. Due to the different way to generate structured illumination, the system was named as a “computational imaging system using single-pixel detectors” to be distinguished from a computational GI system. In this new system, correlation imaging was performed in a much higher SNR than classical GI using pseudo-thermal speckles. For the first time, to our knowledge, correlation imaging using structured illumination was able to image a 3D object with reasonable details. It was also realised that the shading information rather than the shape of an image changed when the detector was moved. Based on this principle, a 3D computational imaging system was built up. With a DLP used for unique structured illumination, there were four single-pixel detectors employed rather than one. Every detector was set in a different position and was used to produce an image. In one imaging process, all these four images obtained had the same shape but different shading. More specifically, as the object was a Lambertian surface with perfect diffuse reflection, the shading information was determined by the angles between the surface normals of the object and the detecting direction. Since the shading information in the four images as well as their detecting directions were known, the surface normals could be derived by solving an inverse problem, a technique which was called “photometric stereo”. The 3D reconstruction from this system was also compared with that from a commercial 3D camera and was confirmed with high precision.

In the last work, we increased the reconstruction speed of correlation imaging and developed a fast single-pixel imaging system. Normally, the reconstruction speed of correlation imaging was determined by the number of measurement and the measurement speed. To increase the imaging speed, both of these two aspects have been investigated. Previous single-pixel imaging used random structured illumination for sampling, which was in a low efficiency due to the overlap between any random structures. To get rid of

unnecessary overlap sampling, a series of orthogonal arrays were chosen for the 2D sampling. And the number of the arrays is always the same as that of the image resolution. Since the arrays are orthogonal to each other, sampling is conducted in a high efficiency. Compared to the results obtained from random patterns, a much higher SNR can be achieved within the same measurement. Additionally, the measurement speed, which was mainly limited by the speed of spatial mask generation, was improved by using a fast DMD which could project 2D patterns in 22 KHz. Furthermore, all the other part of the measurement like signal acquisition and computational calculation were done in parallel to the mask projection, resulting the system run the highest speed. For an image in 32×32 pixels, the system need 0.05s to finish 1024 steps of sampling. To achieve the differential signal method, 2048 steps were needed and therefore the required time to get an image is 0.1s. By repeating the same set of measurement, a real-time video in 10Hz was achieved. At last, an optimiser based on the principle of compressive algorithm was introduced to suppress the noise level in the single-pixel imaging.

Our work has an advanced correlation algorithm for GI. We also realised the first single-pixel computational imaging of a 3D reflective object, both in 2D and 3D. The reconstruction speed of single-pixel computational imaging system was also improved to a video frame rate. All these achievement brings single-pixel imaging to a more practical stage for some useful applications, while to utilise this imaging technique in some real application case still needs to be explored. In our future work, we are going to employ our single pixel computational imaging system in a specific application: single-pixel methane imaging. Detecting methane gas is important to safety monitoring in gas storage and transmission, therefore a low-cost imaging system therefore has wide industrial use. On the other hand, as methane normally contains very low spatial frequency, image reconstruction can be run in a relatively low resolution, the resultant reconstruction speed based on the real time single-pixel camera system is also very fast. Methane has strong absorption in $3\mu\text{m}$ and $1.6\mu\text{m}$. An imaging system based on the absorption spectrum can be done by using either the ambient background radiation or active laser illumination. Early research in our group has developed a methane imaging instrument based on active illumination and single-pixel scanning [134]. In our new

single-pixel computational imaging approach, we will use a $1.6\mu m$ laser diode for active illumination. In the detection end, instead of looking through one pixel at a time, our computational imaging system will sample many pixels. Signal to noise ratio will be analysed between scanning and multi-pixel sampling to quantitatively compare single pixel camera with scanning method.

Bibliography

- [1] T. B. Pittman, Y. H. Shih, D. V. Strekalov, and A. V. Sergienko. Optical imaging by means of two-photon quantum entanglement. *Phys. Rev. A*, pages R3429–R3432, Nov . doi: 10.1103/PhysRevA.52.R3429.
- [2] A. Gatti, E. Brambilla, M. Bache, and L. A. Lugiato. Ghost imaging with thermal light: Comparing entanglement and classical correlation. *Phys. Rev. Lett.*, page 093602, Aug . doi: 10.1103/PhysRevLett.93.093602.
- [3] A. Valencia, G. Scarcelli, M. D’Angelo, and Y. Shih. Two-photon imaging with thermal light. *Phys. Rev. Lett.*, page 063601, Feb . doi: 10.1103/PhysRevLett.94.063601.
- [4] F. Ferri, D. Magatti, A. Gatti, M. Bache, E. Brambilla, and L. A. Lugiato. High-resolution ghost image and ghost diffraction experiments with thermal light. *Phys. Rev. Lett.*, page 183602, May . doi: 10.1103/PhysRevLett.94.183602.
- [5] J. H. Shapiro. Computational ghost imaging. *Phys. Rev. A*, page 061802, Dec . doi: 10.1103/PhysRevA.78.061802.
- [6] D. N. Klyshko. A simple method of preparing pure states of an optical field, of implementing the einsteinpodolskyrosen experiment, and of demonstrating the complementarity principle. *Physics-Uspekhi*, 31(1):74–85, 1988.
- [7] R. S. Bennink, S. J. Bentley, and R. W. Boyd. “two-photon” coincidence imaging with a classical source. *Phys. Rev. Lett.*, page 113601, Aug . doi: 10.1103/PhysRevLett.89.113601.
- [8] M. O. Scully. *Quantum optics*. Cambridge university press, 1997.

-
- [9] R. Loudon. *The quantum theory of light*. Oxford university press, 2000.
- [10] C. Gerry and P. Knight. *Introductory quantum optics*. Cambridge university press, 2005.
- [11] R. H. Brown and R. Q. Twiss. Correlation between photons in two coherent beams of light, 1956.
- [12] R. H. Brown and R. Q. Twiss. A test of a new type of stellar interferometer on sirius. *Nature*, 178(4541):1046–1048, 1956.
- [13] L. Wang, S. Qamar, S. Zhu, and M. Zubairy. Hanbury brown-twiss effect and thermal light ghost imaging: A unified approach. *Phys. Rev. A*, 79:033835, Mar 2009. doi: 10.1103/PhysRevA.79.033835.
- [14] R. S. Aspden, D. S. Tasca, R. W. Boyd, and M.J. Padgett. Epr-based ghost imaging using a single-photon-sensitive camera. *New Journal of Physics*, (7):073032.
- [15] D. A. Kleinman. Theory of optical parametric noise. *Phys. Rev.*, 174:1027–1041, Oct 1968. doi: 10.1103/PhysRev.174.1027.
- [16] D. C. Burnham and D. L. Weinberg. Observation of simultaneity in parametric production of optical photon pairs. *Phys. Rev. Lett.*, 25:84–87, Jul 1970. doi: 10.1103/PhysRevLett.25.84.
- [17] D. N. Klyshko. *Photons Nonlinear Optics*. CRC Press, 1988.
- [18] Amnon Yariv. Quantum electronics, 3rd. *Edn.(John Wiley & Sons, New York, 1988)* p, 389, 1989.
- [19] E. Brambilla, A. Gatti, M. Bache, and L. A. Lugiato. Simultaneous near-field and far-field spatial quantum correlations in the high-gain regime of parametric down-conversion. *Phys. Rev. A*, 69:023802, Feb 2004. doi: 10.1103/PhysRevA.69.023802.
- [20] R. S. Aspden, D. S. Tasca, A. Forbes, R. W. Boyd, and M. J. Padgett. Experimental demonstration of klyshkos advanced-wave picture using a coincidence-count based, camera-enabled imaging system. *Journal of Modern Optics*, 61(7):547–551, 2014. doi: 10.1080/09500340.2014.899645.

-
- [21] A. V. Belinskii and D. N. Klyshko. Two-photon optics-diffraction, holography and transformation of two-dimensional signals. *ZHURNAL EKSPERIMENTALNOI I TEORETICHESKOI FIZIKI*, 105(3):487–493, 1994.
- [22] T. B. Pittman, D. V. Strekalov, D. N. Klyshko, M. H. Rubin, A. V. Sergienko, and Y. H. Shih. Two-photon geometric optics. *Phys. Rev. A*, 53:2804–2815, Apr 1996. doi: 10.1103/PhysRevA.53.2804.
- [23] A. F. Abouraddy, P. R. Stone, A. V. Sergienko, B. E. A. Saleh, and M. C. Teich. Entangled-photon imaging of a pure phase object. *Phys. Rev. Lett.*, 93:213903, Nov 2004. doi: 10.1103/PhysRevLett.93.213903.
- [24] B. Jack, J. Leach, J. Romero, S. Franke-Arnold, M. Ritsch-Marte, S. M. Barnett, and M. J. Padgett. Holographic ghost imaging and the violation of a bell inequality. *Phys. Rev. Lett.*, page 083602, Aug . doi: 10.1103/PhysRevLett.103.083602.
- [25] A. F. Abouraddy, B. E. A. Saleh, A. V. Sergienko, and M. C. Teich. Role of entanglement in two-photon imaging. *Phys. Rev. Lett.*, page 123602, Aug . doi: 10.1103/PhysRevLett.87.123602.
- [26] T. B. Pittman, D. V. Strekalov, A. Migdall, M. H. Rubin, A. V. Sergienko, and Y. H. Shih. Can two-photon interference be considered the interference of two photons? *Phys. Rev. Lett.*, 77:1917–1920, Sep 1996. doi: 10.1103/PhysRevLett.77.1917.
- [27] A. Gatti, E. Brambilla, and L. A. Lugiato. Entangled imaging and wave-particle duality: From the microscopic to the macroscopic realm. *Phys. Rev. Lett.*, page 133603, Apr . doi: 10.1103/PhysRevLett.90.133603.
- [28] A. Gatti, E. Brambilla, M. Bache, and L. A. Lugiato. Correlated imaging, quantum and classical. *Phys. Rev. A*, page 013802, Jul . doi: 10.1103/PhysRevA.70.013802.
- [29] R. S. Bennink, S. J. Bentley, R. W. Boyd, and J. C. Howell. Quantum and classical coincidence imaging. *Phys. Rev. Lett.*, page 033601, Jan . doi: 10.1103/PhysRevLett.92.033601.

-
- [30] G. Scarcelli, V. Berardi, and Y. Shih. Can two-photon correlation of chaotic light be considered as correlation of intensity fluctuations? *Phys. Rev. Lett.*, page 063602, Feb . doi: 10.1103/PhysRevLett.96.063602.
- [31] A. Gatti, M. Bondani, L. A. Lugiato, M. G. A. Paris, and C. Fabre. Comment on “can two-photon correlation of chaotic light be considered as correlation of intensity fluctuations?”. *Phys. Rev. Lett.*, page 039301, Jan . doi: 10.1103/PhysRevLett.98.039301.
- [32] B. Lorenzo and O. Pasquale. A conceptual experiment on single-beam coincidence detection with pseudothermal light. *Opt. Express*, 15(19):12386–12394, Sep 2007.
- [33] The physics of ghost imaging. *Quantum Information Processing*, 11(4), 2012. ISSN 1570-0755. doi: 10.1007/s11128-011-0356-5.
- [34] Response to the physics of ghost imagingnonlocal interference or local intensity fluctuation correlation?. *Quantum Information Processing*, 11(4), 2012. ISSN 1570-0755. doi: 10.1007/s11128-012-0399-2.
- [35] Joseph W. Goodman. *Speckle phenomena in optics: theory and applications*. Roberts and Company Publishers, 2007.
- [36] T. Shirai, T. Setälä, and A. T. Friberg. Ghost imaging of phase objects with classical incoherent light. *Phys. Rev. A*, 84:041801, Oct 2011. doi: 10.1103/PhysRevA.84.041801.
- [37] W. Gong and S. Han. Phase-retrieval ghost imaging of complex-valued objects. *Phys. Rev. A*, 82:023828, Aug 2010. doi: 10.1103/PhysRevA.82.023828.
- [38] D. Zhang, Q. Tang, T. Wu, H. Qiu, D. Xu, H. Li, H. Wang, J. Xiong, and K. Wang. Lensless ghost imaging of a phase object with pseudo-thermal light. *Applied Physics Letters*, 104(12):121113, 2014.
- [39] B. I. Erkmen and J. H. Shapiro. Unified theory of ghost imaging with gaussian-state light. *Phys. Rev. A*, 77:043809, Apr 2008. doi: 10.1103/PhysRevA.77.043809.
- [40] Leonard Mandel and Emil Wolf. *Optical coherence and quantum optics*. Cambridge university press, 1995.

- [41] Y. Bromberg, O. Katz, and Y. Silberberg. Ghost imaging with a single detector. *Phys. Rev. A*, 79:053840, May 2009. doi: 10.1103/PhysRevA.79.053840.
- [42] R. G. Baraniuk. Single-pixel imaging via compressive sampling. *IEEE Signal Processing Magazine*, 2008.
- [43] D. L. Donoho. Compressed sensing. *Information Theory, IEEE Transactions on*, 52(4):1289–1306, 2006.
- [44] E. J. Candes, J. K. Romberg, and T. Tao. Stable signal recovery from incomplete and inaccurate measurements. *Communications on pure and applied mathematics*, 59(8):1207–1223, 2006.
- [45] E. J. Candès and M. B. Wakin. An introduction to compressive sampling. *Signal Processing Magazine, IEEE*, 25(2):21–30, 2008.
- [46] David L. Donoho and Yaakov Tsaig. Fast solution of l1-norm minimization problems when the solution may be sparse, 2006.
- [47] Stephen P. Boyd and Lieven Vandenberghe. *Convex optimization*. Cambridge university press, 2004.
- [48] D. V. Strekalov, A. V. Sergienko, D. N. Klyshko, and Y. H. Shih. Observation of two-photon “ghost” interference and diffraction. *Phys. Rev. Lett.*, 74:3600–3603, May 1995. doi: 10.1103/PhysRevLett.74.3600.
- [49] M. D’Angelo, M. V. Chekhova, and Y. Shih. Two-photon diffraction and quantum lithography. *Phys. Rev. Lett.*, 87:013602, Jun 2001. doi: 10.1103/PhysRevLett.87.013602.
- [50] M. Zhang, Q. Wei, X. Shen, Y. Liu, H. Liu, J. Cheng, and S. Han. Lensless fourier-transform ghost imaging with classical incoherent light. *Phys. Rev. A*, 75:021803, Feb 2007. doi: 10.1103/PhysRevA.75.021803.
- [51] J. Cheng. Transfer functions in lensless ghost-imaging systems. *Phys. Rev. A*, 78:043823, Oct 2008. doi: 10.1103/PhysRevA.78.043823.
- [52] K. W. C. Chan, M. N. O’Sullivan, and R. W. Boyd. Two-color ghost imaging. *Phys. Rev. A*, 79:033808, Mar 2009. doi: 10.1103/PhysRevA.79.033808.

-
- [53] D. Duan, S. Du, and Y. Xia. Multiwavelength ghost imaging. *Phys. Rev. A*, 88: 053842, Nov 2013. doi: 10.1103/PhysRevA.88.053842.
- [54] S. S. Welsh, M. P. Edgar, R. B., P. J., B. Sun, and M. J. Padgett. Fast full-color computational imaging with single-pixel detectors. *Opt. Express*, 21(20): 23068–23074, Oct 2013.
- [55] M. Bache, E. Brambilla, A. Gatti, and L. A. Lugiato. Ghost imaging using homodyne detection. *Physical Review A*, 70(2):023823, 2004.
- [56] P. Zhang, W. Gong, X. Shen, S. Han, and R. Shu. Homodyne detection in ghost imaging with thermal light. *Phys. Rev. A*, 80:033827, Sep 2009. doi: 10.1103/PhysRevA.80.033827.
- [57] M. Bache, E. Brambilla, A. Gatti, and L. Lugiato. Ghost imaging schemes: fast and broadband. *Opt. Express*, 12(24):6067–6081, Nov 2004. doi: 10.1364/OPEX.12.006067.
- [58] D. S. Tasca, R. S. Aspden, P. A. Morris, G. Anderson, R. W. Boyd, and M. J. Padgett. The influence of non-imaging detector design on heralded ghost-imaging and ghost-diffraction examined using a triggered iccd camera. *Opt. Express*, 21(25):30460–30473, Dec 2013.
- [59] X. Chen, Q. Liu, K. Luo, and L. Wu. Lensless ghost imaging with true thermal light. *Opt. Lett.*, 34(5):695–697, Mar 2009.
- [60] N. Tian, Q. Guo, A. Wang, D. Xu, and L. Fu. Fluorescence ghost imaging with pseudothermal light. *Opt. Lett.*, 36(16):3302–3304, Aug 2011. doi: 10.1364/OL.36.003302.
- [61] M. H. Rubin and Y. Shih. Resolution of ghost imaging for nondegenerate spontaneous parametric down-conversion. *Phys. Rev. A*, 78:033836, Sep 2008. doi: 10.1103/PhysRevA.78.033836.
- [62] Pere Clemente, Vicente Durán, Víctor Torres-Company, Enrique Tajahuerce, and Jesús Lancis. Optical encryption based on computational ghost imaging. *Opt. Lett.*, 35(14):2391–2393, Jul 2010. doi: 10.1364/OL.35.002391.

- [63] J. Cheng. Ghost imaging through turbulent atmosphere. *Opt. Express*, 17(10): 7916–7921, May 2009.
- [64] J. Cheng and J. Lin. Unified theory of thermal ghost imaging and ghost diffraction through turbulent atmosphere. *Phys. Rev. A*, 87:043810, Apr 2013. doi: 10.1103/PhysRevA.87.043810.
- [65] M. Bina, D. Magatti, M. Molteni, A. Gatti, L. A. Lugiato, and F. Ferri. Backscattering differential ghost imaging in turbid media. *Phys. Rev. Lett.*, 110:083901, Feb 2013. doi: 10.1103/PhysRevLett.110.083901.
- [66] F. Ferri, D. Magatti, V. G. Sala, and A. Gatti. Longitudinal coherence in thermal ghost imaging. *Applied Physics Letters*, (26):261109, . doi: 10.1063/1.2945642.
- [67] F. Ferri, D. Magatti, L. A. Lugiato, and A. Gatti. Differential ghost imaging. *Phys. Rev. Lett.*, page 253603, Jun . doi: 10.1103/PhysRevLett.104.253603.
- [68] L. Ou and L. Kuang. Ghost imaging with third-order correlated thermal light. *Journal of Physics B: Atomic, Molecular and Optical Physics*, 40(10):1833.
- [69] K. W. C. Chan, M. N. O’Sullivan, and R. W. Boyd. High-order thermal ghost imaging. *Opt. Lett.*, 34(21):3343–3345, Nov 2009.
- [70] X. Chen, I. N. Agafonov, K. Luo, Q. Liu, R. Xian, M. V. Chekhova, and L. Wu. High-visibility, high-order lensless ghost imaging with thermal light. *Optics letters*, 35(8):1166–1168, 2010.
- [71] K. W. C. Chan, M. N. O’Sullivan, and R. W. Boyd. High-order thermal ghost imaging. *Optics letters*, 34(21):3343–3345, 2009.
- [72] Q. Liu, X. Chen, K. Luo, W. Wu, and L. Wu. Role of multiphoton bunching in high-order ghost imaging with thermal light sources. *Phys. Rev. A*, 79:053844, May 2009. doi: 10.1103/PhysRevA.79.053844.
- [73] I. N. Agafonov, M. V. Chekhova, S. Timur Iskhakov, and L. Wu. High-visibility intensity interference and ghost imaging with pseudo-thermal light. *Journal of Modern Optics*, 56(2-3):422–431, 2009.

-
- [74] K. W. C. Chan, M. N. O’Sullivan, and R. W. Boyd. Optimization of thermal ghost imaging: high-order correlations vs. background subtraction. *Optics express*, 18(6):5562–5573, 2010.
- [75] M. Li, Y. Zhang, K. Luo, L. Wu, and H. Fan. Time-correspondence differential ghost imaging. *Phys. Rev. A*, 87:033813, Mar 2013. doi: 10.1103/PhysRevA.87.033813.
- [76] M. Li, Y. Zhang, X. Liu, X. Yao, K. Luo, H. Fan, and L. Wu. A double-threshold technique for fast time-correspondence imaging. *Applied Physics Letters*, 103(21):211119, 2013. doi: <http://dx.doi.org/10.1063/1.4832328>.
- [77] B. Sun, S. S. Welsh, M. P. Edgar, J. H. Shapiro, and M. J. Padgett. Normalized ghost imaging. *Opt. Express*, 20(15):16892–16901, Jul 2012. doi: 10.1364/OE.20.016892.
- [78] B. I. Erkmen and J. H. Shapiro. Signal-to-noise ratio of gaussian-state ghost imaging. *Phys. Rev. A*, 79:023833, Feb 2009. doi: 10.1103/PhysRevA.79.023833.
- [79] M. N. O’Sullivan, K. W. C. Chan, and R. W. Boyd. Comparison of the signal-to-noise characteristics of quantum versus thermal ghost imaging. *Phys. Rev. A*, 82:053803, Nov 2010. doi: 10.1103/PhysRevA.82.053803.
- [80] G. Brida, M. V. Chekhova, G. A. Fornaro, M. Genovese, E. D. Lopaeva, and I. R. Berchera. Systematic analysis of signal-to-noise ratio in bipartite ghost imaging with classical and quantum light. *Phys. Rev. A*, 83:063807, Jun 2011. doi: 10.1103/PhysRevA.83.063807.
- [81] P. Zerom, Z. Shi, M. N. O’Sullivan, K. W. C. Chan, M. Krogstad, J. H. Shapiro, and R. W. Boyd. Thermal ghost imaging with averaged speckle patterns. *Phys. Rev. A*, 86:063817, Dec 2012. doi: 10.1103/PhysRevA.86.063817.
- [82] K. W. C. Chan. Role of photon statistics of light source in ghost imaging. *Opt. Lett.*, 37(13):2739–2741, Jul 2012.
- [83] Joseph Goodman. *Statistical optics*. Wiley, New York, 2000. ISBN 0471399167.

-
- [84] O. Katz, Y. Bromberg, and Y. Silberberg. Compressive ghost imaging. *Applied Physics Letters*, (13):131110. doi: 10.1063/1.3238296.
- [85] W. Yu, M. Li, X. Yao, X. Liu, L. Wu, and G. Zhai. Adaptive compressive ghost imaging based on wavelet trees and sparse representation. *Opt. Express*, 22(6): 7133–7144, Mar 2014. doi: 10.1364/OE.22.007133.
- [86] A. Shabani, R. L. Kosut, M. Mohseni, H. Rabitz, M. A. Broome, M. P. Almeida, A. Fedrizzi, and A. G. White. Efficient measurement of quantum dynamics via compressive sensing. *Phys. Rev. Lett.*, 106:100401, Mar 2011. doi: 10.1103/PhysRevLett.106.100401.
- [87] C. Zhao, W. Gong, M. Chen, E. Li, H. Wang, W. Xu, and S. Han. Ghost imaging lidar via sparsity constraints. *Applied Physics Letters*, 101(14):141123, 2012. doi: <http://dx.doi.org/10.1063/1.4757874>.
- [88] O. S. Magaña-Loaiza, G. A. Howland, M. Malik, J. C. Howell, and R. W. Boyd. Compressive object tracking using entangled photons. *Applied Physics Letters*, 102(23):231104, 2013. doi: <http://dx.doi.org/10.1063/1.4809836>.
- [89] B. Sun, M. P. Edgar, R. Bowman, L. E. Vittert, S. Welsh, A. Bowman, and M. J. Padgett. 3d computational imaging with single-pixel detectors. *Science*, 340(6134): 844–847, 2013. doi: 10.1126/science.1234454.
- [90] R. Meyers, K. S. Deacon, and Y. Shih. Ghost-imaging experiment by measuring reflected photons. *Phys. Rev. A*, 77:041801, Apr 2008. doi: 10.1103/PhysRevA.77.041801.
- [91] R. E. Meyers, K. S. Deacon, and Y. Shih. Quantum imaging of an obscured object by measurement of reflected photons. In *Optical Engineering+ Applications*, pages 70920E–70920E. International Society for Optics and Photonics, 2008.
- [92] C. Wang, D. Zhang, Y. Bai, and B. Chen. Ghost imaging for a reflected object with a rough surface. *Phys. Rev. A*, 82:063814, Dec 2010. doi: 10.1103/PhysRevA.82.063814.
- [93] N. D. Hardy and J. H. Shapiro. Reflective ghost imaging through turbulence. *Phys. Rev. A*, 84:063824, Dec 2011. doi: 10.1103/PhysRevA.84.063824.

- [94] N. D. Hardy and J. H. Shapiro. Computational ghost imaging versus imaging laser radar for three-dimensional imaging. *Phys. Rev. A*, 87:023820, Feb 2013. doi: 10.1103/PhysRevA.87.023820.
- [95] Larry J. Hornbeck. From cathode rays to digital micromirrors: A history of electronic projection display technology. *Texas Instruments Technical Journal*, 15(3): 7–46, 1998.
- [96] L. A. Yoder, W. M. Duncan, E. M. Koontz, J. So, T. A. Bartlett, B. L. Lee, B. D. Sawyers, D. Powell, and P. Rancuret. Dlp technology: applications in optical networking. In *International Symposium on Optical Science and Technology*, pages 54–61. International Society for Optics and Photonics, 2001.
- [97] Y. Lu and S. Chen. Direct write of microlens array using digital projection photopolymerization. *Applied Physics Letters*, 92(4):041109, 2008. doi: <http://dx.doi.org/10.1063/1.2838751>.
- [98] Y. Ren, M. Li, K. Huang, J. Wu, H. Gao, Z. Wang, and Y. Li. Experimental generation of laguerre-gaussian beam using digital micromirror device. *Appl. Opt.*, 49(10):1838–1844, Apr 2010. doi: 10.1364/AO.49.001838.
- [99] T. Ota, S. Kawata, T. Sugiura, M. J. Booth, M. A. A. Neil, R. Juškaitis, and T. Wilson. Dynamic axial-position control of a laser-trapped particle by wave-front modification. *Opt. Lett.*, 28(6):465–467, Mar 2003. doi: 10.1364/OL.28.000465.
- [100] M. Mirhosseini, O. S. Magaña Loaiza, C. Chen, B. Rodenburg, M. Malik, and R. W. Boyd. Rapid generation of light beams carrying orbital angular momentum. *Opt. Express*, 21(25):30196–30203, Dec 2013. doi: 10.1364/OE.21.030196.
- [101] Berthold K. P. Horn. Understanding image intensities. *Artificial Intelligence*, (2): 201 – 231. ISSN 0004-3702. doi: 10.1016/0004-3702(77)90020-0.
- [102] V. S. Ramachandran. Perception of shape from shading. *Nature*, 331:163, Jan 1988. doi: 10.1038/331163a0.
- [103] R. Zhang, P. Tsai, J. E. Cryer, and M. Shah. Shape-from-shading: a survey. *Pattern Analysis and Machine Intelligence, IEEE Transactions on*, 21(8):690 – 706, aug 1999. ISSN 0162-8828. doi: 10.1109/34.784284.

- [104] E. Rouy and A. Tourin. A viscosity solutions approach to shape-from-shading. *SIAM Journal on Numerical Analysis*, 29(3):867–884, 1992.
- [105] R. T. Frankot and R. Chellappa. A method for enforcing integrability in shape from shading algorithms. *Pattern Analysis and Machine Intelligence, IEEE Transactions on*, 10(4):439–451, 1988.
- [106] Q. Zheng and R. Chellappa. Estimation of illuminant direction, albedo, and shape from shading. In *Computer Vision and Pattern Recognition, 1991. Proceedings CVPR'91., IEEE Computer Society Conference on*, pages 540–545. IEEE, 1991.
- [107] K. Ikeuchi and B. KP Horn. Numerical shape from shading and occluding boundaries. *Artificial intelligence*, 17(1):141–184, 1981.
- [108] B. KP Horn and M. J. Brooks. The variational approach to shape from shading. *Computer Vision, Graphics, and Image Processing*, 33(2):174–208, 1986.
- [109] B. KP Horn. Shape from shading: A method for obtaining the shape of a smooth opaque object from one view. 1970.
- [110] J. J. Atick, P. A. Griffin, and A. N. Redlich. Statistical approach to shape from shading: Reconstruction of three-dimensional face surfaces from single two-dimensional images. *Neural Computation*, 8(6):1321–1340, 1996.
- [111] Robert J. Woodham. Photometric method for determining surface orientation from multiple images. *Optical Engineering*, (1):191139–191139–. doi: 10.1117/12.7972479.
- [112] D.B. Goldman, B. Curless, A. Hertzmann, and S. M. Seitz. Shape and spatially-varying brdfs from photometric stereo. *Pattern Analysis and Machine Intelligence, IEEE Transactions on*, 32(6):1060–1071, June 2010. ISSN 0162-8828. doi: 10.1109/TPAMI.2009.102.
- [113] S. Barsky and M. Petrou. The 4-source photometric stereo technique for three-dimensional surfaces in the presence of highlights and shadows. *Pattern Analysis and Machine Intelligence, IEEE Transactions on*, 25(10):1239–1252, Oct 2003. ISSN 0162-8828. doi: 10.1109/TPAMI.2003.1233898.

- [114] Katsushi Ikeuchi. Determining surface orientations of specular surfaces by using the photometric stereo method. *Pattern Analysis and Machine Intelligence, IEEE Transactions on*, PAMI-3(6):661–669, Nov 1981. ISSN 0162-8828. doi: 10.1109/TPAMI.1981.4767167.
- [115] Robert J. Woodham. Gradient and curvature from the photometric-stereo method, including local confidence estimation. *J. Opt. Soc. Am. A*, 11(11):3050–3068, Nov 1994. doi: 10.1364/JOSAA.11.003050.
- [116] J. A. Webb and J. K. Aggarwal. Shape and correspondence. *Computer Vision, Graphics, and Image Processing*, (1):145 – 160. ISSN 0734-189X. doi: 10.1016/S0734-189X(83)80032-2.
- [117] D. Scharstein and R. Szeliski. A taxonomy and evaluation of dense two-frame stereo correspondence algorithms. *International Journal of Computer Vision*, 47(1-3):7–42, 2002.
- [118] H. Jin, S. Soatto, and A. J. Yezzi. Multi-view stereo reconstruction of dense shape and complex appearance. *International Journal of Computer Vision*, 63(3):175–189, 2005.
- [119] J. Geng. Structured-light 3d surface imaging: a tutorial. *Adv. Opt. Photon.*, 3(2):128–160, Jun 2011. doi: 10.1364/AOP.3.000128.
- [120] B. Khambay, N. Nairn, A. Bell, J. Miller, A. Bowman, and A. F. Ayoub. Validation and reproducibility of a high-resolution three-dimensional facial imaging system. *British Journal of Oral & Maxillofacial Surgery*, 46(1):27–32, January 2008. doi: DOI10.1016/j.bjoms.2007.04.017.
- [121] L. G. Farkas. *Anthropometry of the head and face*. Raven Press, New York, second edition, 1994.
- [122] J. Zheng and E. L. Jacobs. Video compressive sensing using spatial domain sparsity. *Optical Engineering*, 48(8):087006–087006, 2009.
- [123] P. Llull, X. Liao, X. Yuan, J. Yang, D. Kittle, L. Carin, G. S, and D. J. Brady. Coded aperture compressive temporal imaging. *Optics express*, 21(9):10526–10545, 2013.

- [124] X. Yuan, J. Yang, P. Llull, X. Liao, G. Sapiro, D. J. Brady, and L. Carin. Adaptive temporal compressive sensing for video. *arXiv preprint arXiv:1302.3446*, 2013.
- [125] M. A. Herman, J. Tidman, D. Hewitt, T. Weston, and L. McMackin. A higher-speed compressive sensing camera through multi-diode design. In *SPIE Defense, Security, and Sensing*, pages 871706–871706. International Society for Optics and Photonics, 2013.
- [126] K. Kumar. Microelectromechanical handheld laser-scanning confocal microscope: application to breast cancer imaging. 2010.
- [127] R. A. DeVerse, R. R. Coifman, A. C. Coppi, W. G. Fateley, F. Geshwind, R. M. Hammaker, S. Valenti, F. J. Warner, and G. L. Davis. Application of spatial light modulators for new modalities in spectrometry and imaging. In *Biomedical Optics 2003*, pages 12–22. International Society for Optics and Photonics, 2003.
- [128] J. Hadamard. Résolution dune question relative aux déterminants. *Bull. sci. math*, 17(1):240–246, 1893.
- [129] Kathy J. Horadam. *Hadamard matrices and their applications*. Princeton university press, 2007.
- [130] A. Hedayat and WD. Wallis. Hadamard matrices and their applications. *The Annals of Statistics*, 6(6):1184–1238, 1978.
- [131] J. Williamson. Hadamards determinant theorem and the sum of four squares. *Duke Mathematical Journal*, 11(1):65–81, 03 1944. doi: 10.1215/S0012-7094-44-01108-7.
- [132] T. T. Do, T. D. Tran, and Lu G. Fast compressive sampling with structurally random matrices. In *Acoustics, Speech and Signal Processing, 2008. ICASSP 2008. IEEE International Conference on*, pages 3369–3372. IEEE, 2008.
- [133] J. A. Tropp. Improved analysis of the subsampled randomized hadamard transform. *Advances in Adaptive Data Analysis*, 3(01n02):115–126, 2011.
- [134] Graham Gibson, Ben van Well, Jane Hodgkinson, Russ Pride, Rainer Strzoda, Stuart Murray, Steve Bishton, and Miles Padgett. Imaging of methane gas using a scanning, open-path laser system. *New Journal of Physics*, 8(2):26, 2006.